Doctoral theses at NTNU, 2006:239

Frank Mauseth

Charge accumulation in rod-plane air gap with covered rod

NTNU
Norwegian University of
Science and Technology
PhD Thesis
Faculty of Information Technology, Mathematics
and Electrical Engineering
Department of Electric Power Engineering

Frank Mauseth

Doctoral thesis 2006:239

NTNU

Frank Mauseth

Charge accumulation in rod-plane air gap with covered rod

PhD Thesis

Trondheim, December 2006

Norwegian University of Science and Technology
Faculty of Information Technology,
Mathematics and Electric Engineering
Department of Electric Power Engineering

NTNU
Innovation and Creativity

NTNU
Norwegian University of Science and Technology

PhD Thesis

Faculty of Information Technology, Mathematics and Electrical Engineering
Department of Electric Power Engineering

ISBN 82-471-8261-0 (printed version)
ISBN 82-471-8260-2 (electronic version)
ISSN 1503-8181

Doctoral theses at NTNU, 2006:239

Printed by NTNU-trykk

PREFACE

This thesis is submitted in partial fulfilment of the requirements for the degree of Philosophiae Doctor (PhD) at the Norwegian University of Science and Technology (NTNU).

The work was carried out at the Department of Electric Power Engineering at the Faculty of Information Technology, Mathematics and Electrical Engineering.

The research has been founded by the Norwegian Research Council.

ACKNOWLEDGEMENTS

My main supervisor has been Professor Arne Nysveen and co-supervisor Professor Erling Ildstad both of the Department of Electric Power Engineering, NTNU. I would like to thank my supervisors for their contributions, suggestions and support during the work on my thesis. I would also like to thank Professor Franz-Theo Suttmeier and his PhD-students Monica Dücker and Ivan Cherlenyak at University of Siegen and Dr Trond Varslot, currently at the Rensselaer Polytechnic Institute, USA, for their valuable help on the mathematical part of this work. I also acknowledge the English editing support from Stewart Clark at NTNU. I am indebted to Ole Granhaug and Pål Skryten at ABB Skien for their support.

Finally, I would like to express my thanks to my family, friends and my colleagues at the Department of Electric Power Engineering at NTNU for their support and encouragement during the work on this thesis.

Trondheim, December 2006

Frank Mauseth

ABSTRACT

The focus of this work has been on hybrid insulation in inhomogeneous electric fields under lightning impulse voltage stress. The principal idea behind hybrid insulation is the intentional use of surface charges to re-distribute the electric field within an insulation system. This allows a significant part of the electric stress to be transferred from the dielectric weaker gas to the dielectric stronger solid insulation thus increasing the total electric strength of the insulation system.

The concept has been theoretically and experimentally addressed by means of a hemispheric rod covered with a layer of solid insulation. Discharge activity and surface charge accumulation have been studied in an air gap by measuring the voltage and discharge current and recording the discharge activity using a high-speed digital camera. New methods have been introduced and evaluated for the evaluation of surface charge measurements.

The experiments found that the increase in positive inception voltage was considerable compared to uncovered rods. This increase varied from 35% up to 100% depending on the electrode distance. The increase in breakdown strength is higher than the increase in inception voltage and dependent on the covered length of the rod. During the application of a lightning impulse, the discharge activity spreads upwards along the rod and out into the air gap. Positive discharges form numerous branches and bridge the air gap in most cases. Negative discharges are more diffuse, less light intensive and only form a few branches around the tip of the rod where the electric field is the strongest.

Discharge activity along the insulating surface has been observed where the background field is lower than the critical electric field strength. Visible discharge activity is observed where the background field is higher than 2.3 kV/mm and 2.5 kV/mm for positive and negative impulses respectively.

During the application of lightning impulses, discharge activity starts in the air gap around the tip where the electric field is highest and spreads upwards along the rod. As expected, negative charges accumulate on the surface in the case of positive impulse voltage and vice versa. However, after more powerful discharges during negative impulse voltage application, surface charges of both polarities have been observed.

Accumulated surface charges decay exponentially with a time constant τ varying from micro-seconds to hours depending on the material properties of the solid insulation. The dominating relaxation mechanism is found to be conduction through the solid insulation.

Improved methods to calculate surface charges based on probe response for a 2D axial symmetric case have been developed and evaluated. The method that is best suited for this purpose is the λ-method with truncated singular value decomposition (TSVD) as regularization.

Surface charge calculations show that the accumulated surface charges for the used configuration typically have a maximum value of 0.6 to 1.5 μC/m² and 0.4 to 1 μC/m² after positive and negative impulses respectively. The surface charge density in the areas with the highest discharge activity is relatively uniform. Further upwards along the rod, the surface charge density is reduced relatively fast towards zero, and in some cases, it changes polarity before approaching zero.

TABLE OF CONTENTS

LIST OF SYMBOLS AND ABBREVIATIONS

Symbol	*Unit*	*Description*
B	T	magnetic flux density
C	F	capacitance
D	C/m²	electric displacement flux density
E	V/m	electric field strength
F	N	force
H	A/m	magnetic field strength
J	A/m²	current density
j		$\sqrt{-1}$, imaginary unit
$\vec{n}$		unit vector
q	C	charge
T	K	absolute temperature
t	s	time
U	V	potential
z_0	m	critical avalanche length
α^*	mm^{-1}	effective ionization coefficient
α	mm^{-1}	ionization coefficient
η	mm^{-1}	electron attachment coefficient
μ	cm^2/Vs	mobility
ε_0	F/m	permittivity of free space ($8.854 \cdot 10^{-12}$ F/m)
ε_r		relative permittivity
σ	C/m²	surface charge density
σ		singular value
σ_a	S/m	apparent conductivity
τ	s	time constant
ω	rad/s	angular frequency
ω	mm^{-1}	second ionization coefficient
$\nabla \cdot A$		divergence of A
$\nabla \times A$		curl of A
$\|A\|_2$		Euclidean norm of A ($\mathbf{A} = [a_1, a_2, .. a_n] \rightarrow \|A\|_2 = \sqrt{\sum_{k=1}^{n} \|a_k\|^2}$)

Abbreviation	*Description*
ac	alternating current
dc	direct current
FEM	finite element method
LI	lightning impulse
RTV	room temperature vulcanized
SIR	silicone rubber
SNR	signal-to-noise ratio
SVD	singular value decomposition
TSVD	truncated singular value decomposition

1 INTRODUCTION

1.1 Background

Gas insulated high voltage systems today mainly apply atmospheric air or pressurized sulphur hexafluoride (SF_6) as a dielectric medium.
Non-pressurized air-insulated switchgear and insulation systems are widely used due to their low price and high reliability. The main disadvantage of this kind of insulation system is the moderate withstand voltage of air, making such systems physically large, which in some applications makes the total cost high.
Several techniques are used to reduce their physical size. An increase in gas pressure results in a nearly proportional increase in the withstand voltage. However, this requires placing the insulation system inside pressurized tanks, which increases the cost and risk for personnel and equipment in the case of a fault in the insulation system.
The electronegative gas SF_6 has good electric and thermal properties, is chemically inert and non-toxic. At moderate pressure, SF_6 offers a withstand voltage that is 5 to 10 times higher than that of atmospheric air. However, SF_6 and some of its decomposition products contribute to the greenhouse effect and are therefore included in the Kyoto Protocol of the United Nations about gases which should be reduced. Alternatives to SF_6 are therefore currently being sought.

Normally, the high voltage insulation used is of gaseous, solid or liquid consistence. A combination of dielectrics of different properties within the same insulating system should be done with great care as this might result in undesirable field distributions. This is especially the case when combining a solid and gaseous dielectric as the gas tends to have lower breakdown strength and permittivity, the latter causing a higher electric field in the gas than in the solid insulation. Normally this can cause undesirable discharge activities that finally can lead to a breakdown of the insulation system. However, these discharges and associated charges can also be utilized in a favourable way for an insulation system, as is the case in a so-called hybrid insulation system.

For gas-insulated systems the impulse withstand voltage is normally the dimensioning criteria, the ac withstand voltage is then normally automatically satisfied. This is due to the rapid flashover mechanisms of air, making the momentary voltage stress vital for the breakdown voltage of the insulating system.

1.2 Research objectives

Previous experiments have shown that covering one, or both electrodes with a layer of solid insulation in a gas insulated system, can increase the breakdown voltage for lightning impulses considerably. The main goal of this work has been to increase the

knowledge of hybrid insulation in inhomogeneous electric fields by studying discharge phenomena, surface charge distribution and the stress of the solid insulation.

The surface charge densities associated with these kinds of insulation systems are high, necessitating a large distance between the surface and the probe to avoid flashover during measurements of surface charges. Existing methods for the evaluation of such measurements are very sensitive to perturbations, making them unsuited for practical measurements.

Three new methods for the estimation of surface charge densities based on E-field measurements from a large distance are introduced, tested and compared in this thesis: Two of these methods use either the boundary element method (BEM) or the finite element method (FEM) together with regularization, and the third method uses truncated singular value decomposition (TSVD) as regularization of Pedersen's λ-method [1].

1.3 Outline of thesis

Initially, the basic theory of gas discharges, avalanche theory and calculation, dielectric surface insulation and a review of hybrid insulation systems together with a review of surface charge measurements are given in Chapter 2.
The experimental set-up is presented in Chapter 3 together with the measurement procedures. The experimental results are presented in Chapter 4.
In Chapter 5, new methods for surface charge estimation based on E-field measurements at a large distance are presented. The different methods are tested and evaluated with respect to surface charge densities. A discussion of the work presented is given in Chapter 6 and the conclusions are formulated in Chapter 7.

2 LITERATURE REVIEW

The electric breakdown strength of a gas-insulated gap between two metal electrodes can be improved considerably when one or both of the electrodes are covered with a dielectric coating, so-called hybrid insulation.
The effect of the coating depends on the electrode shape, voltage polarity, pre-charging and the duration and form of the applied voltage.

2.1 Hybrid insulation - basic theory

2.1.1 Introduction

A hybrid insulation system comprises at least two types of dielectric media. One example is the combination of solid and gaseous dielectrics where one or more of the electrodes are covered with a layer of solid insulation. Through intentional use of accumulated surface charges, the lightning impulse withstand voltage can be increased considerably for the insulating system compared to a pure gas-insulated system. The accumulation of surface charges influences the electrical field distribution, as given by Gauss' law:

$$\nabla \cdot \vec{D} = \rho \tag{2.1}$$

The concept can be illustrated by the one-dimensional model shown in Fig. 2.1, where both electrodes in a gas gap are covered with a layer for solid insulation with permittivity ε_s and conductivity σ_s.

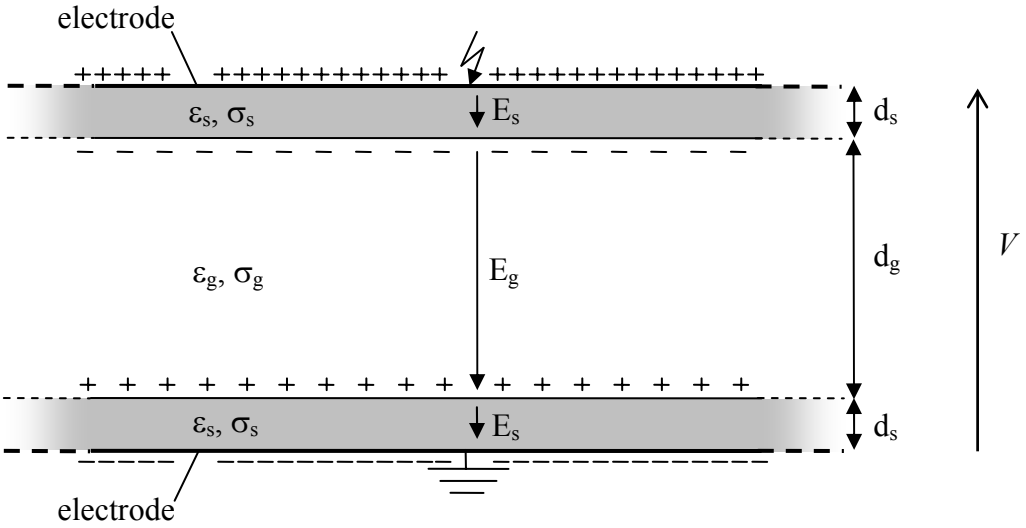

Fig. 2.1 – Basic concept hybrid insulation.

When free charges are present in the air gap, they are exposed to the Lorentz force:

$$\vec{F} = q\vec{E} \tag{2.2}$$

where q is the charge of the particle and E the electric field strength. The charged particle moves towards the electrode of opposite polarity of the particle itself. Since the electrodes are covered with a layer of solid insulation, charges accumulate on them. This charge accumulation continues as long as the electric field component normal to the surface is larger than zero. At any moment in time, the electric field distribution of an insulation system is generally governed by a capacitive and a charge induced field component:

$$\vec{E}_{\text{total}} = \vec{E}_{\text{capasitive}} + \vec{E}_{\text{charge induced}} \tag{2.3}$$

The contribution from space charge formation in the gap and at the insulation covered surfaces actively redistributes the electric field within the insulation system, resulting in an increased electric field in the solid insulation and a decreased electric field in the air gap, hereby quenching the discharge activities in the air gap and increasing the breakdown voltage of the insulation system compared to that of a pure gas-insulated system [2, 3].

2.1.2 Capacitive charge distribution

During application of a time varying voltage, a capacitive current $i_c = C\ dU/dt$ runs, and the electric field distribution is determined by the electrode geometry and the permittivity of the applied insulating materials. In a system without surface charge, the effect of a polymeric layer covering the rod is a reduction both in the maximum electric field close to the metal electrode and in the air. However, for hybrid insulation systems, results show that the increase in breakdown strength is much higher than what can be expected from just this capacitive/permittivity effect [2, 3].

2.1.3 Discharge activities and surface charge formation

The discharges, which occur in the air above the critical electric field strength, are characterized by a large number of micro-discharges or so-called independent current filaments. These streamer-like micro-discharges spread out across the air gap. Typically, micro-discharges have a diameter of 10 – 100 μm, area densities of 10-100 cm^{-2} and are associated with current pulses with duration of a few to 100 ns, peak currents of 100 mA and a total charge of 0.1-1 nC [4-7]. The electrons created rapidly attach to oxygen, resulting in the formation of negative oxygen and positive nitrogen ions [7]. Due to the applied electric stress, these charges rapidly drift towards the electrodes following the discharge paths. In case of a covered electrode, the charges accumulate on the surface, causing local field reduction and the quenching of the discharge activities. Without the insulation layer, the electric breakdown of the insulation system is likely to occur.
Results from examination of covered electrodes in a uniform electric field show that micro-discharges are distributed homogeneously over the covered electrodes [2, 8, 9].

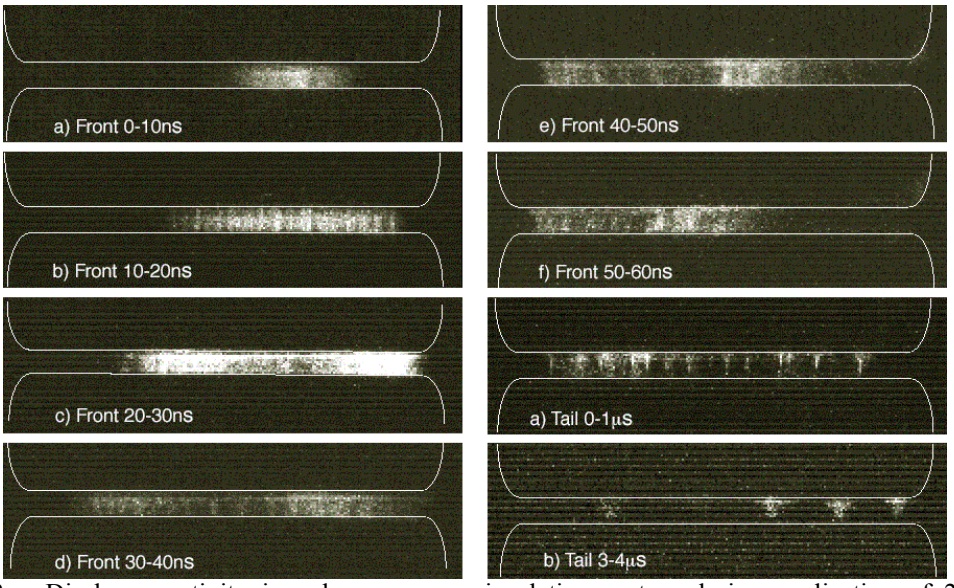

Fig. 2.2 – Discharge activity in a homogeneous insulation system during application of 2.4/51μs lightning impulse voltage during the front and tail [3].

The heterogeneous charge building up on the insulator surface reduces the field strength in the air gap causing a corresponding increase in the field inside the solid material.

In case of an inhomogeneous electrode configuration, it is likely that most of the same phenomena will take place, causing a net reduction of the field in the air gap. Thus the charges accumulated due to the first burst of micro-discharges are expected to cause discharges along the barrier surface as well as new micro-discharges in the air gap. In a non-uniform field, it is unlikely that the resulting surface charge will be homogeneously distributed over the surface of the insulated rod.

The amount of charge required to quench the discharges is dependent on the applied electric field, the electrode arrangement and the material properties. Generally, less charge is needed in case of a thick coating with a low relative permittivity, as the capacitance between the surface and the rod is low.

During discharges in a covered electrode system, the net sum of the charges in the gap is zero, resulting in no resistive current. The rapid varying electric field distribution in the insulation system during discharge activity will, however, result in a high displacement current.

2.1.4 Charge relaxation

Relaxation time constant

When applying a dc voltage over an insulating material, the field distribution is initially, and for a short time afterwards, capacitive. After that, a transition from a capacitive to resistive field distribution takes place. The transition is recognized by a relaxation time constant τ that ranges from seconds to days depending on the properties of the insulation material:

In a region with uniform permittivity and conductivity, the charge conservation and Gauss' law determine the charge density throughout the volume of the material [10]:

$$\nabla \cdot \vec{J} + \frac{\partial \rho}{\partial t} = 0 \tag{2.4}$$

Inserting Ohm's law

$$\vec{J} = \sigma \vec{E} \tag{2.5}$$

and Gauss' law, (2.1), into (2.4) gives the charge relaxation equation for ρ:

$$\frac{\partial \rho}{\partial t} + \frac{\sigma}{\varepsilon} \rho = 0 \tag{2.6}$$

The solution of (2.6) is an exponential function with time constant τ given by

$$\tau = \frac{\varepsilon}{\sigma} = \frac{\varepsilon_0 \varepsilon_r}{\sigma} \tag{2.7}$$

where σ is the conductivity and ε_r is the relative permittivity of the insulation material.

Relaxation discharges

The polarity of the accumulated charge at the barrier surface is opposite to that of the adjacent electrode. When the applied voltage is reduced to zero, the air gap is stressed with an electric field directed in the opposite direction. The magnitude of this stress may

be high enough to cause new discharges. This is particularly likely to occur if a voltage of opposite polarity is applied [2].

Otherwise the trapped charge may slowly decay to earth via the resistance of the air gap and the insulating barrier. As the capacitance of the barrier is much higher than that of the air gap, the time constant of this decay is mainly given by the properties of the solid insulation layer as shown in Eq. (2.7).

2.2 Gas discharge

This chapter describes the physical mechanisms regarding the concept of hybrid insulation, including the basic theory on discharges and breakdown of gaseous dielectrics.

2.2.1 Ionization coefficient

A gaseous dielectric always contains some free electrons as the gas molecules are ionized by light, cosmic and radioactive radiation. With no electric field present, free electrons recombine with the positive ions. With an electric field present, the electrons are accelerated in the direction of the applied electric field E by the force F = eE. The average kinetic energy E_k gained between each collision is then given by [11]:

$$E_k = eE\lambda \tag{2.8}$$

where λ is the average length of free path of the electron and is inversely proportional to the gas pressure p. When an electron collides with an atom/molecule, one out of the following scenarios might happen [12, 13]:

- The collision is elastic and the electron loses a fraction of its energy as it is being scattered. The electron accelerates further until the next collision.
- The collision is inelastic, causing an excitation of the atom. The atom is temporary excited and radiates a photon when it falls back to its basic state.
- Recombination; the electron is attached to an atom or an ion and does not contribute to further ionization.

The energy needed for ionization of oxygen at atmospheric pressure is 12.2 eV while the ionization energy for nitrogen is 15.5 eV.
The inelastic collision is the most important for the initiation of a (partial) breakdown of the gas. The ionization coefficient α gives the relationship between the number of new ions created per length unit in the field direction. A fraction of the electrons recombine or get attached to molecules forming heavy negative ions which consequently do not contribute to further ionization. The electron attachment coefficient η gives the relation of lost/recombined electrons per length unit in the field direction. The effective ionization coefficient is found from this to be:

$$\alpha^* = \alpha - \eta \tag{2.9}$$

Typical values of α^* in air at standard atmospheric conditions as a function of the electric field is given in Fig. 2.3. The total number of free electrons generated along an avalanche path is given by

$$dN(z) = \alpha^*(z)\, N(z)\, dz \tag{2.10}$$

where N(z) is a continuous differentiable function representing the number of electrons N_e participating in the collision process. The equation is valid when swarm conditions exist.

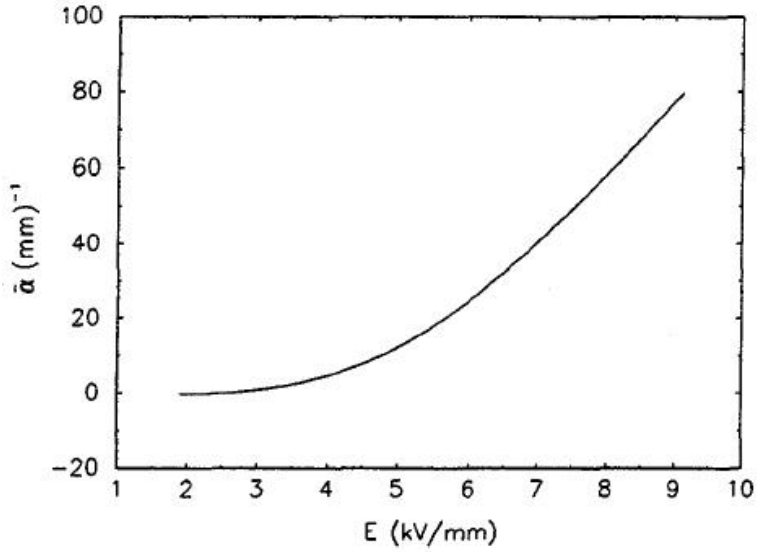

Fig. 2.3 – Effective ionization coefficient α^* as function of electric field magnitude in air at standard atmospheric conditions [14].

2.2.2 Streamer criterion

The streamer breakdown criterion is commonly used as a tool to calculate the inception of breakdown voltage of gas gaps under various gas pressures and electric field distributions.

Application of Eq. (2.10) is normally restricted to the later stage of the electron avalanche development. Initially N_e is too small for swarm conditions to exist. This implies that the avalanche growth is not exponential in the beginning.
Active mechanisms are field distortion and photo-ionization. A proper mathematical model of the physical mechanisms for the streamer has not been formulated [11]. However, it is possible to utilize the inherent mathematical nature of exponential growth to formulate a quantitative numerical criterion from which the onset of breakdown voltage can be calculated assuming known electric field distribution.

An electric breakdown is assumed to occur if N_e, the number of electrons in the avalanche, reaches a critical number N_c. The actual value of N_c is unknown, but is found to be around 10^6-10^8, dependent on the test conditions [11]. The growth of an avalanche

becomes exponential when swarm conditions exist, after a distance z_1 where the number of electrons is $N(z_1)$. After this distance, the number of electrons in the avalanche head is exponentially increasing according to

$$N(z) = N(z_1) \exp\left[\int_{z_1}^{z} \alpha^*(z')\, dz'\right] \tag{2.11}$$

The critical length z_0 of an avalanche as it reaches the critical number of electrons N_e is called critical avalanche length z_0. In a homogeneous or weakly inhomogeneous field, z_0 is equal to the electrode distance d. In an inhomogeneous field z_0 is the distance along the field line until the point where the avalanche growth stops, i.e. where α^* is zero.
As long as $z < z_1$, swarm conditions do not exist and the growth of avalanches will be stochastic. $N(z)_{max}$ will then be given by the smallest value of z_1 along a field line, i.e. the avalanche producing the highest number of electrons:

$$N_c = N(z_0)_{max} \tag{2.12}$$

where

$$N(z_0) = N(z_1) \exp\left[\int_{z_1}^{z_0} \alpha^*(z)\, dz\right] \tag{2.13}$$

Eq. (2.12) can then be re-written to

$$N_c = \left[\frac{N(z_1) \exp\left[\int_{0}^{z_0} \alpha^*(z) dz\right]}{\exp\left[\int_{0}^{z_1} \alpha^*(z)\, dz\right]}\right]_{max} \tag{2.14}$$

There are variations in the size of electron avalanches, i.e. $N(z_1)$ can differ considerably from the value in the denominator. At the on-set of a breakdown, the value of the ratio of the exponential forms has a maximum for a minimal value of z_1.
From Eq. (2.14) it can be found that at the on-set of breakdown it yields [11]:

$$\ln\left(N_c\right) \neq \int_{0}^{z_0} \alpha^*(z)\, dz \tag{2.15}$$

Thus at the on-set of a breakdown, the largest electron avalanche is not given by this integral. However, due to the exponential nature of the variation of α^* with the electric field, the integral is dominant in Eq. (2.14) so that it effectively controls the on-set of a breakdown. In other words, the on-set of breakdown occurs when the integral in Eq. (2.15) reaches a certain value K. The streamer criterion can then, strictly empirical, be written as:

$$\int_0^{z_0} \alpha^*(z)\, zd = K \qquad (2.16)$$

The value of K in the literature differs between 9 and 18. In this work K = 9 is assumed, giving the lowest breakdown strength, in accordance with Ref. [11, 12]

2.2.3 Drift and diffusion of electrons and ions

When a swarm of electrons or ions in a gas is subjected to an electric field the swarm moves as a whole with its centre of mass parallel to the field with a velocity v - the drift velocity of charged particles. For sufficient low values of the electric field strength, the drift velocity is proportional to the electric field strength for a given gas pressure. The mobility μ can then be defined as μ = v/E. The mobility for ions is referred to atmospheric pressure and temperature [15, 16]:

$$\mu_0 = v\left(\frac{E}{p}\right)^{-1} \cdot \frac{273}{T} \quad \left[\mathrm{cm^2/Vs}\right] \qquad (2.17)$$

The value used in literature is the "zero-field, reduced mobility" which is the limiting value of μ_0 as the electric field E approaches zero. Table 2.1 gives the values of μ_0 for the major ions and electrons in air.

Table 2.1– Mobility in air at 20ºC and 1 atm.

Ion	**Mobility μ_0[cm^2/Vs]**
N^+	3.4
N_2^+	2.8
O^+	2.74
O_2^+	2.29
O_2^-	2.59
electron	214

The mobility of electrons in air at atmospheric pressure and 293K is 214 cm^2/Vs, about 80 times higher than the mobility of nitrogen and oxygen ions.
In air, the ions shortly after creation attach to water molecules and CO_2 and form large slowly moving clusters. These clusters have a mobility of about 1 cm^2/Vs in atmospheric air.

2.3 Dielectric barriers

Dielectric barriers in air and oil gaps are well known for bringing improvement to the electric breakdown strength [17-19] and widely used in high voltage engineering. For example in oil insulated power transformers. Barriers help preventing short circuiting caused by the bridging of particles in the transformer oil, increasing the withstand voltage compared to an oil gap without barriers.

The increase in breakdown strength is explained as field redistribution and homogenization due to charge accumulation on the barrier surface and that the dielectric barrier represents a physical obstacle which extends the discharge path and thereby counteracts the development of a disruptive channel.
The effect of barriers depends on the shaping of barriers and electrodes, their positions in the air gap, degree of field inhomogeneity and pre-charging.

2.4 Surface insulation

Dielectric covering of electrodes can be divided into two groups; thin layers (dielectric coating), having a thickness up to some hundred micrometres, and covered electrodes with a thickness in the range of millimetres to centimetres. While coated electrodes increase the withstand voltage through reducing emissions from electrodes, covered electrodes are increasing the withstand voltage by charge accumulation reducing the electric field in the gas gap.

2.4.1 Dielectric coated electrodes

Dielectric coating can beneficially be applied to improve the breakdown strength of vacuum gaps. The thin film reduces the field emission by lowering the electric field at the electrode surfaces, suppressing electron emission. In case of an ideal insulating film, the field at the electrode surface is reduced proportional to the permittivity of the coating. Experiments done with a 2 μm SiO_x layer show an increase in dc breakdown voltage up to 100% [8]. After breakdown, uncoated electrodes were destroyed while the coated only had small (15 μm diameter) punctures and undamaged electrodes. The breakdown voltages of punctured coated electrodes were found to be 90% of the breakdown voltage of the undamaged covered electrodes.

When applying ac and lightning impulse voltage in a uniform field gap with SF_6 and high pressure (0.3 MPa), experiments show an increase in breakdown voltage of 30-88% and 18-40% respectively compared to that of bare electrodes [9]. In the same experiment different coating thicknesses were examined. A thin layer (60 – 200 μm) gave an increase in ac breakdown voltage up to 8%. Applying a thicker coating gave a further increase in breakdown voltage. The effect of the coating was found to be at its optimum when the coating was so thick that the electric stress concentration caused by the electrode roughness becomes negligible.

2.4.2 Dielectric covered electrodes

Dielectric covering of electrodes can be applied beneficially to gas gaps in a so-called hybrid insulation system. The increased breakdown strength under lightning/switching impulses, ac and dc are believed to be caused by accumulation of space charges on the dielectrically covered electrodes. As a consequence, a counteracting electric field component results, causing a reduction of the field in the air gap and an increase of the field in the dielectric layer. This increase is observed for both homogeneous and inhomogeneous electric field configurations [2, 3, 9].

Blennow [2] and Sjöberg [3] studied hybrid insulation for homogeneous electric fields in case of dc and lightning impulses. For a slowly rising dc-stressed gap, an increase in applied voltage without breakdown ranged from 50 to 250% above the voltage corresponding to critical voltage calculated for a pure capacitive electric field distribution, dependent on the air gap distance. For lightning impulses the increase varied between 70 and 350%. The discharge activities together with measurements of the discharge currents were recorded. In order to obtain improved insulation properties, the coating should be used on all electrodes and their thickness should be sufficient to withstand the largest electric stress applied to the insulation system. The permittivity of the solid insulation should be as low as possible in order to achieve low capacitance and thereby minimize the required quantity of surface charges needed to quench air gap discharges. Low capacitance also reduces the surface impacts on the coatings.

Dynamic numerical simulations of the homogeneous field were made assuming one-dimensional discharge events [2, 3]. Comparison made with experiments show a good agreement with the basic ideas behind the concept of hybrid insulation. Sjöberg et al. [20] and Serdyuk et al. [21] performed two-dimensional numerical simulations in order to explain the formation and growth of surface charges causing redistribution of the electric field within the insulation system. The formation of discharges and surface charge accumulation were described both numerically and experimentally. Both the computed and measured currents showed distinct discharge pulses indicating good agreement between estimated and measurement data. Some divergences are present, but they are explained as shortcomings in the model and experimental method inaccuracies.

The breakdown voltage for a rod-plane gap in SF_6 was investigated in [22, 23]. The rod was covered with epoxy on the hemispheric part and 30 mm upwards. The insulation thickness was varied between 10 - 30 mm and the electrode distance was varied up to 200 mm. Tests were preformed for both ac voltages and lightning impulses. For ac, the maximum increase of breakdown voltage was found to be 95% and for lightning impulses 68%. At breakdown the solid insulation was not punctured but a flashover occurred along the insulating surface. The observed increase in breakdown voltages is believed by the authors to be caused by the reduction of the maximal electric field around the tip of the rod and thus suppression of electron emission from the tip. Surface charge deposition on the rod tip was studied with the use of black copier toner and found to be about 4 nC/cm^2.

Baldo and Pesavento [24] investigated discharge development under lightning impulses for a coated electrode in air by means of video camera images and electric field

measurements. The experimental set-up consisted of a sphere/plan air gap where the sphere diameter was 20 or 50 mm and air gap varied from 15 to 200 mm. The sphere and supporting rod was covered with a 2.5 mm thick layer of epoxy-based resin while the plane was left uncoated. An increase in corona inception voltage ranging from 20 to 60% was achieved depending on the sphere diameter and the voltage used, while increase in positive breakdown voltage was higher than 100%. The authors have also done repeated voltage applications with lightning impulse voltages with different conductivities of the coating without removing charges after each shot. Tests showed that particularly for the coating with high resistivity (10^{13} Ωm), discharges at a given voltage level, were related to the amount of charging during the pervious lightning impulse voltage application. Due to surface charge accumulation on the insulating surface, succeeding shots at the same voltage resulted in a more diffuse corona. In case of breakdown, the puncture never occurred at the shortest distance of the air gap, but approximately 200 mm above the covered sphere. The corona activity does not differ from that of streamers developing in contact with an electrode. However, in the subsequent phase, it differs as there is no indication of the formation of any leader channel, except for an increased filament luminance as the voltage increases. As the voltage was increased, discharges were also observed propagating upwards along the covered supporting rod. The authors assume that the ionization along the rod is supported by the capacitive and charge induced field. The stress along the surface can then reach values causing a puncture of the resin, initiating a leader formation followed by breakdown of the insulation system. After a puncture, the withstand voltage was still quite high, and breakdown always occurred when the voltage applied was so high that the discharge activity reached the puncture. Tests were repeated with reduced air gaps of 15 and 100 mm. Breakdown did not occur even with an average electric field strength very close to the ionization limit of air over the entire air gap. Higher voltages caused breakdown to take place without damaging the insulating cover as the disruptive channel formed in the air close to the insulating surface bridging the insulating surface.

Mizuno et al. [25] describe experimental examination of the electric performance of a rod plane air gap under lightning impulse with the rod covered with a 10 or 20 mm thick coating. The length of the covered rod was varied between 100 and 300 mm while the gap distance was kept constant at 100 mm. For positive impulses the increase in breakdown strength of the covered rod (covered length 100 mm) was approximately 40% while the increase for negative impulses was approximately 30%. Variation of the covered length with 10 mm thick coating showed a small increase for positive impulse voltages while for negative impulse voltages the increase was linear with the covered length. For a thicker coating, 20 mm, the breakdown voltage was found to be independent of the covered length, but strongly depends on the electric field at the tip of the rod. Light intensity and still photos were recorded for partial discharges and breakdown for both positive and negative lightning impulses. Both during positive and negative impulse voltage application discharges occurred round the hemisphere area of the rod. Discharge activity during positive lightning impulse voltages was more dispersed around the tip than discharge activity during negative lightning impulse voltages.

The electric performance of an air or nitrogen (N_2) insulated system has been investigated in [26]. A semi-hemispheric rod was covered with silicone rubber. Its thickness was varied in the range of 18 mm with gap distance of 50 and 100 mm and pressure between 0 and 0.5 MPa. Also the diameter of the rod was varied. For all pressures an increase in breakdown strength was found. The maximum increase in breakdown strength in air and nitrogen (N_2) was found to be maximum 50% at 0.2 MPa. The experiments also showed that the breakdown strength rose with increasing layer thickness. At small gap distances, the effect of coating was found to be enlarged since the maximum value of the electric field in the air/N_2 gap is reduced. The increase-ratio in breakdown strength and reduction-ratio of the maximum electric field around the tip are not identical, indicating that the breakdown voltage is determined not only by the maximum electric field strength, but also by surface charging.

The development of creeping discharges has been studied by Darvenzia [27] using two adjacent XLPE covered conductors crossing at a 90º angle to each other with air gaps varying between 3 and 22.5 mm. The objects were tested with impulse voltage applying 25 lightning impulses at each level. After each series of impulses, the surface charge on the XLPE was measured. In the case of no breakdown, there was no measurable surface charge on the insulating surface. When the voltage was raised until a breakdown eventually occurred, no further breakdowns were observed with subsequent applications of voltage at the same level. Due to the accumulated surface charges, the voltage had to be raised by between 25 and 40% before another breakdown was observed. The amount of the charge deposited increased with increasing voltage. If the voltage was reversed after a breakdown, the initial charge was progressively replaced by charge of the opposite polarity as more and more charges were trapped at the surface.

Walfridsson et al. [28, 29] addressed the problem of creeping discharges along the insulating surface. In order to reduce the problems with discharge currents and hereby increase the lightning impulse breakdown strength of the system, cable terminations were utilized. The increase in breakdown strength was 75% and 25% for positive and negative lightning impulses respectively. The mechanisms for flashover along insulator surfaces have been reviewed in [30]. Positive streamer discharge propagation in air and along an insulating surface have been investigated experimentally and simulated in 3D in [31, 32]. The simulations showed that when streamer discharges are propagating along an insulating surface, more branches developed in direction of the insulating surface. This is explained as a consequence of the field enhancement in the air caused by the dielectric constant of the surface due to the polarization charge of the dielectric which attracts the developing branches. Due to limited computer memory the 3D-simulations were only run to the 6^{th} step of branching. Experiments with different insulator surfaces showed that the streamer propagation is dependent on both the permittivity of the solid insulation and surface properties. Streamer propagation simulations were also done considering the effect of charges deposited on the insulating surface. The dielectric constant influences the electric field at the tip of the streamer and the surface charge could either enhance or reduce the electric field dependent on its polarity.

2.5 Surface charge measurements

In order to get a better overview over the total stress situation before, during and after discharges, it is essential to measure the remaining surface charge. It is, however, difficult to quantitatively measure such charges. The application of any probe is likely to alter the electric field and measurements might also have to be performed at distance in order to prevent discharges and electric breakdown.

For thin specimens the surface charge can be found directly as a function of probe response and capacitances between the probe and surface and earth [25], i.e. the probe response is only dependent on the surface charge underneath the measuring position. For thicker specimens and measurements at a greater distance (more than a few millimetres) the probe response depends not only on the surface charge underneath the probe, but also from the surrounding surface charges [33]. The evaluation of measurements of thick specimens and specimens with high surface charge density is therefore complicated.

In this examination several principles for measurement of surface charges are briefly described.

Dust figure technique

A classical method is the dust figure technique introduced by Lichtenberg in 1777. The measuring principle is based upon (Xerox) powder that is sprinkled out on the surface and attaches to the surface charges. This method only gives a rough estimate of charge distribution, density and polarity.

Capacitive probe

For non-contact measurements, a field-sensing meter or a capacitive probe is usually used for measurements on thin objects. Basically there are two different kinds of probes.

The first type measures induced charge or floating potential of the probe. The probe usually consists of a sensor plate surrounded by a guard ring normally directly earthed. The sensor is generally earthed through a known capacitance as shown in Fig. 2.4.

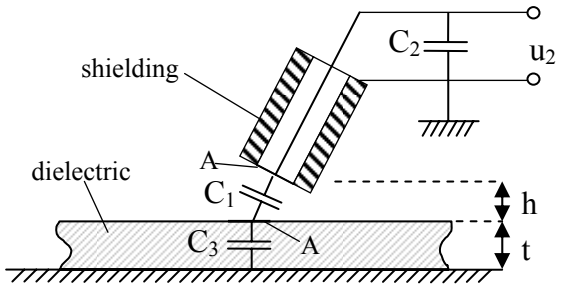

Fig. 2.4 – Capacitive probe for surface charge measurements. A is the area of the surface area being measured, C_1 the capacitance between probe and measured surface area, C_3 the capacitance of the insulation material between surface area and earth electrode and C_2 the capacitance between earthed shielding and probe response.

Given that the capacitance is sufficiently large to keep the sensor virtually earthed, the probe is referred to as a Q-probe. A probe with a floating potential is referred to as a P-probe.

The second type measures the potential close to the surface charge, adjusting the probe potential until it equals the point being measured. This method requires that the measured potential does not vary during the approach of the probe.

Field mill

Another method for non-contact measurement is the use of a field mill. Field lines induced by the surface charges terminate at the measuring electrode. An rotating vane *v* interrupts the field lines *n* times per second and the electrode experiences a fluctuating electric field which generates an alternating current *i* in the measurement circuit.

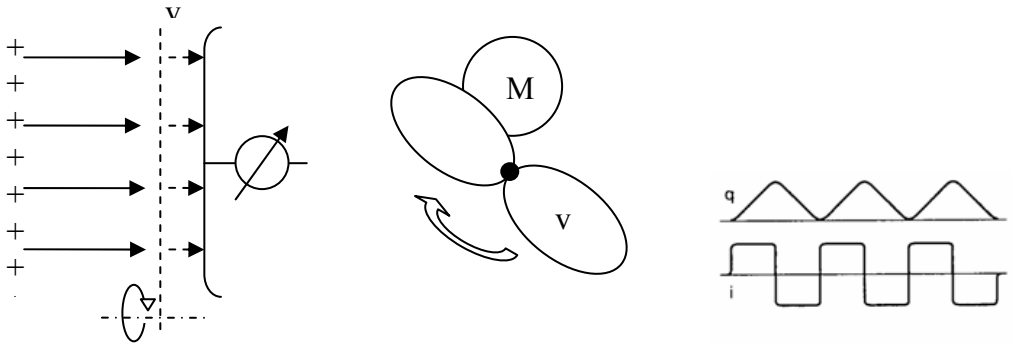

Fig. 2.5 - Field mill with a rotating vane.

The relation between the charge q and current *i* is given by:

$$i = \frac{dq}{dt} \tag{2.18}$$

Alternatively, a vibrating sensor plate can be used. The change in capacitance for a given voltage will induce a current. The relation between current and induced charge is given in Eq. (2.18).

Pockels probe

Using a Pockels surface potential probe as shown in Fig. 2.6, the surface charge or potential distribution can be measured. The probe is based on the Pockels effect (Pockels electro-optic effect) of a crystal and produces birefringence in an optical medium induced by a constant or varying electric field. The birefringence is proportional to the electric field.

The probe presented here uses a $Bi_4Ge_3O_{12}$ (BGO) crystal. At the top end face of the BGO a transparent conductive is used as the earthed electrode. At the bottom end face a metallic mirror coating is used as sensing electrode. The induced potential is measured by the Pockels effect of the BGO crystal whose optical orientation is arranged having sensitivity on the field component parallel to the light direction. The probe can be regarded as a P-probe (see capacitive probes).

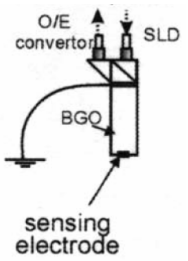

Fig. 2.6 – Pockels probe [49]

2.5.1 The λ-method

In order to analyse the probe response in the case of high surface charges and thick insulation surfaces, the contribution from every dielectric surface element dS on the probe has to been taken into account. A. Pedersen introduced a probe response function; the λ-function [1, 34] to facilitate this. The function describes the relation between the Poissonian induced charge dq on the probe and the deposited surface charges dQ on the dielectric surface:

$$dq = -\lambda dQ = -\lambda \sigma dS \tag{2.19}$$

The total induced charge q on the probe becomes

$$q = \iint_{S_0} \lambda \sigma dS \tag{2.20}$$

where λ is a dimensionless function. The λ-function is governed by the Laplace equation, σ is the surface charge density of the small surface element dS on the solid dielectric, where the boundary conditions are λ = 1 at the sensor plate of the probe and λ = 0 at all other electrodes.

Using electric field calculations, the value of the λ-function for each probe position can be computed. With N probe positions, N surface elements are needed which require N^2 parameters.

By introducing a Λ-matrix, both the geometrical scanning procedure and the relevant λ-function can be taken into account. For each position i, the probe response p_i is a sum of the weighted charge on each surface element j, yielding

$$p_i = \sum_j \Lambda_{ij} \sigma_j \tag{2.21}$$

where σ_j is the charge density on surface element j. The λ_{ij} coefficient is given by:

$$\Lambda_{ij} = \iint_S \lambda_i dS \tag{2.22}$$

λ_i is the λ-function measured at a certain probe position i. For a measured probe response p and given Λ, the surface charge density σ can be found by inverting the Λ-matrix:

$$\sigma = \Lambda^{-1} p \tag{2.23}$$

However, during practical measurements of high voltage experiments this method has been shown to be very sensitive to small deviations in the measurements [35]. For high surface charge densities and thick insulating surfaces, a large distance between the probe and the insulating surface is necessary. Small variations in the measured probe response p may then cause large changes in the calculated charge distribution.

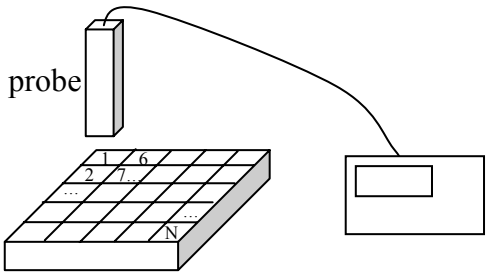

Fig. 2.7 – Division of insulating surface into segments. The probe positions have the same numbering as the surface element under the probe. The elements do not have to be squares or to have an equal number of horizontal and vertical divisions.

A similar method has been developed by Takuma et al. [36], which also requires the solution of a matrix equation:

$$W_p(i) = \sum_{j=1}^{N} A(i, j)\sigma(j) \tag{2.24}$$

where $W_p(i)$ is the probe response at measuring point i, $\sigma(j)$ is the surface charge density at surface segment j and N is the total number of surface segments. The function A(i, j) is the response at probe position i due to a charge density at surface segment j. The coefficient is dependent on the system geometry and the A(i, j) is determined by numerical field calculations. Although the procedures for determining the A and Λ matrixes are somewhat different, the two matrices are identical and thus, the same problem with perturbations of the probe response applies here as well.

A method for improving the evaluation of measurements from an electrostatic probe (Pockels probe) suppressing noise is presented in [37-39]. Measurements have been carried out on a cone spacer exposed to a dc field in SF_6. Based on Pedersen's λ-method, an estimated solution $\hat{\sigma}$ of the surface charge density can be calculated using:

$$\begin{aligned}\hat{\sigma} &= \left([\Lambda]^T [\Lambda] + \gamma [I] \right)^{-1} [\Lambda]^T \, p \\ &= [G] p\end{aligned} \tag{2.25}$$

where the matrix [I] is a unit matrix and γ a small constant corresponding to the signal-to-noise ratio (SNR). Here 0.3% of the largest eigenvalue of the covariance matrix $[\Lambda]^T[\Lambda]$ was adopted as value of γ [39]. This method is suitable for measurements at a short distance, which can be made with a Pockels probe. But when using probes requiring a larger measurement distance, this method is no help in improving the estimation of the surface charge distribution.

2.6 Summary and scope of work

The phenomena related to charge accumulations of barriers and surface layers has been observed and reported in a number of papers. The conclusions drawn in the literature are that for both homogeneous and inhomogeneous electric fields, the concept can be applied beneficially to high voltage systems in order to increase the lightning impulse withstand voltage. The increase in withstand voltage depends on the geometry and shape of the electrodes in the insulation system and the shape of the applied voltage. The increase of withstand voltage for hybrid insulation can be summarized as shown in Table 2.2.

Table 2.2 – Increase in withstand voltage for hybrid insulation system (gas-solid) compared to a gas-insulated system with same electrode configuration for dc and lightning impulse.

Applied voltage	**Increase of withstand voltage**	
	Homogeneous field	**Inhomogeneous field**
DC	air: 50-250% [2, 3]	air: >100% [24]
Lightning impulse	air: 70-350% [2, 3]	air: 30-40% [25] SF_6: < 95% [22, 23] N_2(pressurized): 50% [26]

Hybrid insulation in case of homogeneous fields is well examined in the work of J. Blennow [2] and M. Sjöberg [3]. Modelling of discharges and charge distribution has been carried out and comparisons with experimental observations and measurements show a good correlation.

No comparable work to homogeneous fields has been done for hybrid insulation in inhomogeneous fields. Experimental results confirm the increased withstand voltage also for inhomogeneous fields, but further investigation on the phenomena has not been presented.

For thin objects, the surface charge can be found directly while for thick objects and objects with a relatively high surface charge, measurements have to be carried out at a greater distance to avoid discharges or flashover to the probe. This implies that in addition to the surface charge directly underneath the probe its response is also determined by the surrounding charges. The λ-method of A. Pedersen handles this problem in a mathematically stringent way, but the method is very sensitive to perturbations in the measurements, making the λ-method in its current form not applicable for practical measurements. Some methods to improve the results obtained by the λ-method exist, but are only suitable for short distance measurements (distance probe – surface a few millimetres). For measurements of a greater distance (10-20 mm), no methods are found in the literature for getting a reliable estimation of the surface charge distribution.

Scope of work

The main objective of the experiments is to study the influence of charge formation in the air gap and on the covered electrodes in a non-uniform electric field during and after lightning impulse application of both polarities.

In order to increase the knowledge of hybrid insulation in inhomogeneous electric fields, experiments will be carried out on a hemispheric rod covered with a layer of solid insulation. Discharge activity will be studied by measuring voltage, discharge current and recording the discharge activity using a digital high speed camera.

Surface charge accumulation after discharges will also be studied. Here, new methods for the evaluation of surface charge measurements will be introduced, tested and assessed.

3 EXPERIMENTAL METHODS

This chapter presents the experimental set-up and test procedures for applying lightning impulse and recording of light emission from air discharges, current and voltage pulses.

3.1 Experimental set-up

3.1.1 Impulse application, voltage, current and light measurements

Test objects were stressed with a standard 1.2/50 μs lightning impulse according to the IEC 60060 standards.

For voltage application, a 1.2 MV Marx impulse generator has been used. A Proxitronic high-speed camera was used to record the accumulated emission of light from discharge activities in the air gap during voltage application. The camera was triggered simultaneously with the Marx generator. The open time of the camera could be varied from a few microseconds to milliseconds. To facilitate the detection of light emission, the set-up was enclosed in black curtains. The camera was connected to a PC for storage of the recorded images.

A sketch of the experimental set up is shown in Fig. 3.1 while a typical test electrode configuration is shown in Fig. 3.2. The discharge current was measured by means of 80 x 80 mm square electrode. The electrode was connected to a 50 Ω coaxial cable terminated with the internal 50 Ω resistance of the oscilloscope to avoid reflections. In addition, two attenuators of -6dB and -10dB were connected in series with the coaxial cable to reduce the energy of the current pulse in case of breakdown of the test object, together with over-voltage protection at both coaxial cable terminals.
For voltage measurement, a resistive voltage divider was used, connected with the oscilloscope through a 50 Ω coaxial cable and terminated with the internal 50 Ω resistance of the oscilloscope.
Recorded voltage and current graphs were stored on the same PC for later analysis.

All experiments performed during this work were done at room temperature at atmospheric pressure.

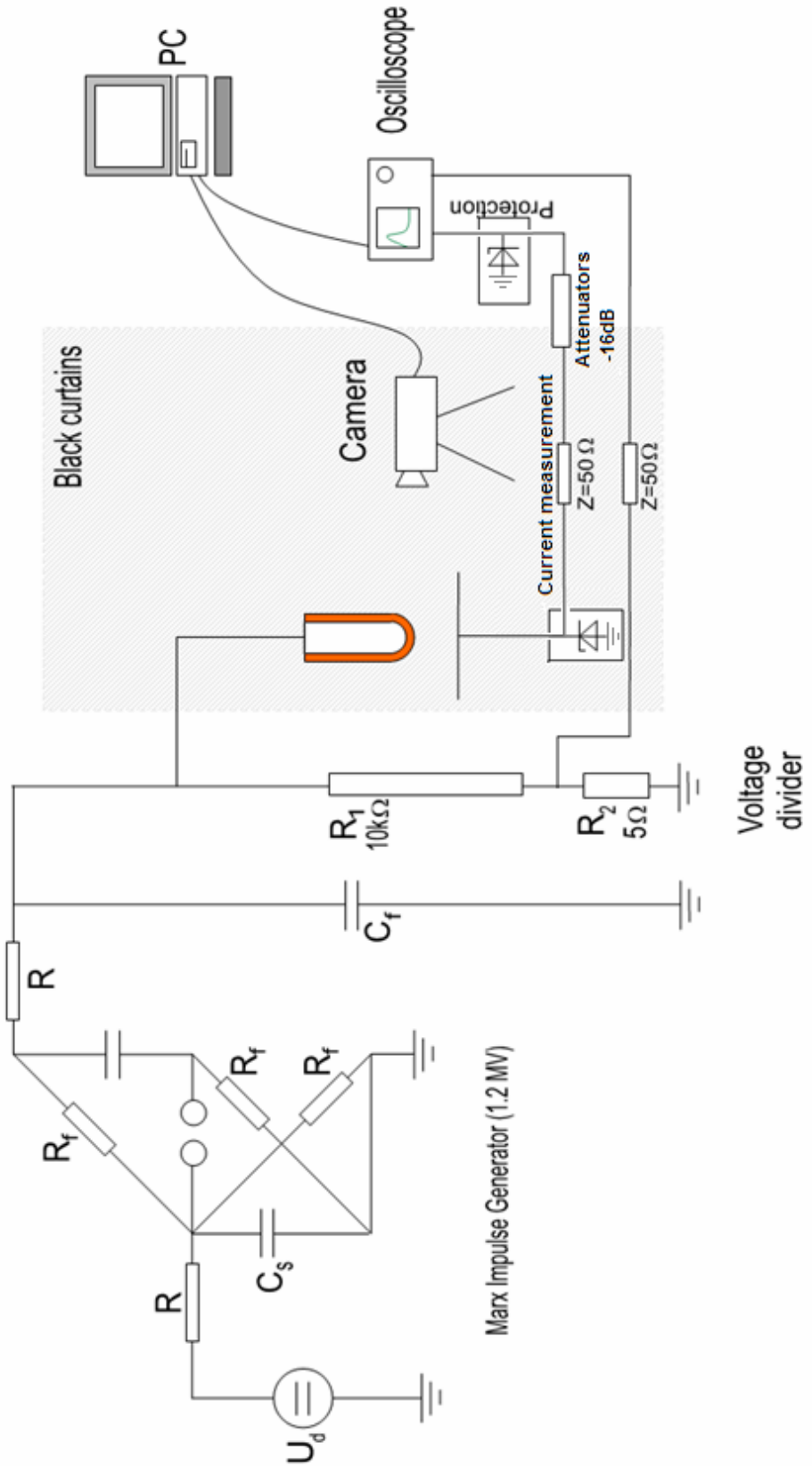

Fig. 3.1 - Experimental set-up for surge impulse testing of rod-air gaps, showing equipment for recording applied voltage, discharge current and light emission. To avoid damage in case of breakdown of the insulation system, over-voltage protection was used at both coaxial cable terminals.

3.1.2 Samples and materials

The basis for the experiments has been a rod-plane air gap with a hemispheric rod. The rod had a radius of 8 mm. The rod was used bare, as a reference, and covered with silicone rubber (SIR) or polyamide (PA66). In addition, the SIR covered rod was also used in two modified versions:

- iodine doped to alter the conductivity
- conductive layer around the tip

The bare rod and SIR covered rods were made of aluminium while the polyamide covered rods were made of copper.

Silicone rubber covered rod

The hemispheric aluminium rod was covered with a 3 mm thick layer of solid insulation as shown in Fig. 3.2. The silicone rubber used is room temperature vulcanizing (RTV) type M4601 from Wacker. The SIR was cast on to the rod using a specially designed Teflon mould. During casting, the mould is placed in an evacuator, evacuated and pressurized 3-4 times in order to eliminate internal gas bubbles in the silicone rubber.

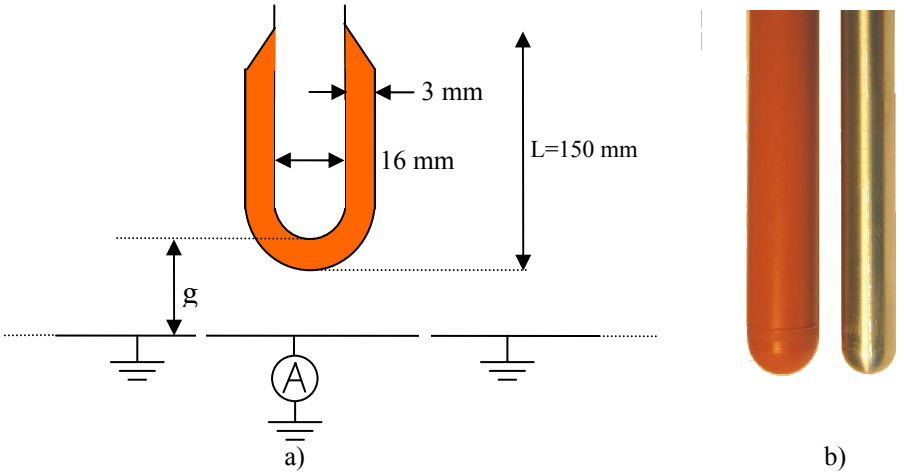

Fig. 3.2 - a) Typical electrode configuration used for the experiments.
b) Picture of SIR-covered and bare aluminium electrodes used in experiments.

The surface charge decay depends on the material properties of the solid insulation, i.e. the conductivity and permittivity. The conductivity was changed to study the influence of material properties on the charge decay. Through iodine doping of the SIR, a relatively high conductivity can be achieved resulting in a lower time constant τ of the charge decay. To achieve this, the rod with SIR was placed in an airtight glass bulb together with a few grains of solid iodine and placed in an oven at 40°C for 10-12 hours. The iodine vaporizes and diffuses into the solid insulation creating extra holes, that enhance the conductivity.

Silicone rubber covered rod with conductive layer around the tip

A conductive layer on the solid insulation of the hemispheric part of the rod was applied, as shown in Fig. 3.3. A thin layer of silver paint was used as the conductive layer.

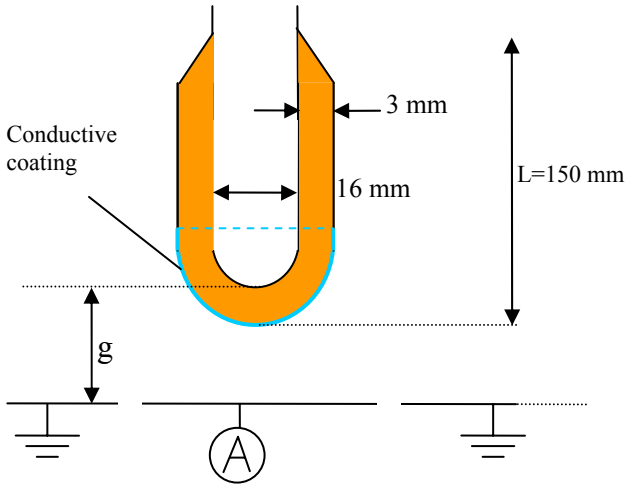

Fig. 3.3 – Test object with conductive layer on the tip.

Polyamide covered rod (PA66)

The samples were cast by ABB and have an insulation thickness of 4 mm instead of 3 mm as with the SIR covered rods.

3.1.3 Conductivity measurement

A dc voltage was applied to a rod and the dc current measured as a function of temperature and applied electric field to determine the apparent conductivity σ_a of the solid insulation used in this experiment,. The set-up was placed in an oven for easy regulation of the temperature. The stable dc current was recorded after 2-3 hours of voltage application.

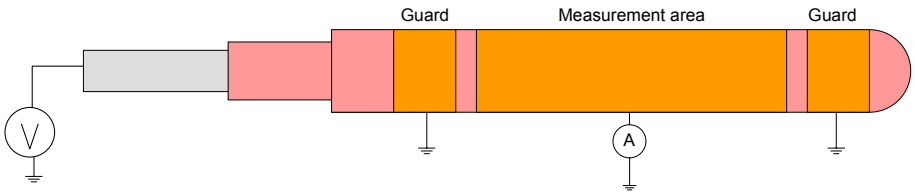

Fig. 3.4 – Measurement of conductivity. For measurement of the current, an electrometer was used.

3.1.4 Measurement of charge decay

The charge decay after a lightning impulse was measured by using a field mill. After applying a lightning impulse and earthing the rod, the field mill is placed in the plane under the rod as shown in Fig. 3.5.

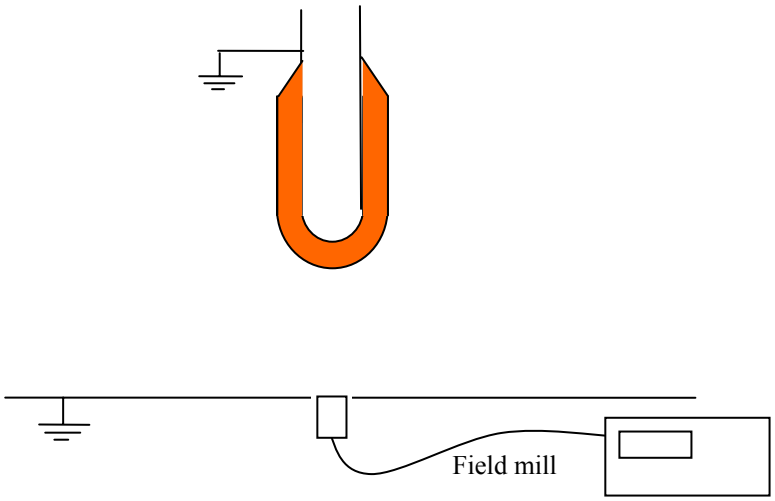

Fig. 3.5 – Set-up for surface charge decay measurement. The field mill was put on place after application of lightning impulse.

The measured electric field is related to the surface voltage of the rod. For calibration of the field mill, a covered rod with a conductive layer around the tip was used and energized with a dc voltage.

3.1.5 Measurement of surface charges

In order to measure the surface charge distribution on the insulating surface, the electric field along a cylinder around the rod was measured. After applying a lightning impulse and earthing the rod, the field mill was mounted outside a hole in a cylinder, surrounding the rod as shown in Fig. 3.6. As it is essential to take the measurements as close to the surface of interest as possible, the field mill was placed in a cylinder wall. This was done in order to avoid that the sharp edges of the mill causing any discharges that would damage the field mill and measurements. At the same time, using a cylinder simplifies the electric field calculations with FEM-software since the problem is rotationally symmetric (and thus 2D) instead of a 3 dimensional one. Another advantage is that the calculated relation between surface charges and probe responses is the same no matter the distance between the rod and plane during the application of the impulse voltage.

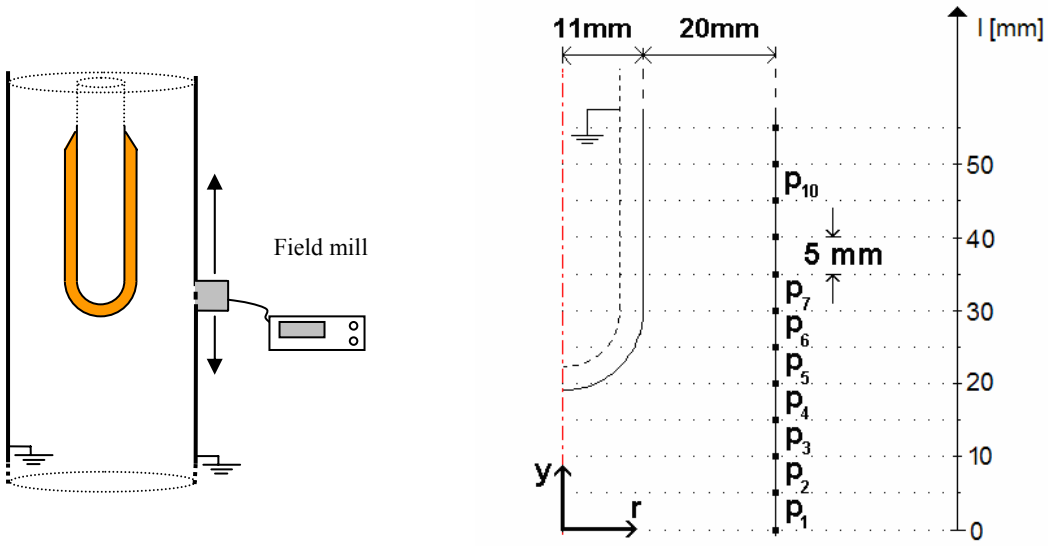

Fig. 3.6 –Left; set-up for measurements of surface charges. The cylinder with the mounted field mill can be moved up and down. Right; appurtenant probe positions.

3.2 Measurement procedures

After each voltage application and measurement of surface charges, the remaining surface charges were removed. This was done by leading an earthed conductive glove over the solid insulation discharging the surface charges. Afterwards, dust and undesirable particles were removed from the surface by washing it with a soft cloth with isopropanol. A handheld electrostatic field mill was used to verify that the surface charges have been properly removed.

For FEM-calculations, commercially available software, COMSOL Multiphysics [40], was used.

4 EXPERIMENTAL RESULTS

In an air-insulated inhomogeneous gap, positive lightning impulse is normally the dimensioning criteria as the breakdown voltage is lower for positive than negative voltage. First the increase in withstand/inception voltage was recorded. Typical discharges for both positive and negative voltage applications are studied. The propagation of discharge activity and charge decay is also studied. Finally the influence of conductivity on the behaviour of the insulation system is studied.

4.1.1 Inception voltage

The standard up-and-down method was used to determine the correlation between electrode distance and discharge inception voltage. When applying a positive lightning impulse to a rod plane gap with bare electrodes, a discharge channel was found to directly lead to breakdown of the insulation system. For covered rods the discharge inception voltage was lower than the breakdown voltage and dependent on how much of the rod that is covered with solid insulation.

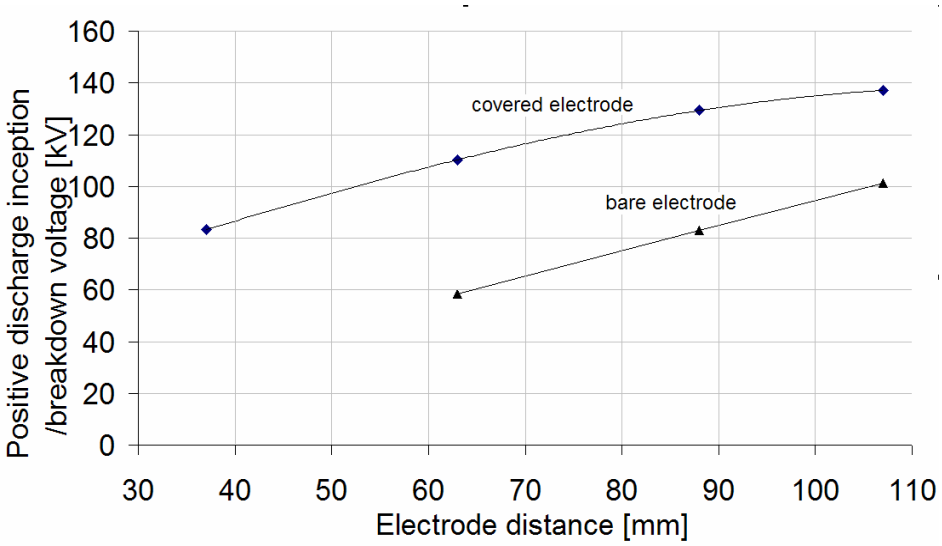

Fig. 4.1 – Discharge inception during application of positive impulse voltage as function of air gap distance: with insulating layer (♦), without layer (a bare rod) (▲). Without an insulating layer, discharge activity leads to breakdown of the insulating system.

The results obtained in Fig. 4.1 show that the withstand voltage for positive impulses improves when the electrode is covered with a layer of solid insulation. The values for the covered electrode are the voltages where visible discharges are recorded. The breakdown voltage for a covered electrode is higher than the inception voltage.

4.1.2 Positive impulses

Fig. 4.2 shows a typical image of accumulated discharge activity in an air gap during the application of a positive impulse voltage to the rod of the gap. The corresponding measured voltage and current is shown in Fig. 4.3.

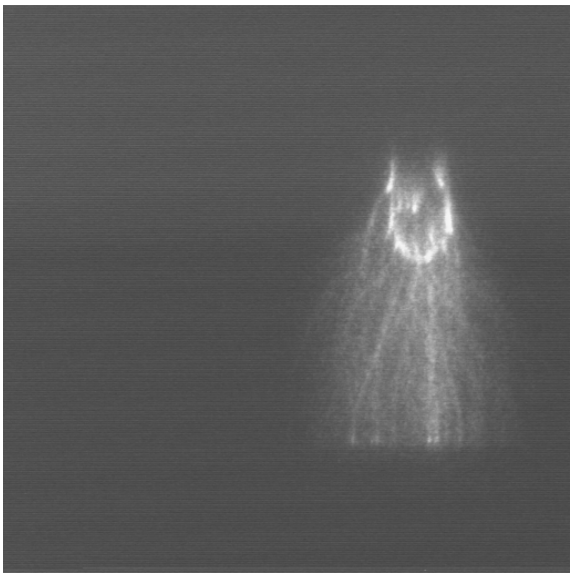

Fig. 4.2 - Video image of air discharges during positive impulse voltage (electrode distance 63 mm, applied voltage: U = 78.0kV). The corresponding current and voltage graphs are shown in Fig. 4.3. The discharges cover the air gap between the rod and plane without breakdown of the insulation system.

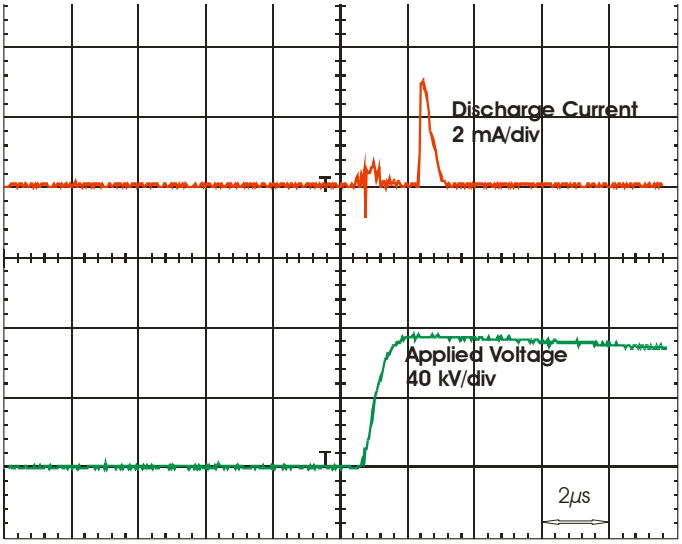

Fig. 4.3 – Voltage and current measurement. The oscillations of the first μs are due to the ignition of the spark gaps of the Marx impulse generator.

As seen in Fig. 4.3 no breakdown of the insulation system occurred even though the discharges bridge the air gap as seen in Fig. 4.2. The current measured at the plane has a peak of about 3 mA. The oscillations in the first microseconds during voltage application is due to the ignition of the spark gaps of the Marx impulse generator and displacement current.

Another example is shown in Fig. 4.4. Here, there is positive discharge activity at a larger electrode distance and higher discharge activity than in the previous image. The corresponding current and voltage trace is shown in Fig. 4.5.

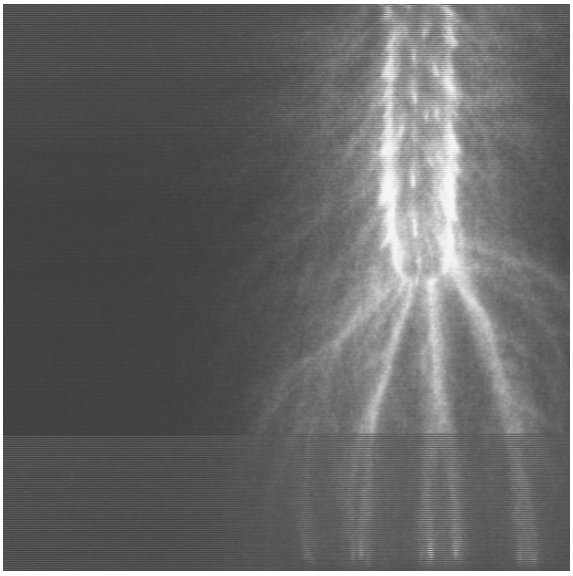

Fig. 4.4 - Video image of air discharges during positive impulse voltage. Electrode distance 91 mm, applied voltage 123 kV. The corresponding current and voltage graphs are shown in Fig. 4.5.

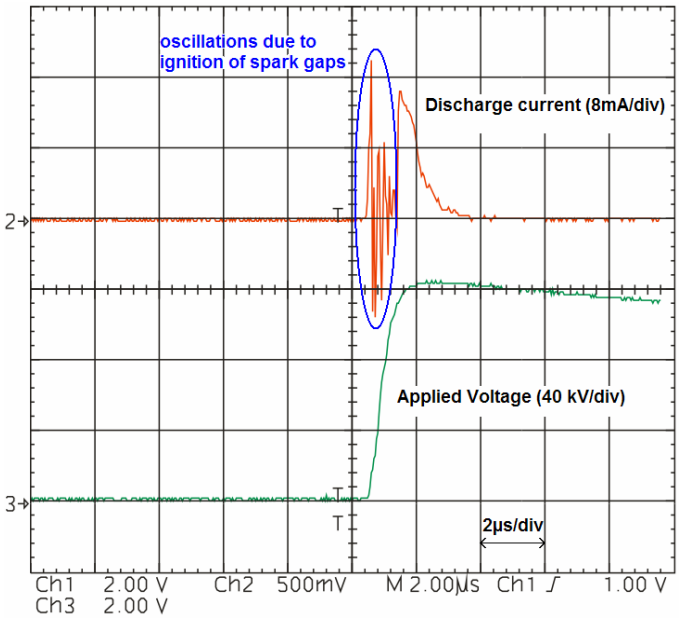

Fig. 4.5 - Voltage and current measurement. The oscillations of the first µs are due to the ignition of the spark gaps of the Marx impulse generator.

In this case the discharge activity is spread higher upwards along the rod surface and also covers a greater part of the air gap. The current trace in Fig. 4.5 shows a higher peak value and longer lasting current than what is the case in the first example of Fig. 4.2. This can be explained by the higher level of activity covering a greater part of the air gap.

4.1.3 Negative impulses

The graphs presented in Fig. 4.6 and Fig. 4.7 show video images of negative discharge activity and voltage and current trace respectively.

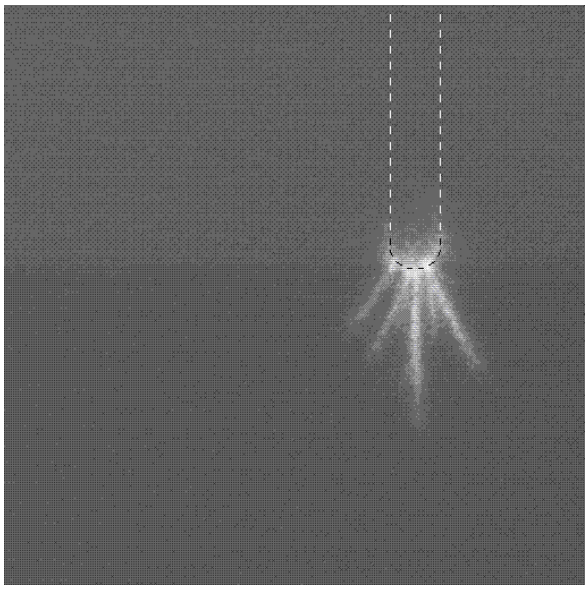

Fig. 4.6 – Video image of air discharge activities during negative impulse voltage. Electrode distance 63 mm and applied voltage -90.0 kV.

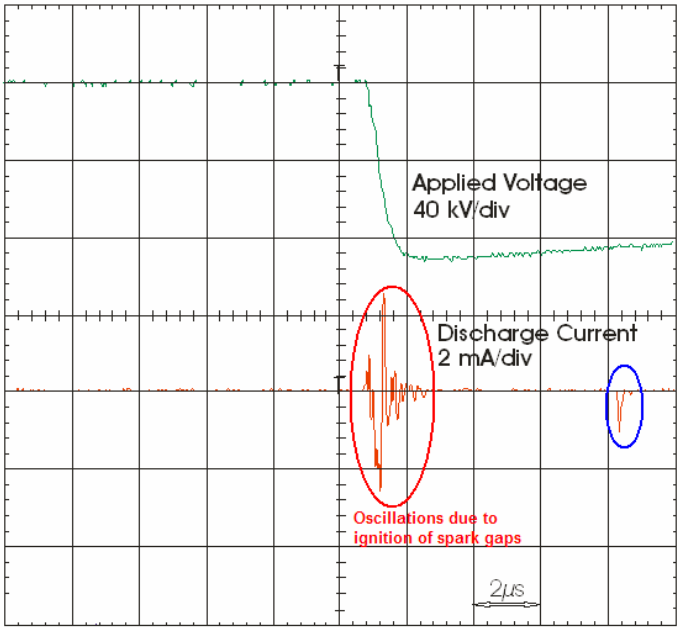

Fig. 4.7 - Voltage and current measurement for a negative impulse. The discharge current pulse is encircled in blue. The oscillations of the first µs are due to the ignition of the spark gaps of the Marx impulse generator. Corresponding video image in Fig. 4.6.

Another example of discharge activity during application of negative impulse voltage is shown in Fig. 4.8 with the corresponding voltage and current trace shown in Fig. 4.9.

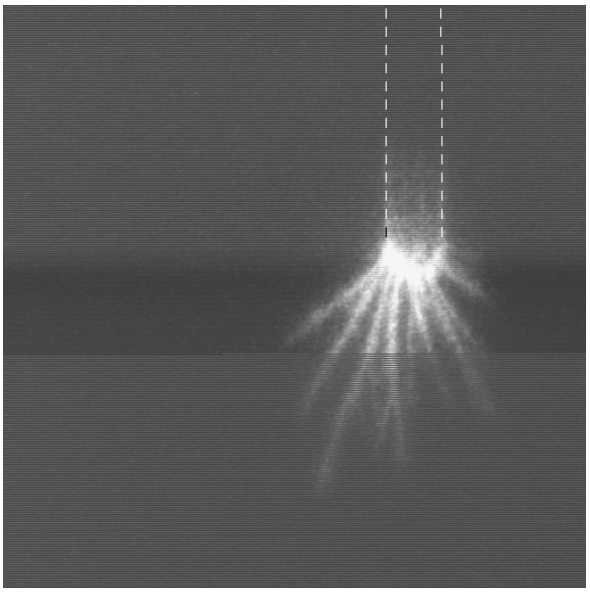

Fig. 4.8 - Video image of air discharge activities during negative impulse voltage. Electrode distance 63 mm and applied voltage -102 kV.

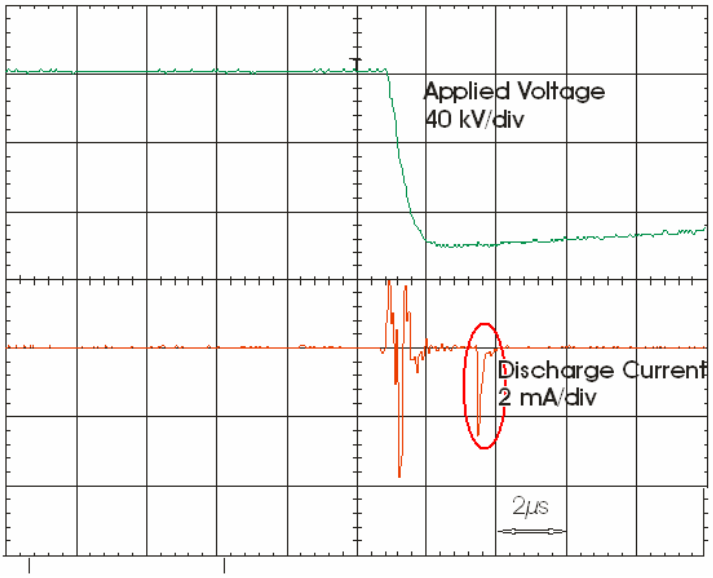

Fig. 4.9 - Voltage and current measurement for a negative impulse. The discharge current pulse is encircled. The oscillations of the first µs are due to the ignition of the spark gaps of the Marx impulse generator. Corresponding video image in Fig. 4.8.

The main difference between discharges occurring during positive and negative impulse voltage is that the discharge activity in case of negative rod is concentrated around the tip of the rod. Another distinctive difference from positive discharges is that the streamers are fewer and thicker and rarely form branches. The discharges here are like the discharges occurring during positive lightning impulses, spreading up along the rod, but this discharge activity appears more diffuse. The measured current peak for discharges under negative lightning impulses is generally much smaller both in peak value and duration than during positive impulses. Discharges during negative impulse

voltages are normally formed at the beginning of the tail while discharges during positive impulses are normally observed around the peak voltage of the lightning impulse.

4.1.4 Discharge creepage distance

As seen from the positive discharges in Fig. 4.2 and Fig. 4.4 and for negative discharges in Fig. 4.6 and Fig. 4.8, the discharge activity covers the region around the tip where the electric field is at its highest and up along the rod where the electric field is initially not high enough to cause discharges. This is particular easy to see in the case of a positive impulse voltage in Fig. 4.10. Here also the initial electric field distribution is calculated with the use of FEM software and compared with the video image of discharge activity in the air gap.

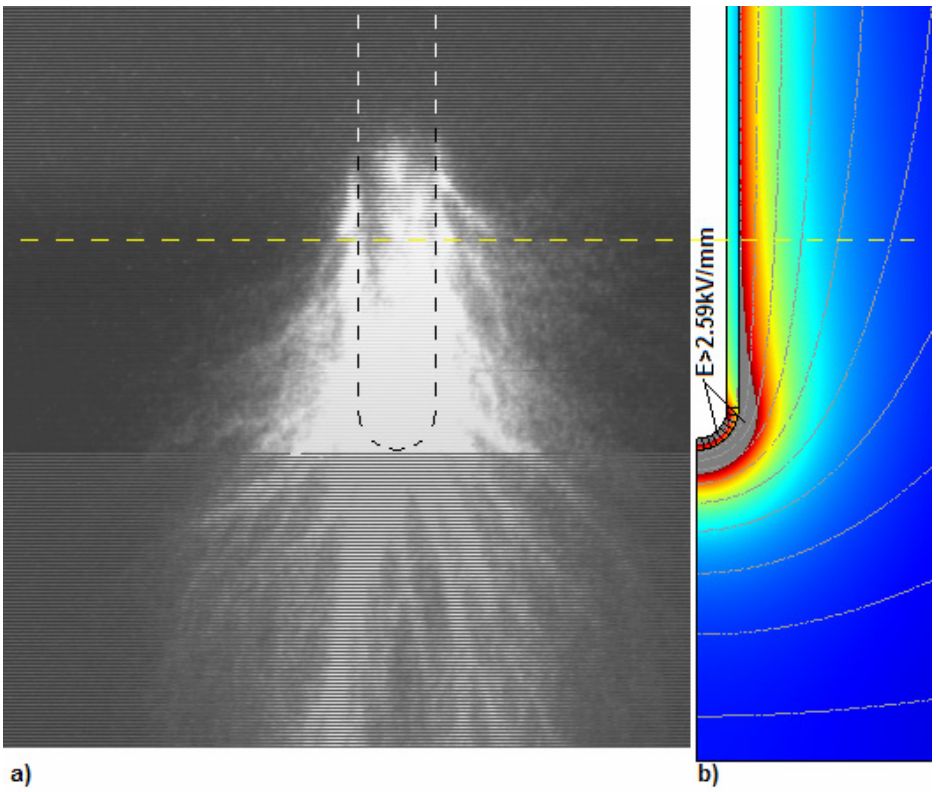

Fig. 4.10 - Comparison between calculated electric field strength and discharge activity (the stripes are due to art-effect of the camera) for a positive lightning impulse application (98.6 kV). The grey area around the tip in the right figure marks where the field is above discharge inception value (2.59 kV/mm). The yellow broken line indicates up to what point along the rod surface discharge activity is expected based on avalanche calculations using Eq. (2.16).

The discharge activity goes further up along the rod than expected based on discharge calculations (Eq. (2.16)). This can be explained as follows: the discharges are initiated where the field reaches the inception value (grey area in Fig. 4.10 b) and follow the field lines towards the earthed plane electrode. Since the rod during voltage application is positive, negative charges are attracted towards the insulating surface following the electric field, and accumulated as surface charges (Eq. (2.2)). These charges cause an electric field component to be directed parallel to the surface driving the discharge activity further up along the rod. In addition, ionization due to emitted photons from

discharge activity nearby is contributing spreading of the discharges upward along the rod.

How far the discharge activity propagates upwards along the rod is dependent on both the electrode geometry and the voltage applied. In Fig. 4.11 an example of this is given for a fixed electrode distance (86 mm) with different impulse voltages applied.

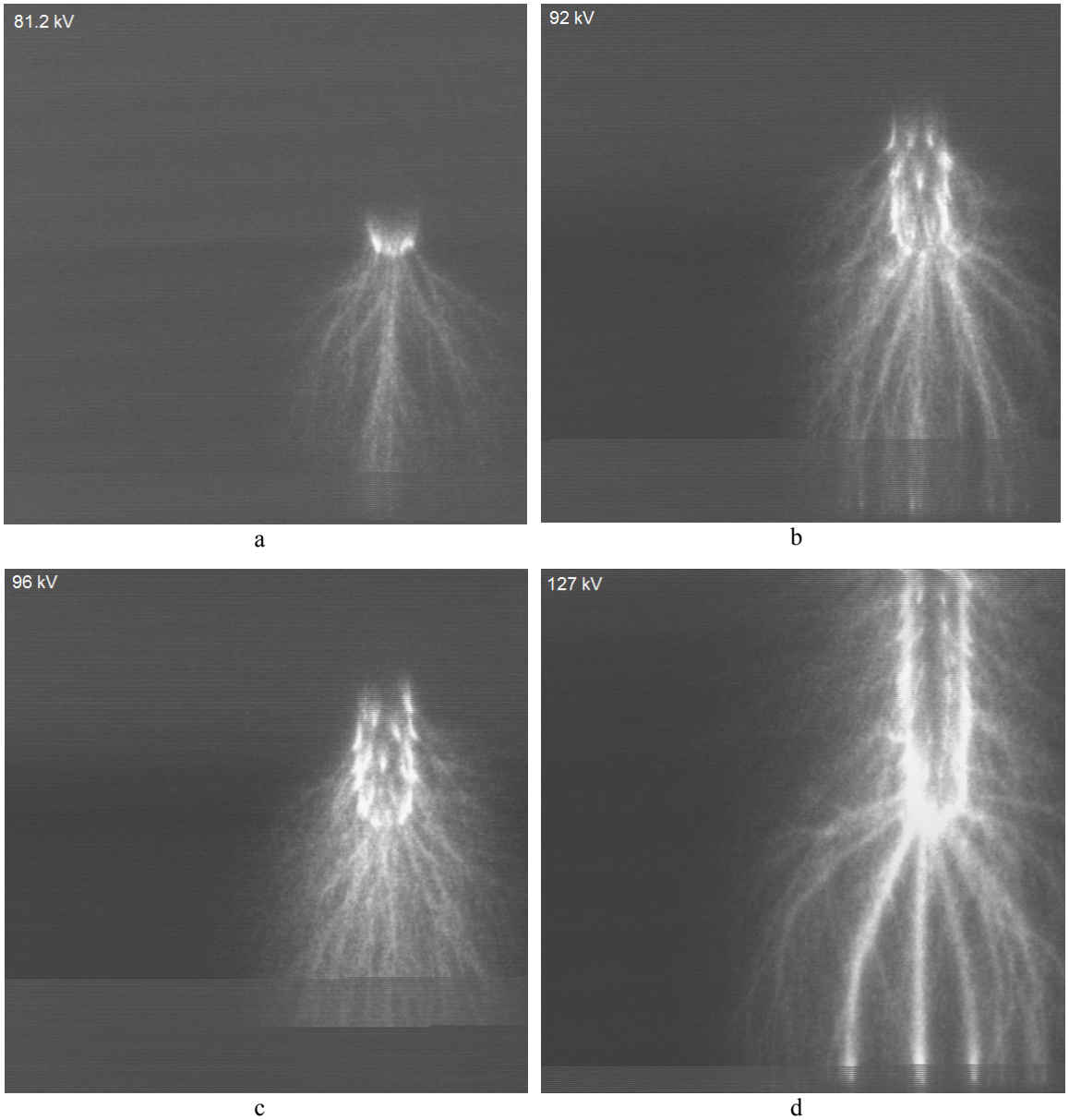

Fig. 4.11 – Discharge activity during positive lightning impulse application at fixed electrode distance. Electrode distance 89 mm. Applied voltages; [a)] 81.2 kV, [b)] 92 kV, [c)] 96 kV and [d)] 127 kV.

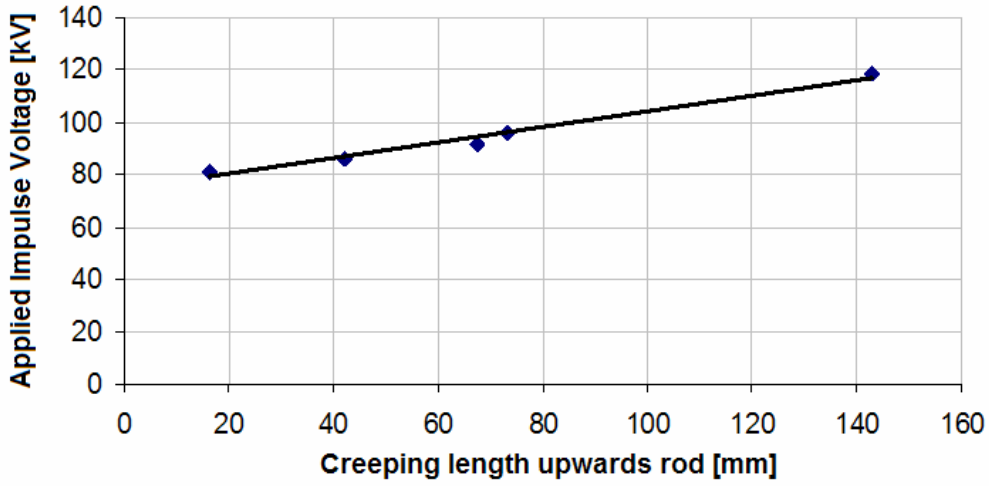

Fig. 4.12 – Creeping distance for discharge activity during application of positive lightning impulses. Electrode distance 89 mm. A further increase in applied impulse voltage results in breakdown.

The data presented in Fig. 4.12 show that the creeping length increases linearly with applied voltage. Looking at the Laplacian field distribution (background field) it shows that for creeping distances higher than about 10 mm from the tip, visible discharge activity occurs in regions where the background field (Laplacian field; without surface charges) exceeds 2.3 kV/mm. Further up, no visible discharge activities were observed.

Another example for a shorter electrode distance (34 mm) is shown in Fig. 4.13 and Fig. 4.14.

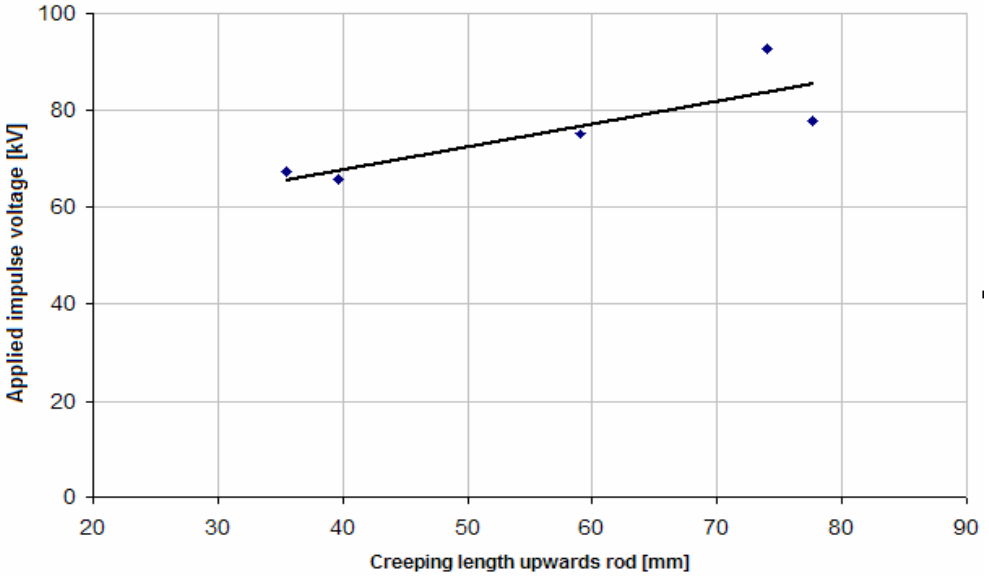

Fig. 4.13 – Creeping distance for discharge activity during application of positive lightning impulses. Electrode distance 34 mm. A further increase in applied impulse voltage is likely to result in the breakdown of the insulation system.

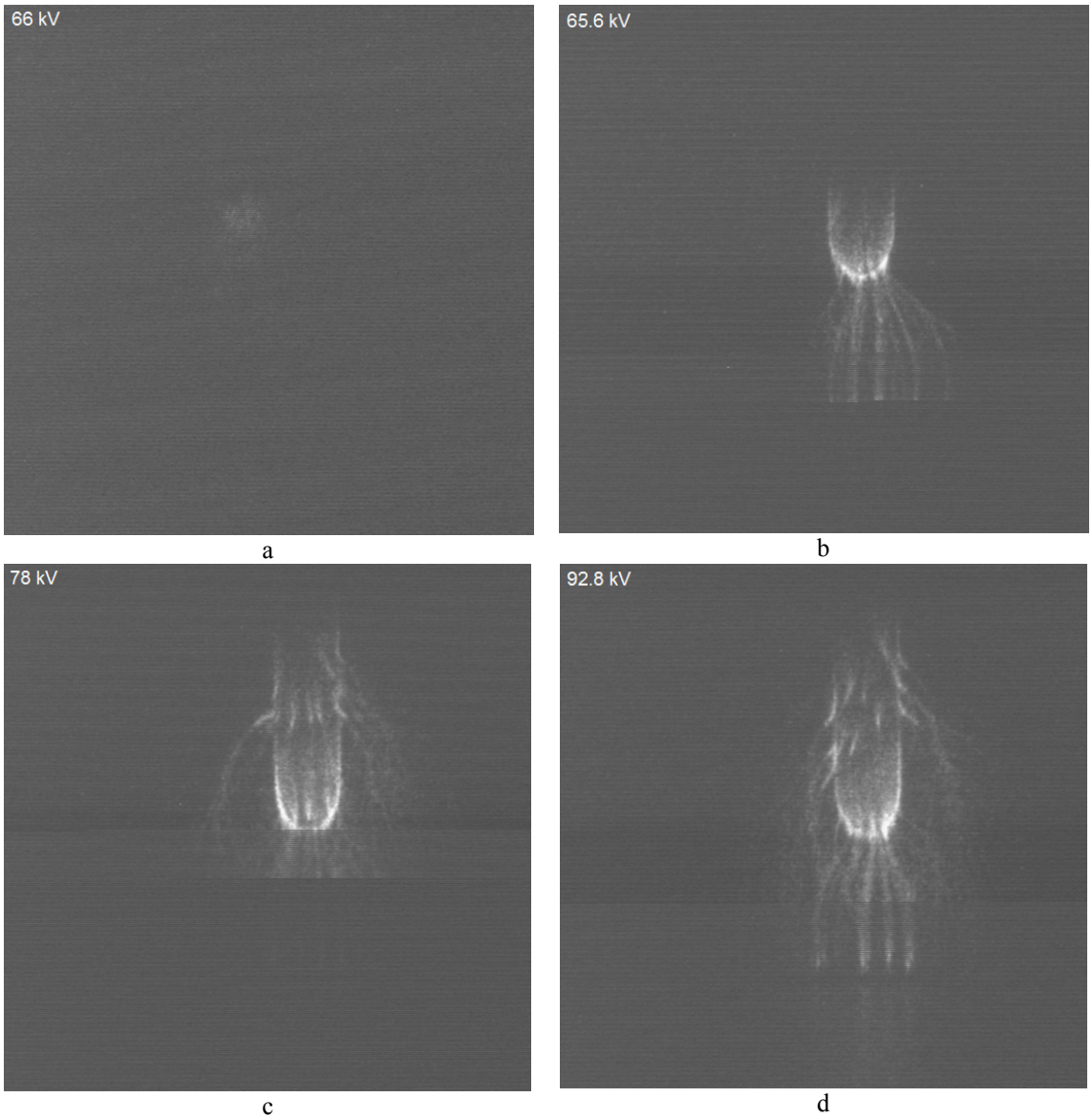

Fig. 4.14 – Discharge activity during positive lightning impulse application at fixed electrode distance. Electrode distances 34 mm. Applied voltages [a)] 66 kV, [b)] 65.6 kV, [c)] 78 kV and [d)] 92.8 kV.

As for a longer electrode distance, field calculations show that discharge activities spread upwards along the rod where the background field exceeds about 2.3 kV/mm. Further up, no visible discharge activities are observed.

For negative impulses it was very difficult to see how far up the discharges are spreading as the discharges became diffuse and less light was emitted compared to that from positive lightning impulses.

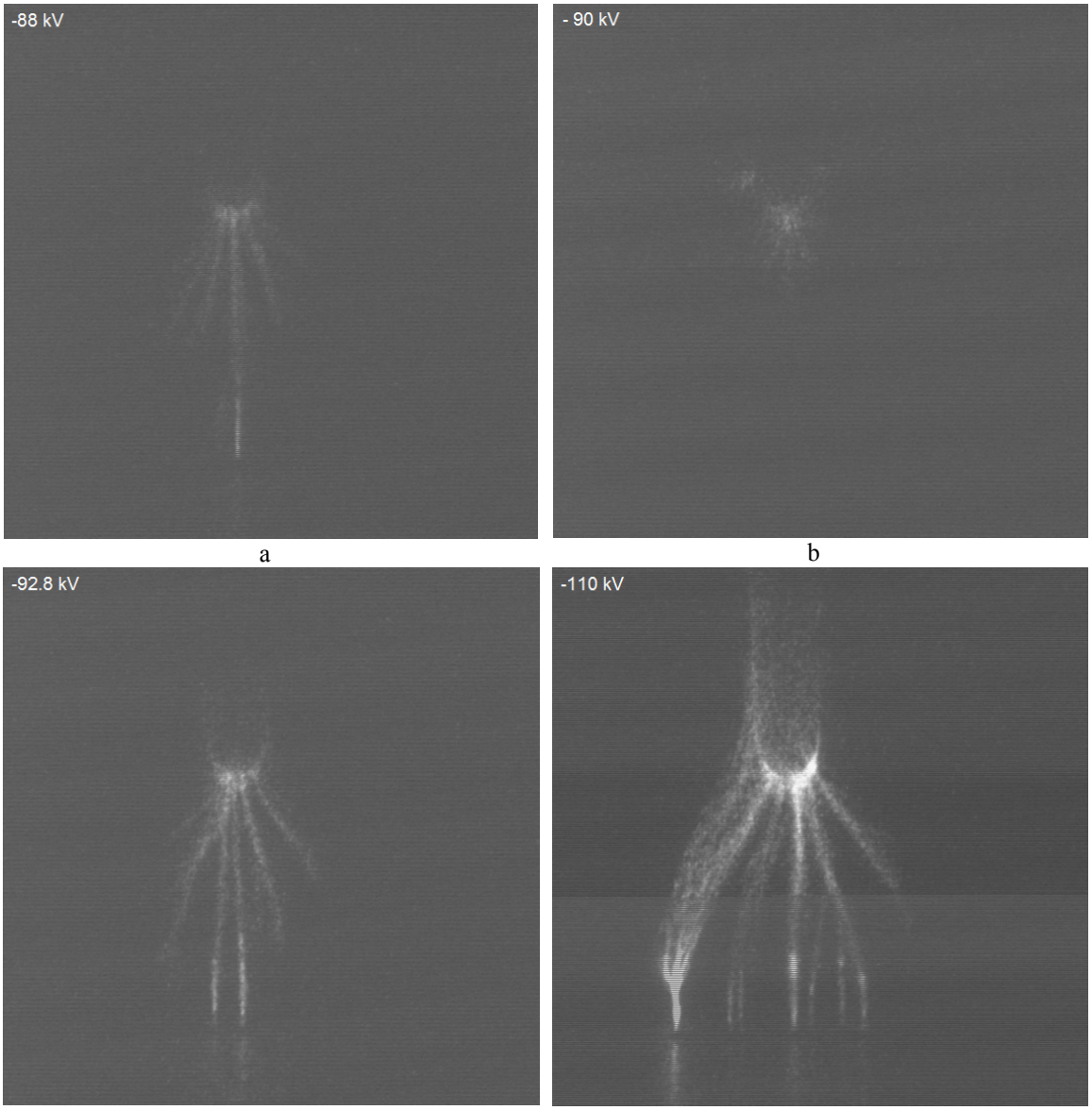

Fig. 4.15 – Discharge activity during negative lightning impulse voltage application at fixed electrode distance.. Electrode distances 63 mm. Applied voltages, [a)] -88 kV, [b)] -90 kV, [c)] -92.8 kV and [d)] -110 kV.

The creepage length of the discharge activities upwards along the rod for negative lightning impulses as function of applied impulse voltage is presented graphically in Fig. 4.16.

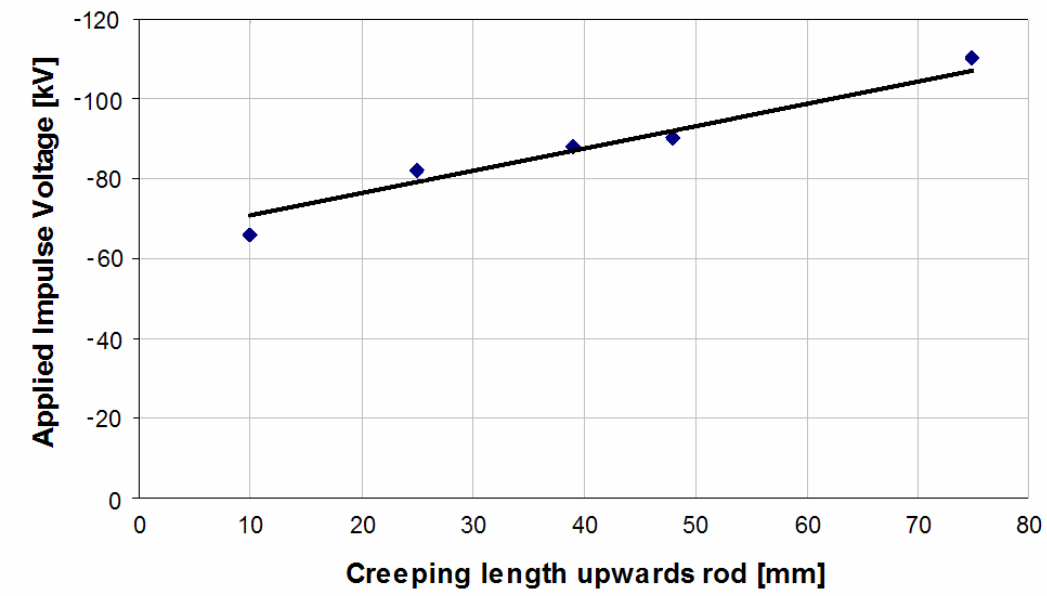

Fig. 4.16 – Creeping distance for discharge activity during application of negative lightning impulses. Electrode distance 63 mm. A further increase in applied impulse voltage is likely to result in the breakdown of the insulation system.

Using FEM software for calculation of background field shows that for creeping distances higher than 10 mm upwards from the tip, visible discharge activity occurs where the background field (pure capacitive electric field without charges) exceeds about 2.5 kV/mm. Further up, no visible discharge activities were observed.

4.1.5 Measurements of charge decay

Conductivity measurements

Conductivity measurements were performed as described in Section 3.1.3.
From the measured currents, the conductivities were calculated and resulting conductivities are shown in Fig. 4.17.

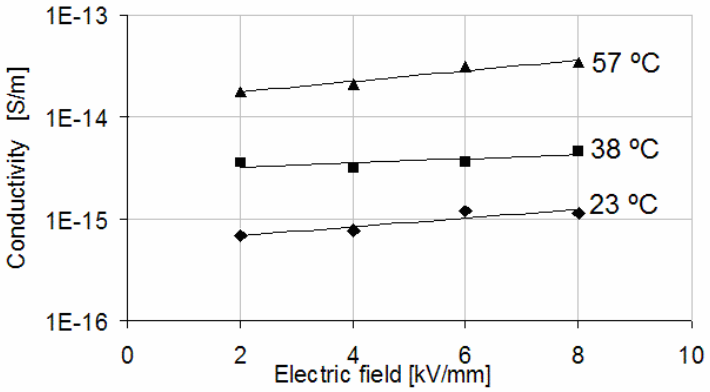

Fig. 4.17 - Results from measurements of dc conductivity of the silicone rubber on a rod sample, as a function of applied stress at temperatures between 23 and 57 ºC.

As expected the conductivity was found to increase with both electric field and temperature. Based upon these results the expected time constant τ was, according to Eq. (2.7), calculated to be 5.3 hours at room temperature (23 ºC) and electric field of 6 kV/mm.

Positive impulses

Results presented in Fig. 4.18 shows charge decay measurement after application of a positive lightning impulse of 137 kV at an electrode distance of 107 mm using the measurement set-up in Fig. 3.5.

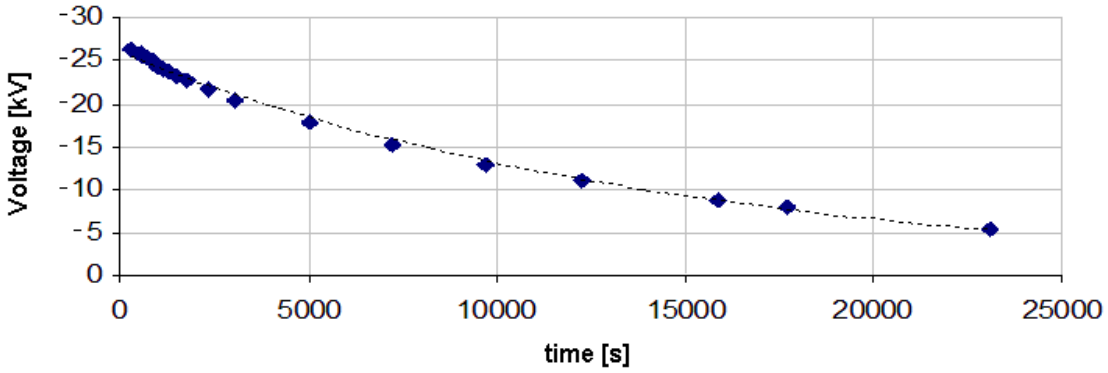

Fig. 4.18 - Surface potential decay after a positive impulse voltage. Applied voltage 137 kV and electrode distance 107 mm. Measured time constant τ is found to be about 4 hours.

The measured charge decay shown in Fig. 4.18 is found to be around 4 hours while the calculated time constant based on conductivity measurements is 5.3 hours. This strongly

indicates that the dominating relaxation process for the surface charges is ohmic conduction through the solid insulation.

Typical result of discharge activity and measured probe response after application of a positive lightning impulse is shown in the following three figures. For surface charge measurement, the set-up in Fig. 3.6 was used.

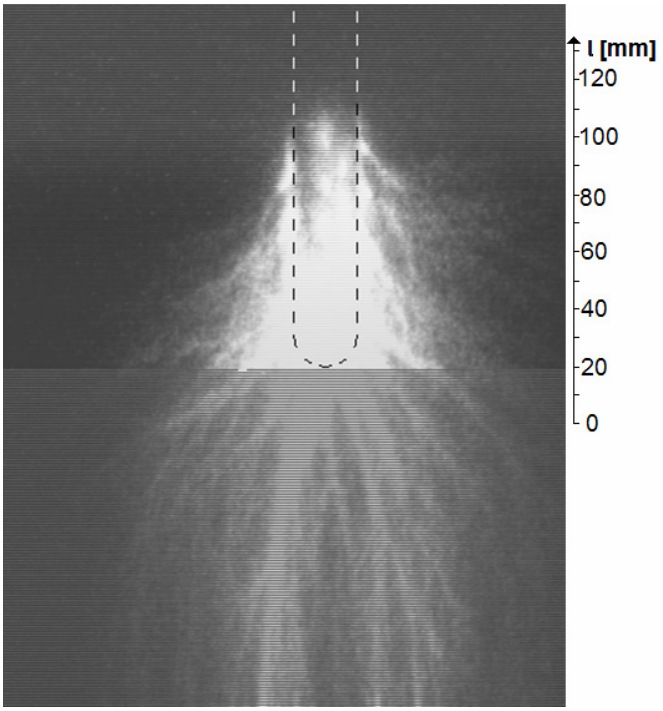

Fig. 4.19 - Video image of discharges with electrode distance 85 mm. Applied impulse voltage 98.6 kV (no electric breakdown of the insulation system. The stripes are due to art-effect of the camera.)

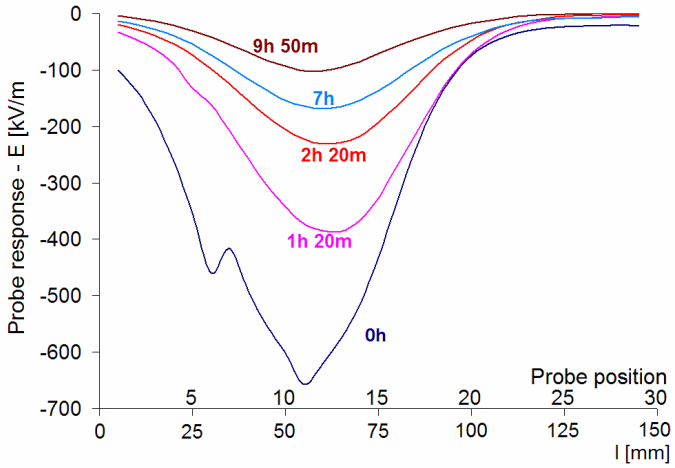

Fig. 4.20 - Measurement of electric field along the cylinder. Corresponding video image of discharge is shown in Fig. 4.19

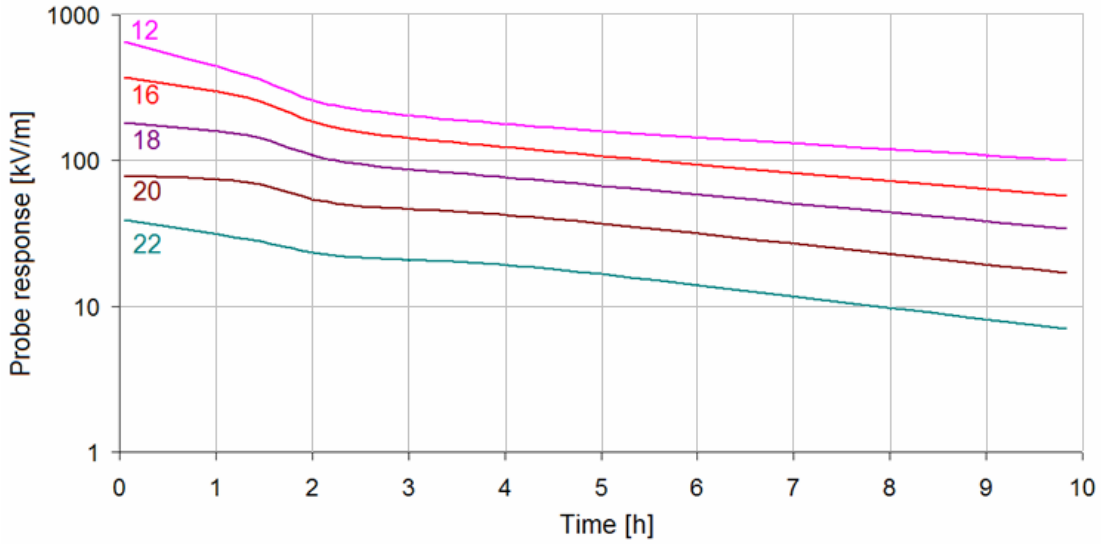

Fig. 4.21 - Charge decay of some probe positions of Fig. 4.20 (corresponding video image shown in Fig. 4.19.)

The image of the discharge activity presented in Fig. 4.19 shows that the discharges occur over a wide part of the air gap and bridge the gap entirely. This indicates that the solid insulation must be able to withstand the entire applied impulse voltage stress.

The correlation between the image of the accumulated discharge activities in Fig. 4.19 and the measured probe response of Fig. 4.20 is good. The highest electric field is measured around the areas with the highest discharge activity. As presented earlier in this chapter, the measured charge decay has a time constant τ of around 4 hours. Results presented in Fig. 4.20 and Fig. 4.21 shows that the decay at some of the positions is initially faster than the expected 4 hours, indicating that areas with relative high charge density compared to the surrounding areas tend to smooth out after some time.

Negative impulses

Fig. 4.22 shows a typical image of accumulated discharge activities in an air gap during the application of negative impulse voltages. The corresponding measured probe response is shown in Fig. 4.23.

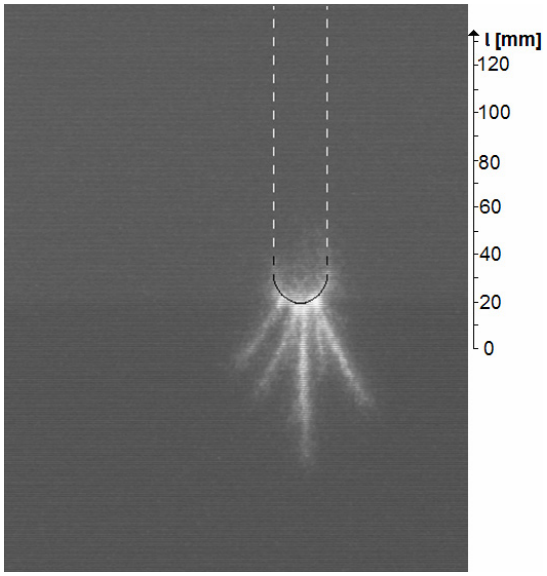

Fig. 4.22 - Video image of discharge activity during application of a negative impulse voltage(-90 kV) No electrical breakdown occurred in the insulation system.

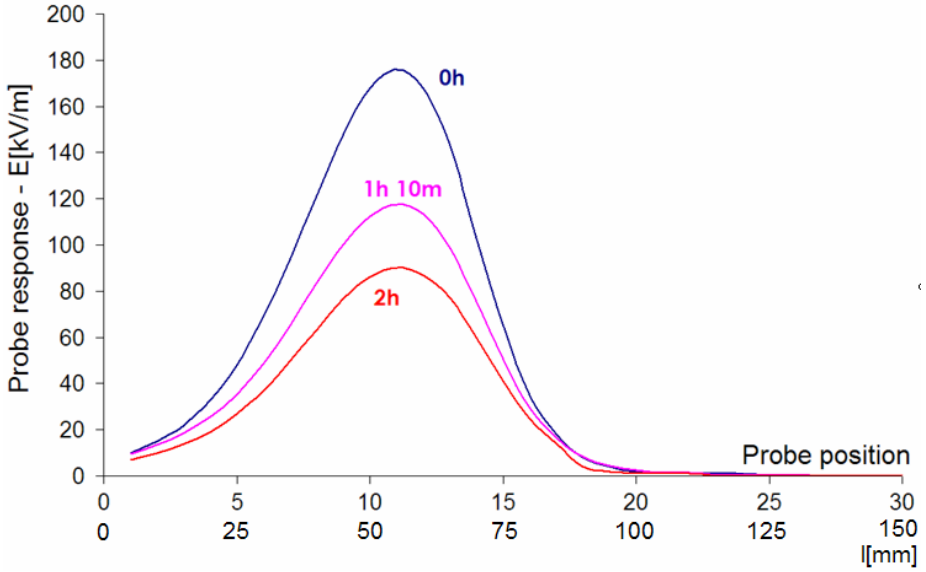

Fig. 4.23 - Measurement of electric field along the cylinder as function of time after a negative impulse. Corresponding video image of discharges is shown in Fig. 4.22

From Fig. 4.22 it can be seen that the discharge activity is concentrated around the tip of the rod where the electric field is highest. A few streamers around the tip are found pointing towards the earth electrode. Further upward the illumination is rather diffuse and decreases gradually upwards along the rod. The streamers do not bridge the air gap as is the case for positive streamers.

At higher impulse voltages, a different surface charge distribution pattern was observed as surface charges of both polarities are found. The number of streamers around the tip also increased.

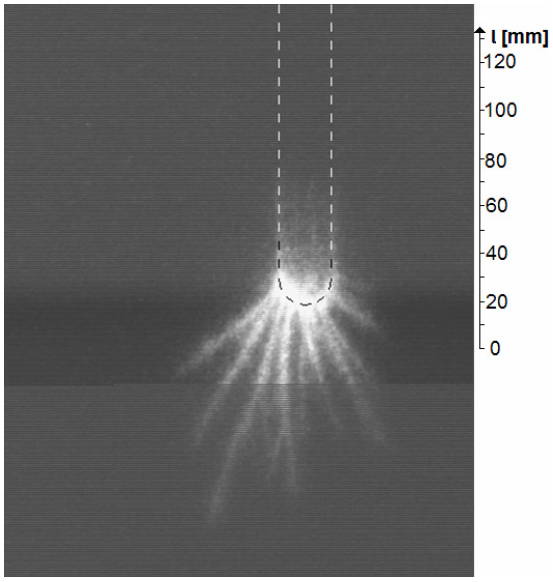

Fig. 4.24 - Video image of discharges. Applied impulse voltage was -102 kV and electrode distance 63 mm (no electrical breakdown of the insulation system)

After being stressed with a negative impulse, positive charge is expected to be found along the rod surface. However, when the discharges were relatively strong, positive surface charges were found at the tip and lower part of the rod. Further up the accumulated charge changed polarity from positive to negative. An example of this is shown in Fig. 4.25.

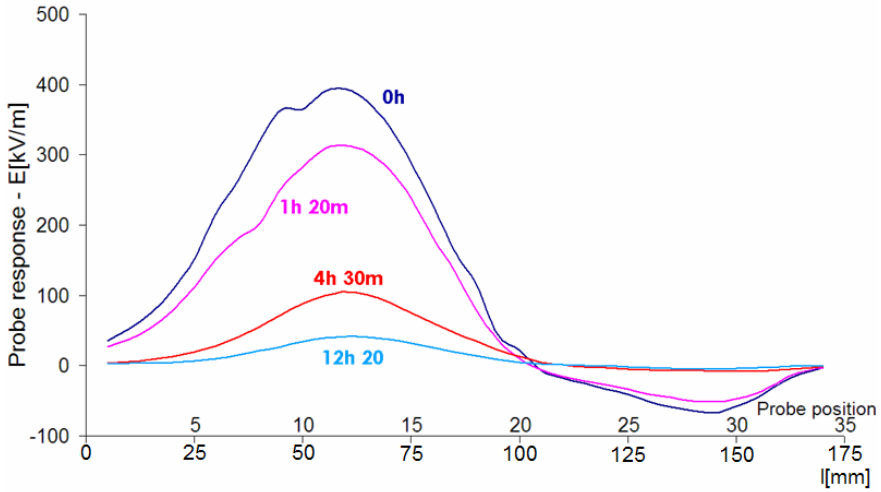

Fig. 4.25 - Measurement of electric field along the cylinder after application of a negative impulse voltage. Positive field is expected along the whole rod, but on the upper part of the rod, a change in the polarity of the accumulated charge was observed. Corresponding video image of discharge activity is shown in Fig. 4.24.

The negative surface charge has been observed only when the applied negative impulse is 10-20% higher that the lowest impulse voltages giving visible discharge activity in the air gap.

4.2 Influence of conductivity

Remaining surface charges after discharge activities are in certain situations undesirable, e.g. when a lightning impulse voltage is followed by a second one of opposite polarity before the surface charges have been reduced to (near) zero, as it might result in a breakdown of the insulation system as the electric field of the air gap is enhanced by the remaining surface charges.

Conductivity measurement of the iodine doped SIR showed that a conductivity of $6.6 \cdot 10^{-9}$ S/m was achieved. With a relative permittivity ε_r of 3.1 this gives, according to Eq. (2.7) an estimated time constant τ of 42ms.

Due to the very small time constant of the iodine doped SIR, no remaining charges were found 30 seconds after impulse application.

A comparison of the calculated and measured time constants is given in Table 4.1.

Table 4.1 – Calculated time constants based on conductivity measurement and measured time constants for the different test objects.

Insulation material	$\tau_{calculated}$	$\tau_{measured}$
SIR	5.3 h	4.6 h
PA66	1.7 h	1.36 h
SIR doped with iodine	42 ms	< 30 sec.

Typical images of discharge activities in the air gap during application of positive and negative impulse voltage are shown in Fig. 4.26 with an electrode distance of 86 mm and different applied voltages.

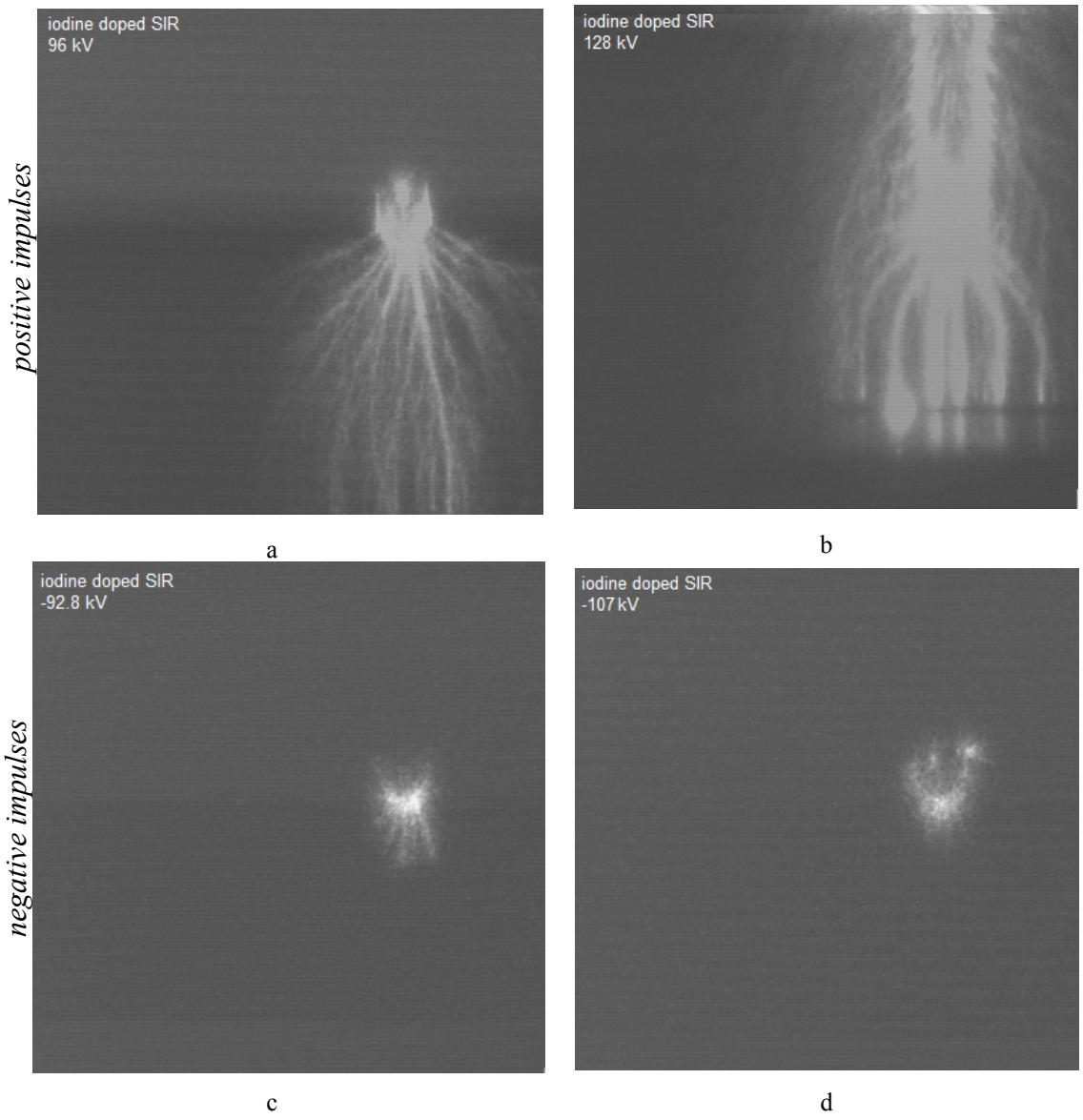

Fig. 4.26 – Discharge activity during application of a positive (a and b) and negative (c and d) lightning impulse voltage for an iodine doped SIR covered rod. Electrode distance 86 mm in all cases. Voltage applied: [a)] 96 kV, [b)] 128kV, [c)] -92.8 kV and [d)] -107 kV. No electric breakdown of the insulation system in any of the cases.

The results presented in Fig. 4.26 show that the discharge patters for an iodine doped SIR covered rod were similar to that of a pure SIR covered rod.

The discharge inception voltage was also measured as function of electrode distance for SIR with and without iodine doping. The results are shown graphically in Fig. 4.27.

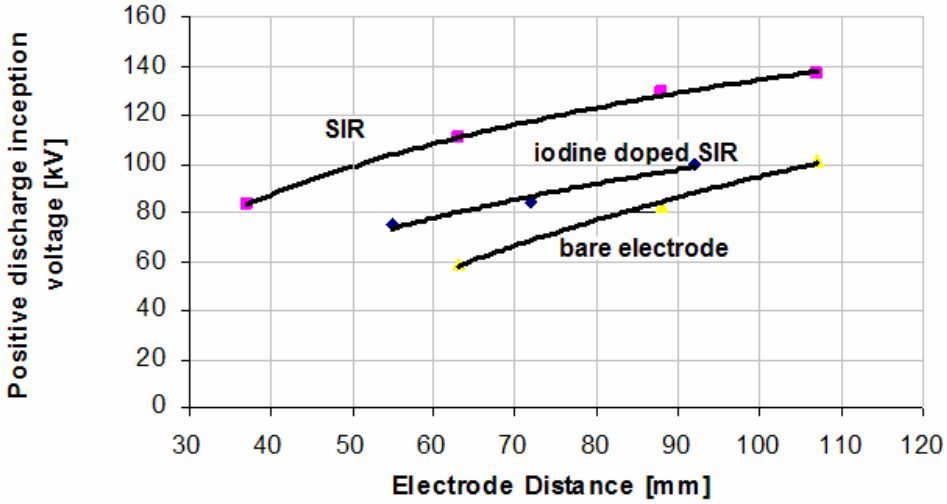

Fig. 4.27 – Positive discharge inception voltage as function of electrode distance for SIR, iodine doped SIR and bare electrodes.

The inception voltage of a rod covered with iodine doped SIR is lower than the one covered with pure SIR, but still higher than the uncovered rod. The results show that even with a very high conductivity, the principle of hybrid insulation works well.

Polyamide (PA66)

Discharge activity during positive lightning impulses on a PA66 covered rod is presented in Fig. 4.28.

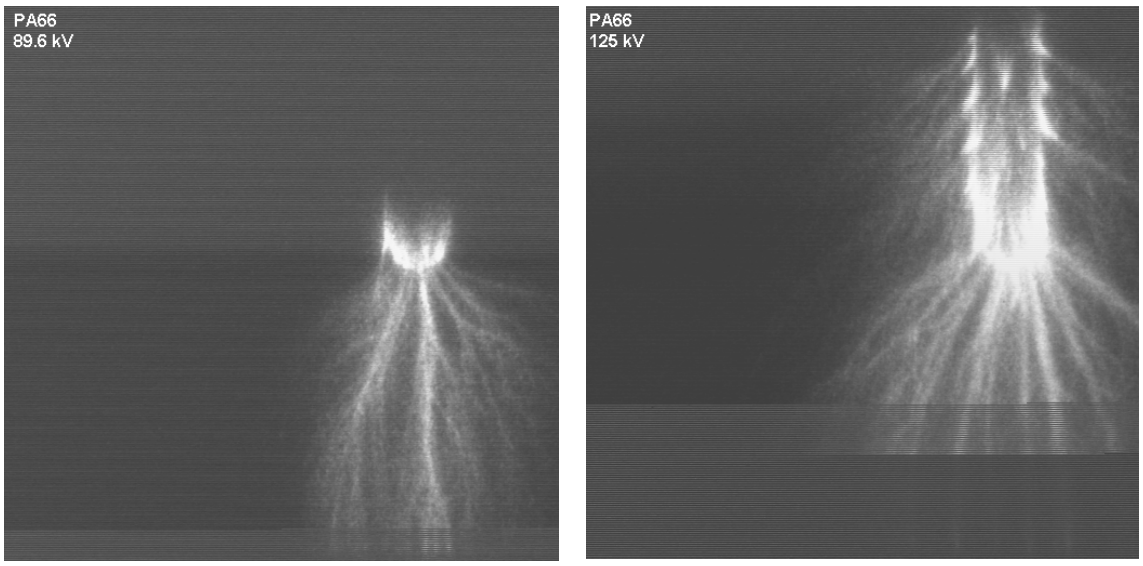

a b

Fig. 4.28 - Discharge activity during application of a positive lightning impulse voltage for a PA66 covered rod. Electrode distance 103 mm in all cases. Voltage applied: [a)] 89.6 kV and [b)] 125 kV.

The results show that the discharge patterns are similar to that of SIR covered rods.

Silicone rubber with conductive layer

In Fig. 4.29 and Fig. 4.30 typical video images of air gap discharge activity and corresponding voltage and current trace are shown respectively. In this case, the discharge inception voltage was reduced from 137 kV without conductive layer to 75 kV with. Visible discharge activity was limited to a discharge channel with a foot point at the tip of the rod and one to the edge of the conductive paint. The maximum resulting current was in this case reduced to 1 mA.

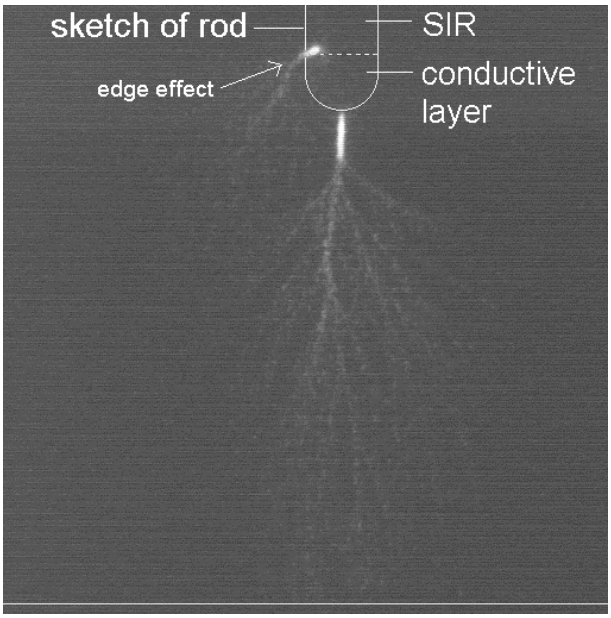

Fig. 4.29 – Image of discharges with a conductive layer on the tip the rod during application of a positive lightning impulse. Corresponding current and voltage graphs are shown in Fig. 4.30. Applied voltage 75kV and electrode distance 107 mm (no electric breakdown occurred in the insulation system.)

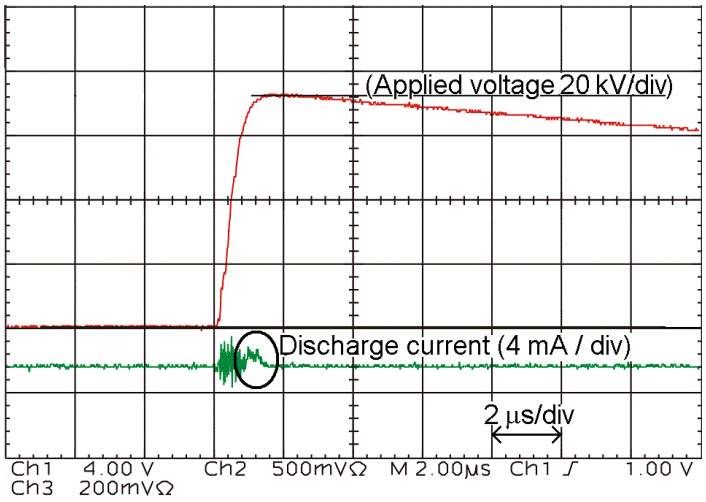

Fig. 4.30 - Measured current and voltage. Discharges are observed close to the peak voltage. The oscillations in the first microsecond of the discharge current are due to ignition of the spark gaps of the Marx impulse generator.

5 ESTIMATION OF SURFACE CHARGE DENSITY

In order to solve the inverse problem of finding the surface charge density based on measurement of the electric field at a distance, three different mathematical approaches are studied. The first using Truncated Singular Value Decomposition (TSVD) as regularization of the Pedersen's Λ-method and the two others use regularization in combination with boundary element method (BEM) and finite element method (FEM) respectively.

5.1 Regularization - Truncated Singular Value Decomposition

When applying the λ-method of Pedersen [1] to a probe response, a Λ-matrix that is close to singular (ill-conditioned) is obtained. Since Λ is ill-conditioned, the solution of Eq. (2.23) is very sensitive to perturbations in the measured probe response p. Small perturbations in p may lead to large perturbations in the surface charge distribution x, creating a so-called ill-posed problem.

A method for dealing with such ill-conditioned matrices is the Truncated Singular Value Decomposition. The basic idea of TSVD, as well for other regularization methods is to define a new well-posed problem related to the ill-posed problem, with a solution that is less sensitive to disturbances [41].

Considering the ill-posed problem with an ill-conditioned matrix A:

$$Ax = b \tag{5.1}$$

A solution of x is sought according to

$$E = \min \left\| Ax - b \right\|_2 , \; A \in \mathbb{R}^{n \times n} \tag{5.2}$$

where $\|.\|_2$ is the Euclidean norm.

In order to solve ill-posed problems, mathematical approaches like the Truncated Singular Value Decomposition [42, 43] can beneficially be used. By the use of Singular Value Decomposition (SVD, see Appendix A) and TSVD, linear dependencies can be identified to improve the system description and lead to a modified system with a better conditioned matrix. The new system can then be solved using standard numerical methods.

The basic idea is to impose the additional requirements on the solution that its norm should be small and thus hopefully damp the contributions of the errors of the right-hand side.

The n×n matrix A is approximated with a matrix A_k of a lower rank k and ignoring the components on the right-hand side corresponding to the ignored components of A.
The matrix A_k used in the TSVD is defined as the rank-k matrix:

$$A_k = U\Sigma_k V^T \tag{5.3}$$

where $\Sigma_k = diag(\sigma_1,...,\sigma_k,0,...,0) \in \mathbb{R}^{m\times n}$ and k < rank(A) with the smallest n-k singular values replaced by zeros.

$\sigma_1 \geq \sigma_2 \geq \ldots \geq \sigma_k \geq 0$ are called the singular values of A. U = ($\mathbf{u}_1$, $\mathbf{u}_2$, … ,$\mathbf{u}_n$) and V = ($\mathbf{v}_1$, $\mathbf{v}_2$, … ,$\mathbf{v}_n$) are matrices with orthonormal columns where the vectors $\mathbf{v}_i$ and $\mathbf{u}_i$ are the left and right singular vectors of A respectively.

The solution of TSVD of Eq. (5.2) is given by:

$$x_k \equiv A_k^+ b \tag{5.4}$$

and is less sensitive to errors in b and A. A_k^+ is the pseudo-inverse of A_k:

$$A_k^+ = V\Sigma_k^+ U^T \tag{5.5}$$

where $\Sigma_k^+ = diag(\sigma_1^{-1},...,\sigma_k^{-1},0,...,0) \in \mathbb{R}^{m\times n}$

Perturbations
Due to approximations, rounding errors and other measurement errors, it is unlikely that true zero singular values occur in practical numerical applications. It is therefore common to neglect singular values smaller than a certain threshold, which corresponds to the use of TSVD [41]. Considering a perturbed matrix Ã:

$$\tilde{A} = A + E = \tilde{U}\tilde{\Sigma}\tilde{V}^T \tag{5.6}$$

The choice of a suitable threshold takes its basis in the following perturbation bound for the singular values [41]:

$$\left|\sigma_i - \tilde{\sigma}_i\right| \leq E, \quad i = 1,2,...,n \tag{5.7}$$

That implies that singular values $\tilde{\sigma}_i$ of Ã larger than E are guaranteed to represent nonzero singular values σ_i of A. The singular values $\tilde{\sigma}_i$ below E cannot be distinguished from exact zeros. When

$$\tilde{\sigma}_k > E \geq \tilde{\sigma}_{k+1} \tag{5.8}$$

for some k, one can only guarantee that the rank of A is at last k. The numerical rank r_θ of A is the number of singular values strictly greater than θ:

$$\sigma_1 \geq \ldots \geq \sigma_{r_\theta} \geq \theta \geq \sigma_{r_\theta+1} \tag{5.9}$$

TSVD consists only of the contributions $u_i\sigma_i v_i^T$ to A with a significant magnitude $\|u_i\sigma_i v_i^T\|_2 = \sigma_i$ as measured by the error level θ while uncertain contributions are discarded [41].

The numerical rank is independent of the particular distribution of singular values of A and is only useful when r_θ is well-determined with respect to the error level θ. This is only the case if there is a well-defined gap between the singular values σ_{r_θ} and $\sigma_{r_\theta+1}$ [41-43].

In case of an ill-determined numerical rank, there is no well-defined gap between the singular values, thus this method cannot be used.

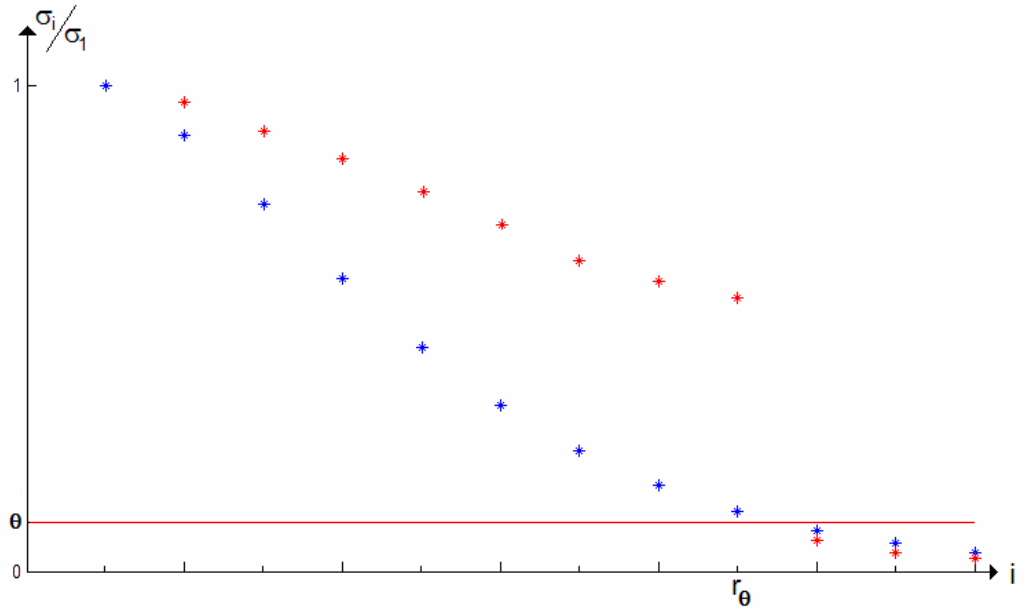

Fig. 5.1 – Example on singular value spectra of ill-conditioned matrixes in case of a well-determined (red) and ill-determined (blue) numerical rank.

For ill-determined numerical ranks, there is no intuitive way on choosing numerical rank, but nevertheless, TSVD might still give good results [41].

5.2 Surface charge calculations

5.2.1 Regularization - Truncated SVD

Pedersen's λ-method [1, 34] has its practical limitations as described in Section 2.5. The method has previously proved to be very sensitive to small measurement inaccuracies [35]. Small variations in the measured probe response, *p*, may then cause large fluctuations in the calculated charge distribution.
However, it is possible to reduce the influence of the measurement inaccuracies utilizing regularization. In this chapter Truncated Singular Value Decomposition is used to obtain an approximate solution based on Pedersen's λ-method.

Example 1

Starting with an ideal case, without any noise or disturbances, assuming a homogeneous surface charge density of $1 \cdot 10^{-4}$ C/m^2 on the tip and first 10 mm upwards the rod, decreasing to zero along the next 55 mm following $(0.5+0.5 \cdot \cos(s)) \cdot 10^{-4}$ C/m^2, where s is $\in [0,\pi]$. The surface charge distribution is shown graphically in Fig. 5.5. The aluminium rod is earthed (U = 0V).
A figure of the electric potential distribution of this case is given in Fig. 5.2.

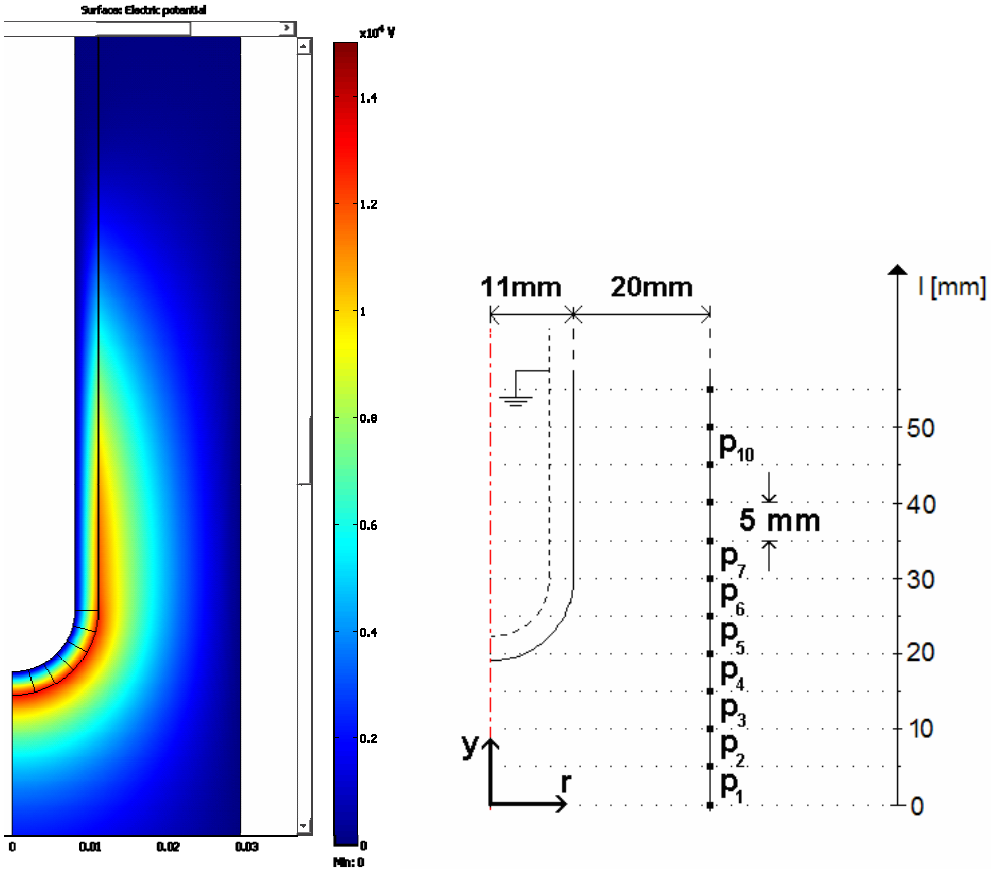

Fig. 5.2 – Electric potential distribution. The layout is rotationally symmetric around x = 0.

The Λ-matrix is calculated as described in Section 2.5 with the geometry of Fig. 5.2 discretized as shown in Fig. 5.3.

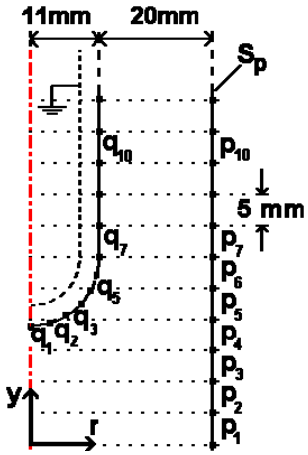

Fig. 5.3 - Division of insulating surface and measurement points into segments. The layout is rotational symmetric around the y-axis. Each measurement segment is 5 mm high.

The applied surface charge distribution gives a simulated probe response as shown in Fig. 5.4.

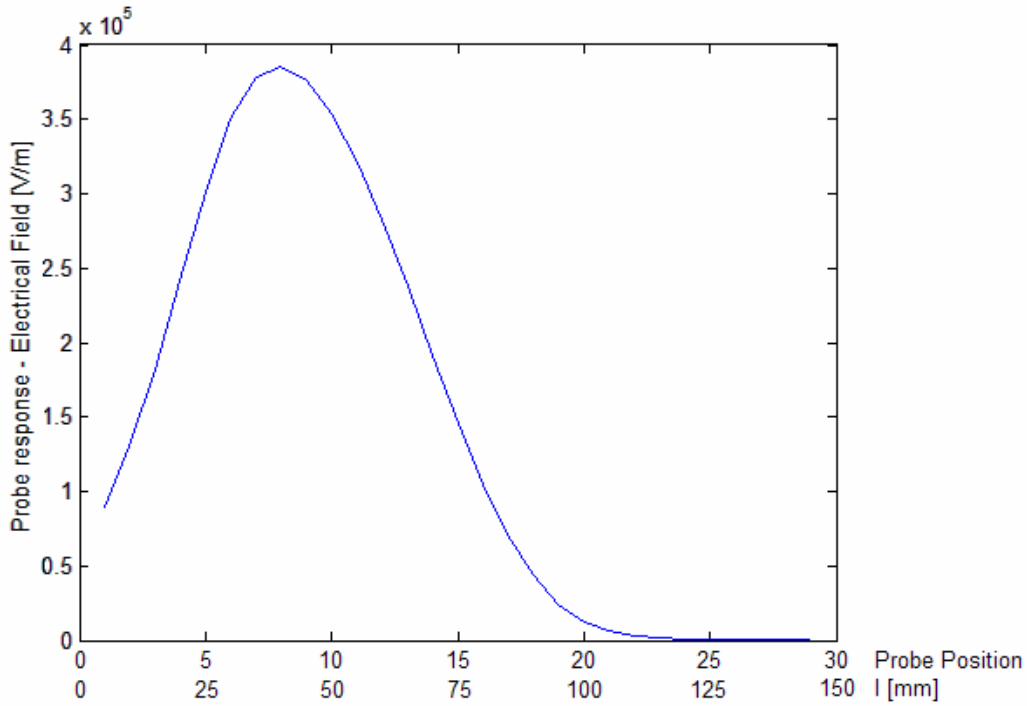

Fig. 5.4 – Simulated probe response.

Based on the simulated probe response, Eq. (2.23) can be used to calculate the surface charge density σ.

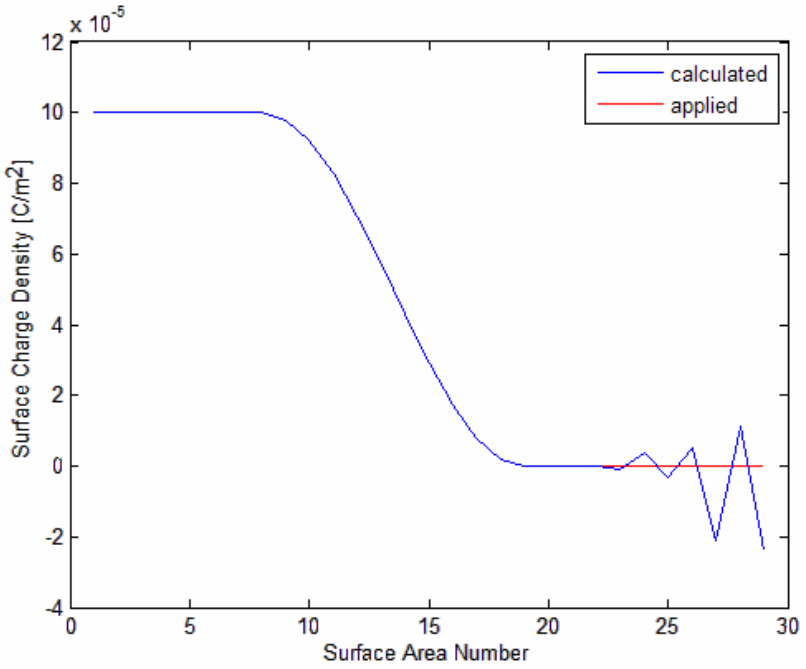

Fig. 5.5 – Calculated surface charge density (blue) and applied surface charge density (red) for an ideal case.

As seen in Fig. 5.5, calculated and applied surface charge density follow each other well. However, as seen at the last probe positions, there are some oscillations at the far end. This is caused by the matrix Λ being ill-conditioned, as described earlier. Since the case considered here is ideal; no noise or disturbances are present. However, when adding as little as 1% white noise to the simulated probe response, shown in Fig. 5.6, the perturbations on the probe response cause large fluctuations in the calculated surface charge density distribution.

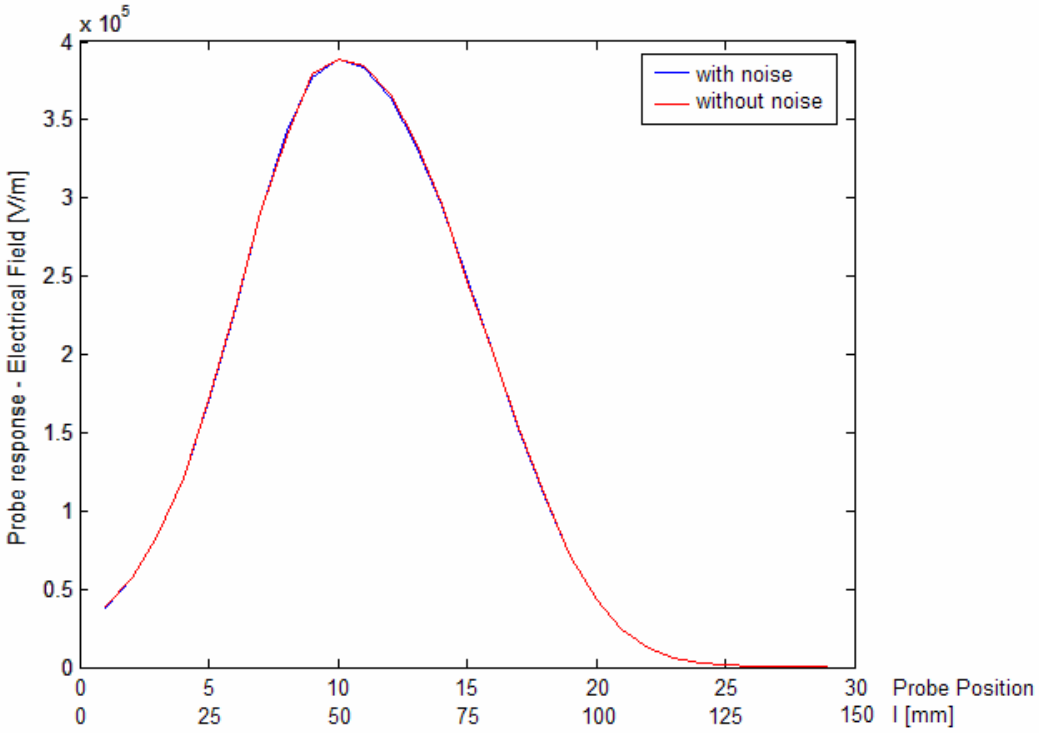

Fig. 5.6 – Simulated probe response without (blue) and with (red) 1% white noise.

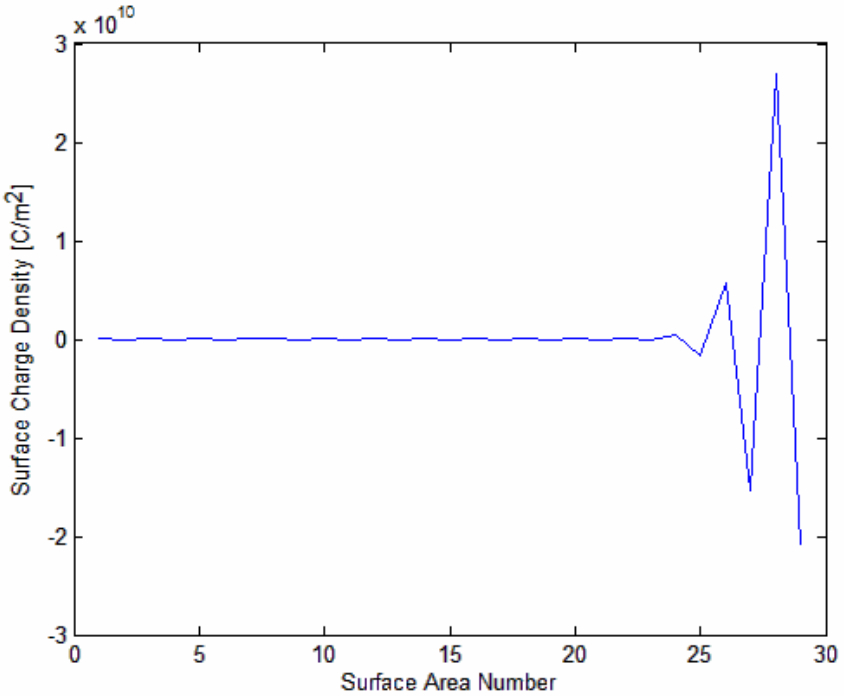

Fig. 5.7 - Calculated surface charge density with 1% white noise on the probe response. The applied surface charge density is shown in Fig. 5.5. Since the oscillations are so large here, the original surface charge density would appear as a straight line around zero.

As seen in Fig. 5.7, the calculations of the surface charge density with as little as one per cent white noise added to the probe response causes the calculation of the surface charge to become highly unstable. Compared to the example without any noise present,

it is obvious that calculation of surface charge with the λ-method for large surface charge densities in its current form is impossible to use for a practical case.

By using the Truncated Singular Value Decomposition an approximate solution can be computed. The Λ-matrix is then replaced by a new matrix Λ_t that is an approximate matrix close to Λ (see Section 5.1).

This makes the TSVD no longer an exact composition of the original matrix Λ. But the approximate matrix Λ_k is in a very useful sense the closest approximation to Λ that can be achieved by a matrix of rank k [41].

In the following examples, the Λ-matrix used is a 30x30 matrix. A plot of the singular value spectra of the Σ-matrix is a useful tool in order to choose an appropriate numerical rank for the TSVD.

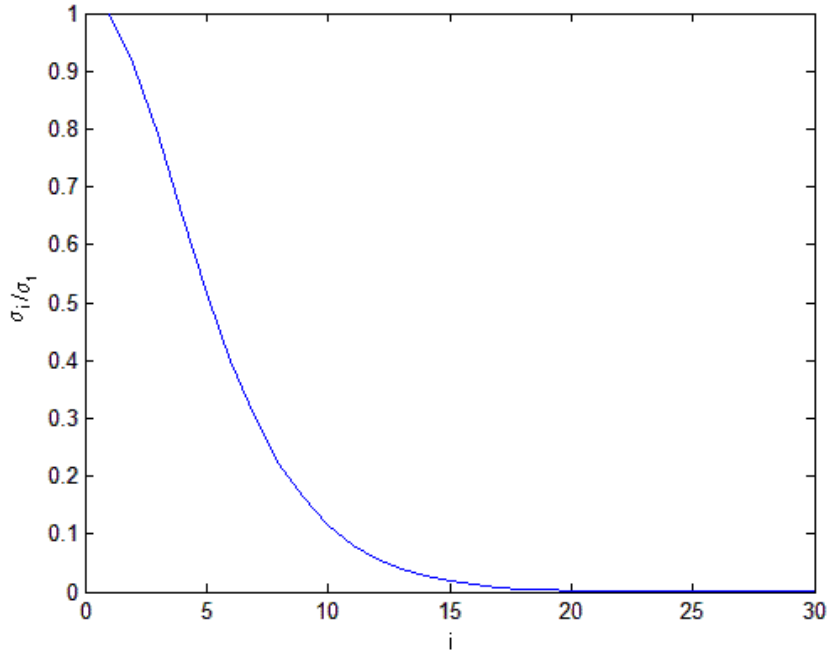

Fig. 5.8 – Singular value spectra for the 30x30 Λ-matrix.

As discussed in Section 5.1, a jump in the spectra would be expected at the index of optimal numerical rank. In Fig. 5.8 a jump in the singular value spectra is difficult to point out, but using logarithmic scale on the singular value spectra, a numerical rank can be found.

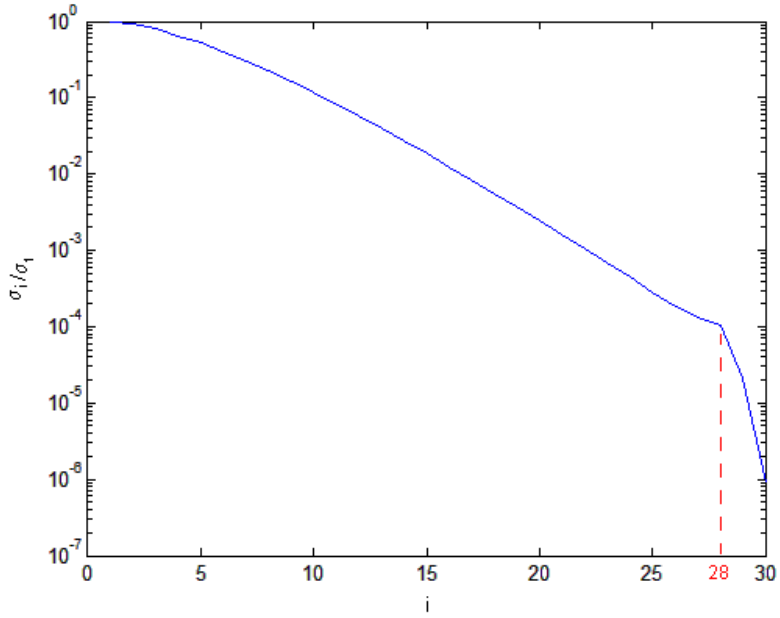

Fig. 5.9 – Logarithmic plot of the singular values for the 30x30 Λ-matrix.

From Fig. 5.9 a knee in the singular value plot can be seen at k = 28. This value is used as the numerical rank here when solving the inverse problem with TSVD.

Using TSVD on the noise-added probe response in Fig. 5.6 with the numerical rank found in Fig. 5.9, the surface charge density can be calculated:

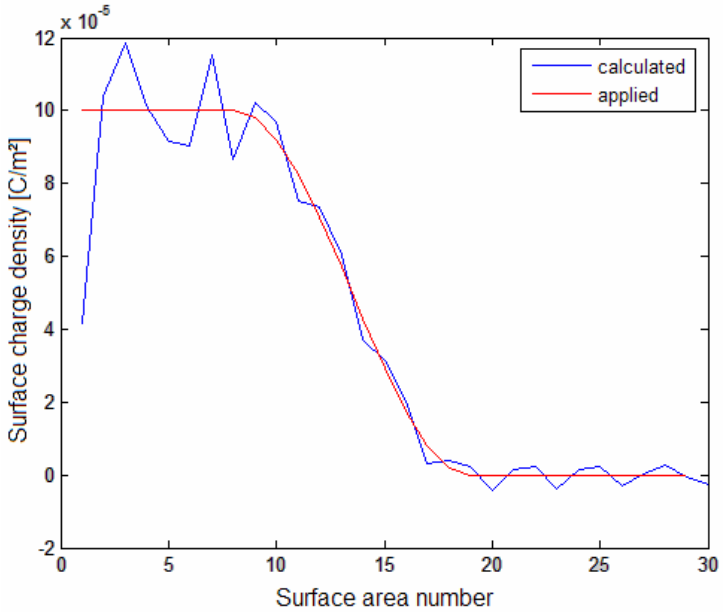

Fig. 5.10 - Surface charge density estimation with 1% white noise using TSVD (blue) compared with the applied surface charge (red).

As seen in Fig. 5.10 the calculated surface charge distribution oscillates around the true solution. To smooth out the fluctuations, the moving average is applied to the calculated surface charge density:

$$\hat{x}_i = \frac{1}{5}\sum_{m=-2}^{2} x_{|i+m|} \tag{5.10}$$

As the system is rotationally symmetric, $x_{-1} = x_1$ and $x_{-2} = x_2$ are assumed.

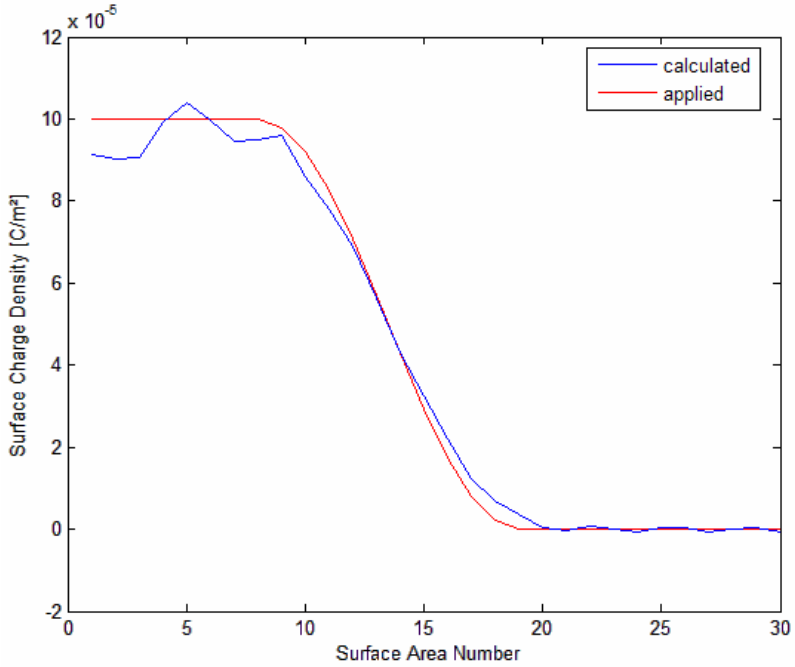

Fig. 5.11 – Surface charge density estimation with 1% white noise using TSVD (blue) and moving average compared with the applied surface charge (red).

Comparing Fig. 5.7 and Fig. 5.11 it is clear that the TSVD with moving average is improving the results of the Λ-method considerably when noise in the probe response is present. The solution found with TSVD is relatively close to the applied surface charge density.

In a practical measurement situation, the noise level and rounding errors are higher than 1%. Increasing the level of white noise from 1% to 10% in the probe response gives a resulting probe response as shown in Fig. 5.12.

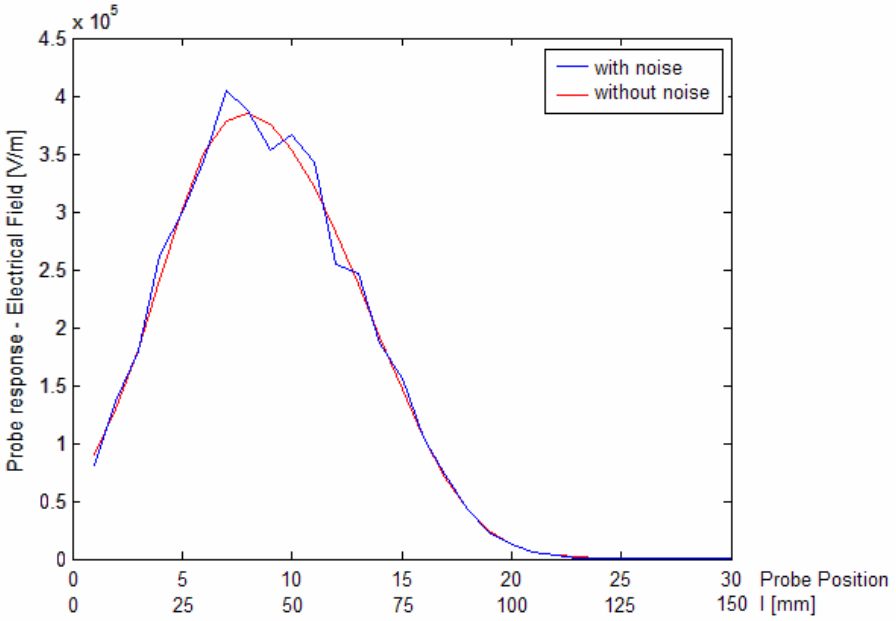

Fig. 5.12 - Simulated probe response without noise (red) and with 10% white noise (blue).

Based on the probe response with noise, using TSVD, the resulting surface charge density estimation in Fig. 5.13 is achieved.

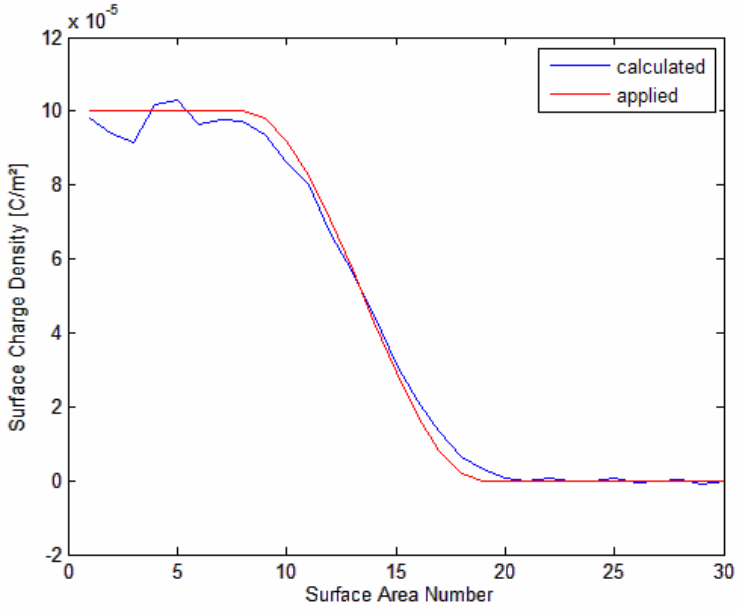

Fig. 5.13 - Surface charge estimation with 10% white noise using TSVD on the λ-method (blue) compared with the applied surface charge (red) based on the probe response shown in Fig. 5.12.

As seen in Fig. 5.13, even with as much as 10% white noise added to the probe signal, it is possible to calculate the surface charge density relatively correctly. For both cases with 1% and 10% noise respectively, there is a deviation between the "true" and calculated surface charge density. The deviation is dependent upon how truncated the approximate matrix Λ_t is and how rapid the surface charge density changes along the rod.

Example 2

In the following example, a surface charge density jump from $1 \cdot 10^{-4}$ C/m² to 0 C/m² is applied to the insulating surface. To the probe response, 1% and 10% white noise is added. The calculated surface charge distribution for the different noise levels is shown in Fig. 5.15 and Fig. 5.16 respectively.

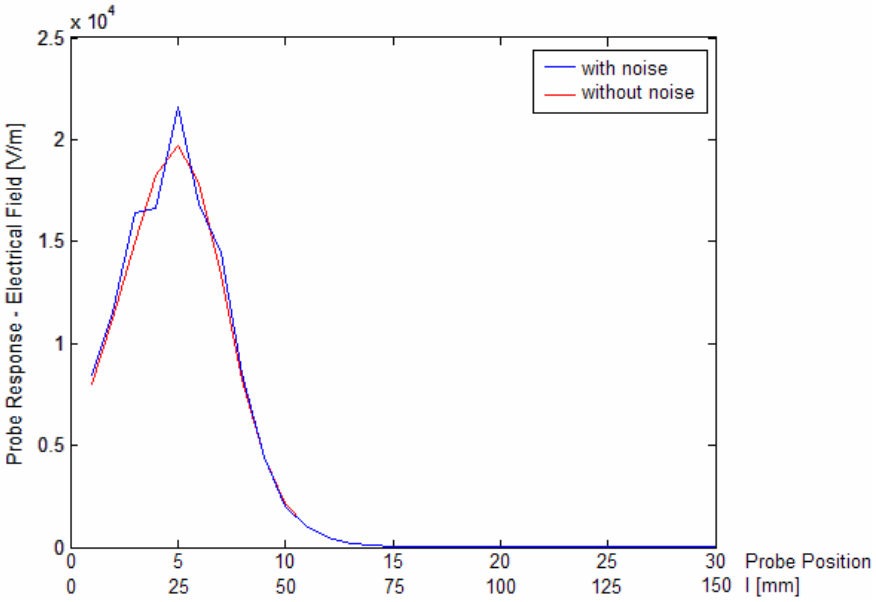

Fig. 5.14 – Probe response with (blue) and without (red) 10% white noise.

Calculating the surface charge density using TSVD, the following results are obtained with 1% and 10% noise added to the probe response respectively.

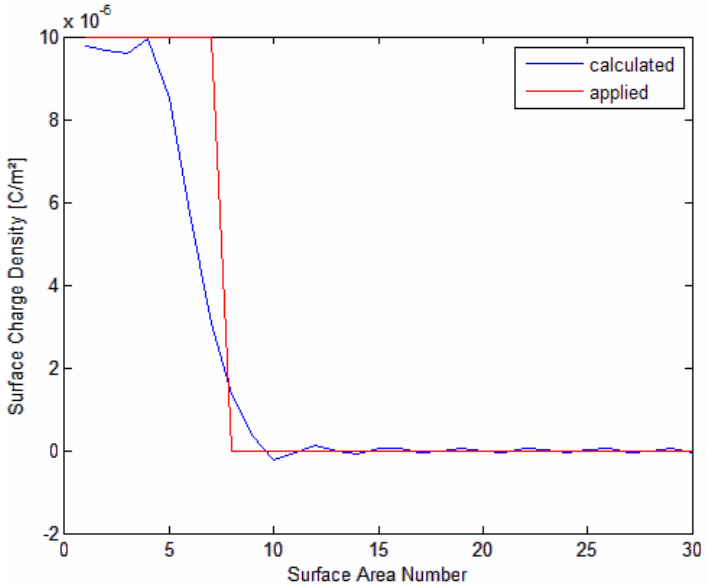

Fig. 5.15 – Estimated (blue) and applied (red) surface charge density with 1% white noise added to probe signal.

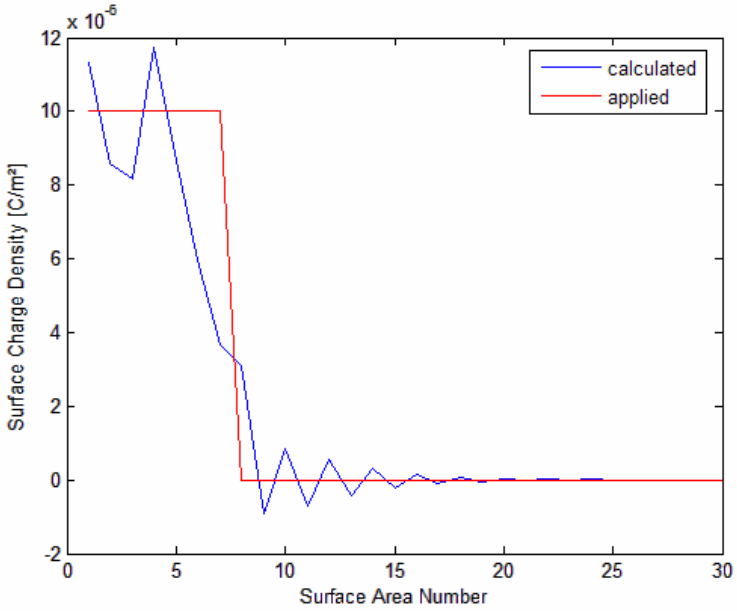

Fig. 5.16 - Estimated (blue) and applied (red) surface charge density with 10% white noise added to probe signal.

The results presented in Fig. 5.15 and Fig. 5.16 show that a rapid change in surface charge density along the rod is difficult to calculate. The difference between applied and calculated surface charge around the knee is high, but generally, the deviation between applied and calculated charge density is small. It should be noted that such a dramatic change in surface charge density along the surface is unlikely to appear after a typical discharge.

5.2.2 Boundary Element Method with regularization

The boundary element method (BEM) is a method that, in combination with regularization, has been evaluated to calculate the surface charge distribution based on the probe response. In this work, two different methods has been used and evaluated. The problem addressed here is sketched in Fig. 5.17.

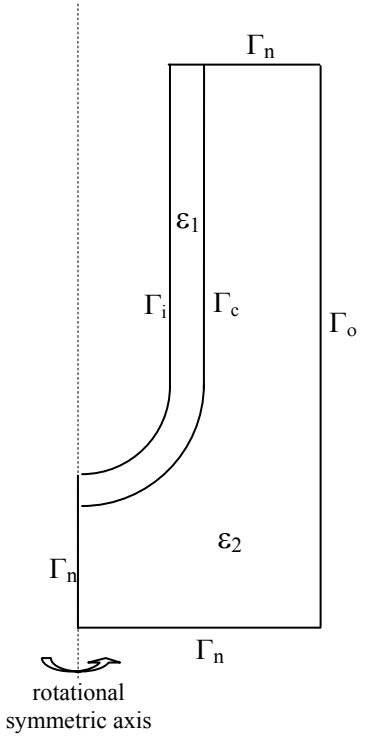

Fig. 5.17 – Problem to be solved using BEM.

The governing equation for this problem is Poisson's equation:

$$-\varepsilon\nabla^2 u = \rho \tag{5.11}$$

In this case the following boundary conditions are used:

$$\frac{\partial u}{\partial n} = 0, \text{ on } \Gamma_n \tag{5.12}$$

The measurement cylinder, Γ_o, is an earthed conductive cylinder:

$$u = 0, \text{ on } \Gamma_o \tag{5.13}$$

The surface charges on the insulating surface, Γ_c, induces mirror charges on the boundary Γ_o that is measured as an electric field along the boundary:

$$\frac{\partial u}{\partial n} = \frac{\rho}{\varepsilon} = \mathrm{f}, \text{ on } \Gamma_o \tag{5.14}$$

The accumulated surface charges will lead to a potential on the interior boundary Γ_c:

$$u = g, \text{ on } \Gamma_c \tag{5.15}$$

The rod is earthed, yielding:

$$u = 0, \text{ on } \Gamma_i \tag{5.16}$$

Normally, when performing BEM calculations the source of the field is known and with given boundary conditions, the problem can easily be solved. In this case, no information about the boundary Γ_c is known, but additional information on the boundary Γ_o is known (u = 0 and du/d**n** from measurements). The problem in Fig. 5.17 is therefore an inverse problem. One way of solving it is to split the original problem into two sub-problems. Considering the simplified geometry of the problem in Fig. 5.17:

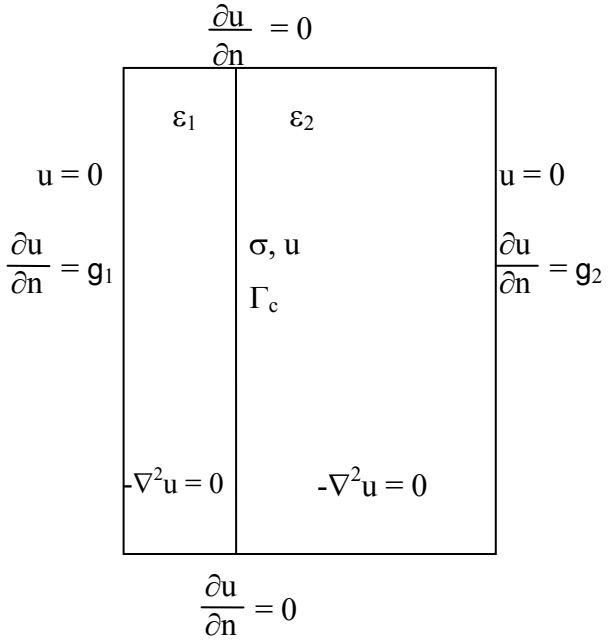

Fig. 5.18 – Simplified problem geometry.

Accumulated surface charges on the interior boundary Γ_c induce mirror charges on both outer boundaries to the right and left in Fig. 5.18. The total sum of the mirror charges on the outer boundaries is equal to the accumulated surface charges but of opposite sign. This can be used to divide the problem in two sub-problems as shown in Fig. 5.19, simplifying the field calculations.

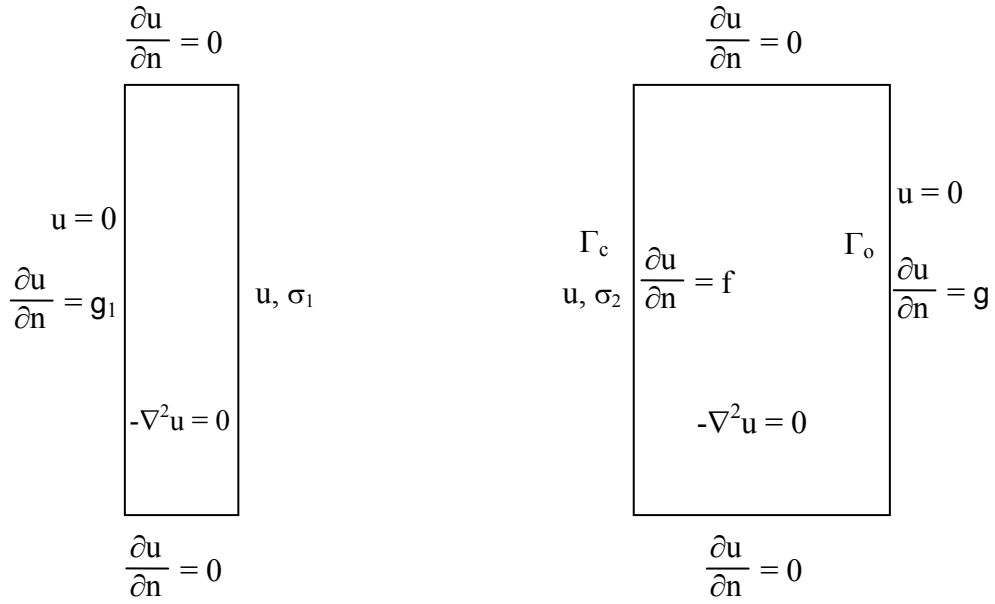

Fig. 5.19 – Division of the problem in Fig. 5.18 into two sub-problems.

The field problem in Fig. 5.19 is now a Laplacian field problem, where neither u nor du/d**n** is known on Γ_c. However, on Γ_o both the u and du/d**n** are known. This makes the problem ill-posed.

The relation between surface charge on the interior boundary (solid surface) and induced mirror charges for the configuration used in Fig. 5.17 can be calculated by the use of FEM software (COMSOL Multiphysics ®).
For the problem sketched in Fig. 5.17, the relation between induced mirror charge on the measurement cylinder and surface charge on a surface area is given in Fig. 5.20.

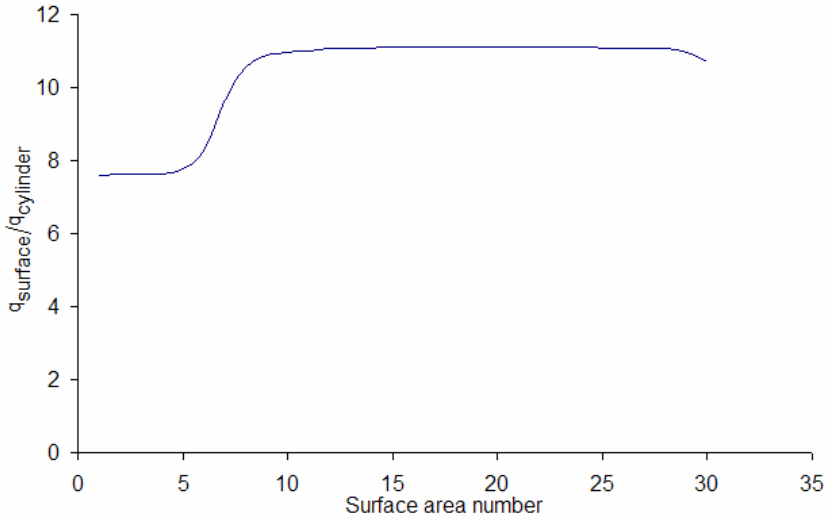

Fig. 5.20 – Relation between accumulated surface charge and induced mirror charge on the cylinder surface calculated using FEM software.

In order to solve this problem a simplified version of the problem in Fig. 5.17 is introduced as shown in Fig. 5.21. The reformulated problem to be addressed is restricted to the boundaries around the air gap ignoring the solid insulation.

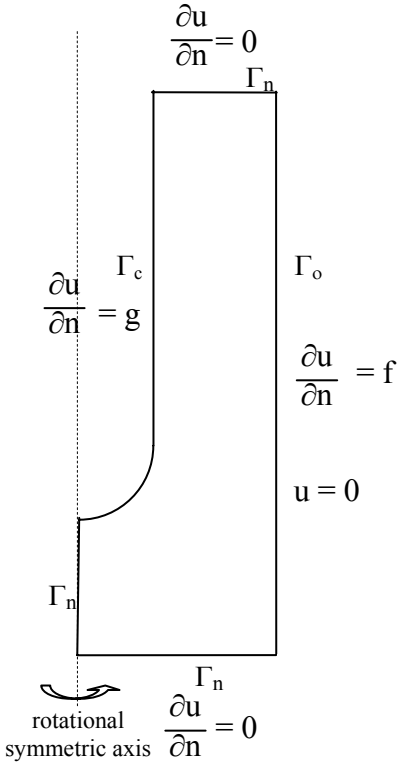

Fig. 5.21 – Boundary conditions for the simplified BEM-problem.

The boundary conditions for the simplified problem in Fig. 5.17 are the same as for the problem sketched in Fig. 5.21.

Since the conditions on boundary (Γ_c) is unknown and the boundary Γ_o has a known u and du/d**n**, it is possible to find a solution using BEM [44-46] and regularization. When using BEM, u and du/d**n** along the boundaries are calculated. By the use of Green's theorem, the electric field in the domain can be calculated in a subsequent calculation [44-46]:

When solving the problem using the boundary element method, the following equation system is generated:

$$Hu - Gq = 0 \tag{5.17}$$

where q = du/d**n**. Separating unknowns from knowns Eq. (5.17) becomes:

$$Ax = Bd = b \tag{5.18}$$

where A is the coefficient matrix, x a vector of unknown values of potential and electric field on the boundaries while b is an independent vector. The solution of this equation gives the unknown values of u and q.

Normally in a BEM problem, one of the two border conditions is known. In this case, both the du/d**n** and u are known for Γ_o. While for the solid insulation surface, Γ_c, both u and du/d**n** are unknown. This makes the problem presented here ill-posed as there is no unique solution to the problem. In order to make an estimation of the unknowns on Γ_c, regularization is used.

The first method used is based on using TSVD on the A matrix as described in Section 5.2.1 to calculate the unknown values of u and q.

A second method is to use SVD on the A–matrix to be inverted and regularized. A regularization parameter α_{reg} is added to the diagonal matrix Σ calculated by SVD (see Appendix A):

$$\hat{A} = U\Sigma V^T \tag{5.19}$$

$$\Sigma_{inv} = \left(\frac{\Sigma}{|\Sigma|} \right)^2 + \alpha_{reg} \left| \Sigma(1,1) \right| \tag{5.20}$$

$$\hat{A}^{-1} = V\Sigma_{inv} U^T \tag{5.21}$$

where the parameter α_{reg} should be chosen to be as small as possible.

5.2.3 Finite Element Method with regularization

By the use of the Finite Element Method (FEM) in combination with regularization, a surface charge distribution based on the probe measurements can be calculated.
The problem is the same as for BEM given in Fig. 5.17 with the boundary conditions Eq. (5.12) - (5.15).

As for BEM, a simplified version of the original problem is introduced, where only the air gap and the boundaries around it are considered.

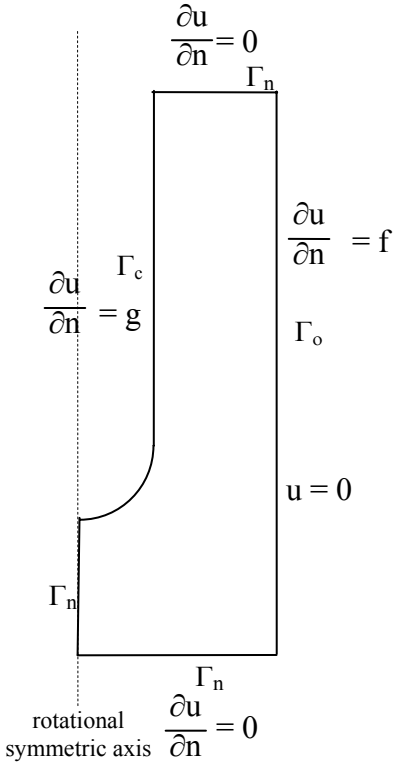

Fig. 5.22 – Simplified problem description with boundary conditions for FEM analysis. The left-hand side (Γ_c) represents the insulating surface while the right side (Γ_o) represents the measurement cylinder.

The boundary conditions of the simplified problem in Fig. 5.22 are the same given for the BEM problem.

In the Finite Element Method, the problem domain is divided into finite elements, giving a set of basic functions used to describe and approximate solution. By using e.g. a variational method, the differential potential equation is transformed into an algebraic equation system, where the unknown are the values of the potential at each node. To each node in the mesh, there is one basic function associated [47]. Compared to BEM, only potential values are evaluated, but they need to be calculated in the whole problem domain. The resulting algebraic equation system:

$$Ax = b \tag{5.22}$$

is ill-posed due to the boundary conditions given in Fig. 5.22.

In the taylor made FEM code used [48, 49] the value u = 0 on the boundary Γ_o is relaxed and an approximate solution where:

$$u \leq e_{threshold} \tag{5.23}$$

is calculated.

The FEM code has been tested on some of the same simulated probe responses used in Section 5.2.1 without any noise added.

The regularization parameter α_{reg} is chosen to 0.1 and was found by trial and error.

Example 1

The applied surface charge density used here is shown in Fig. 5.5.

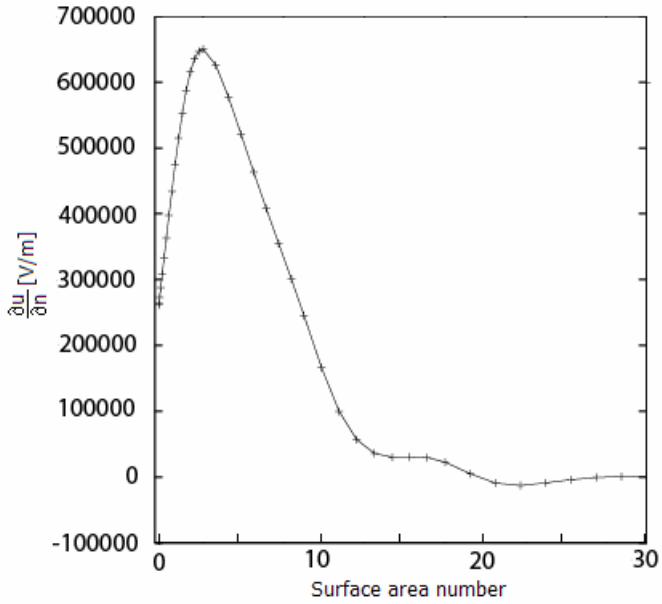

Fig. 5.23 – Calculated surface field strength in the air gap using FEM with regularization. No noise was added to the probe response.

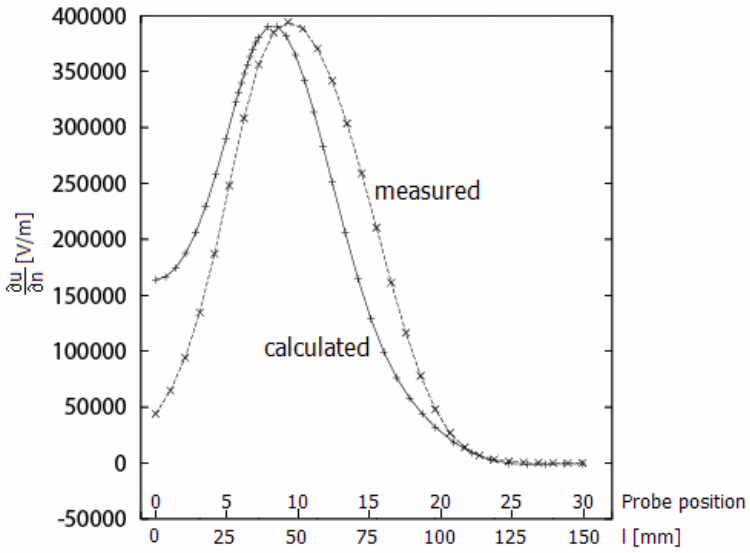

Fig. 5.24 – Calculated probe response (+) based on surface charge distribution in Fig. 5.23 using FEM and regularization vs. simulated probe response.

Example 2:
The applied surface charge density used is shown in Fig. 5.15.

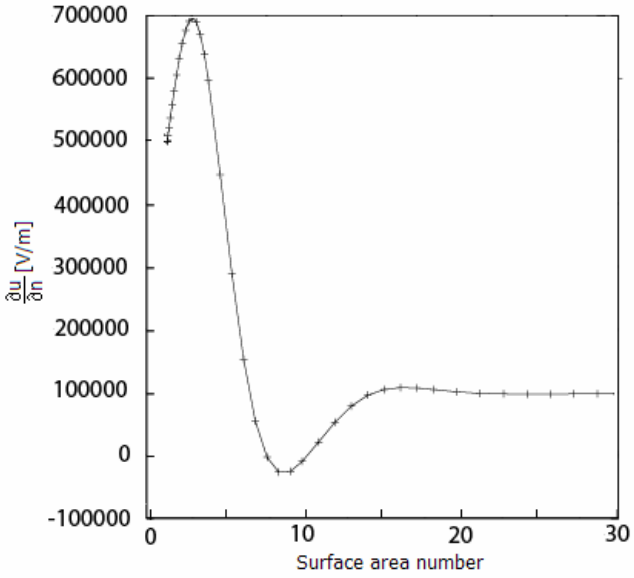

Fig. 5.25 – Calculated surface field strength in the air gap using FEM with regularization. No noise was added to the probe response.

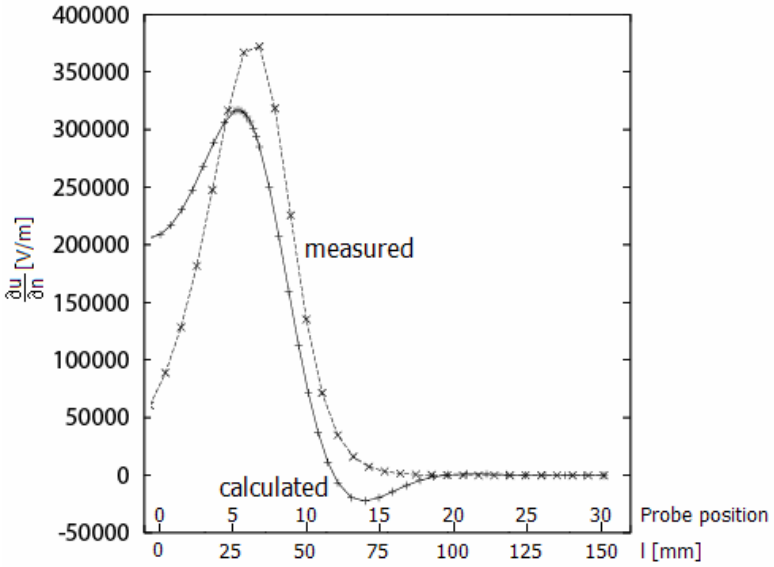

Fig. 5.26 – Calculated probe response (+) based on surface charge distribution in Fig. 5.25 using FEM and regularization vs. simulated probe response.

For both examples, the calculated probe response compared to the simulated is relatively large mainly cased by a phase shift. The deviation can be explained as a poor coupling between the lower part of the rod and the measurement cylinder.

5.3 Surface charge evaluation using TSVD on the λ-method

Cases I and II: Positive impulses

The two following examples show typical discharge activity in the air gap during application of a positive lightning impulse and the corresponding probe responses measured as described in Section 4.1.5. The first example is a case with a relatively moderate discharge activity in the air gap, while the second one shows an example where the discharges spreads widely along the rod and covers the air gap.

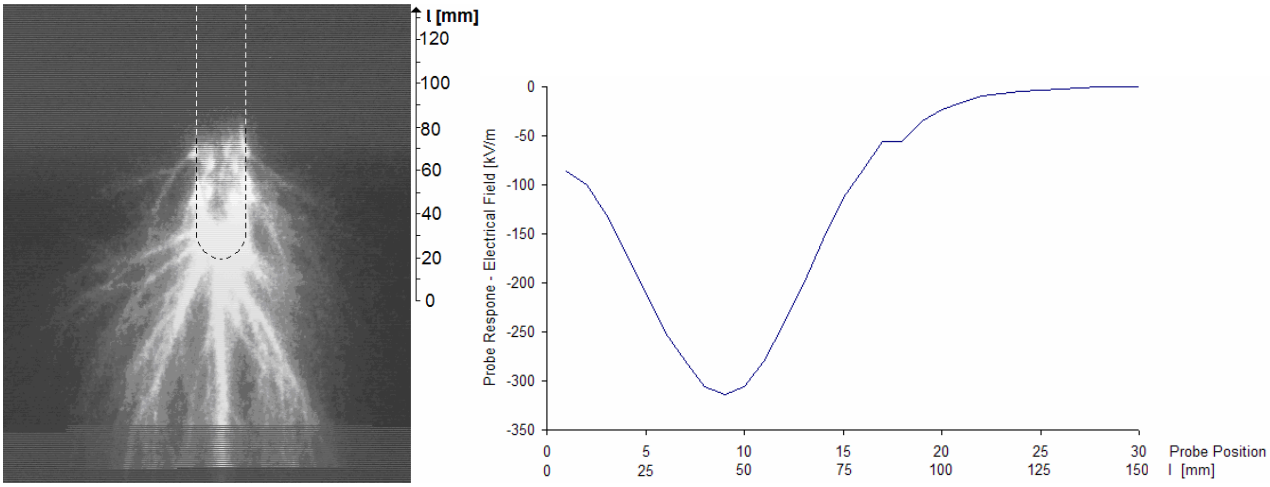

Fig. 5.27 – Case I: Left: Video image of discharges. Right: Corresponding probe response. Electrode distance 90 mm, applied voltage 98.4 kV (no electric breakdown)

Using TSVD on the λ-method as described in Section 5.2.1, the surface charge distribution can be estimated.

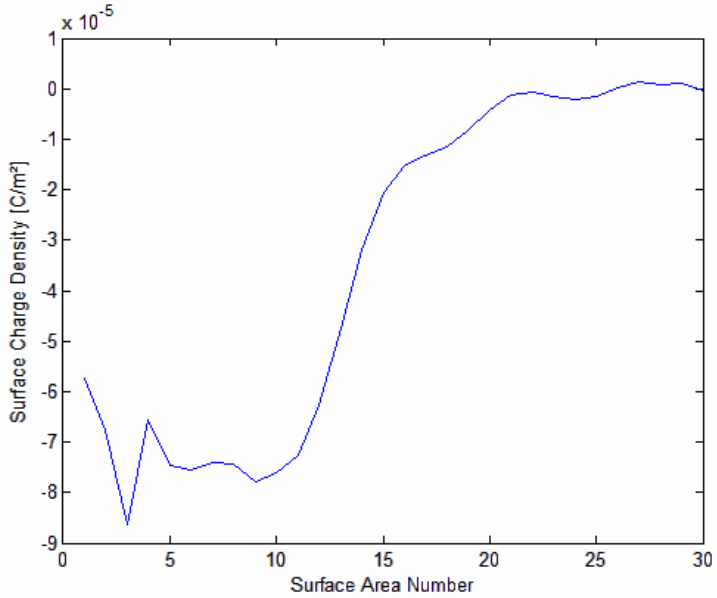

Fig. 5.28 – Estimated surface charge density based on probe response in Fig. 5.27 using TSVD on the λ-method.

The correlation between the video image and estimated surface charge is good. In Fig. 5.27 most of the discharge activity occurs around the tip of the rod and the first centimetres upwards where according to calculations the surface charge density is also at its highest.

The second example of positive discharges is shown in Fig. 5.29. Here the discharge activity is spread widely along the insulating surface and covers most of the air gap. The corresponding probe response shows a good correlation with the discharge video image.

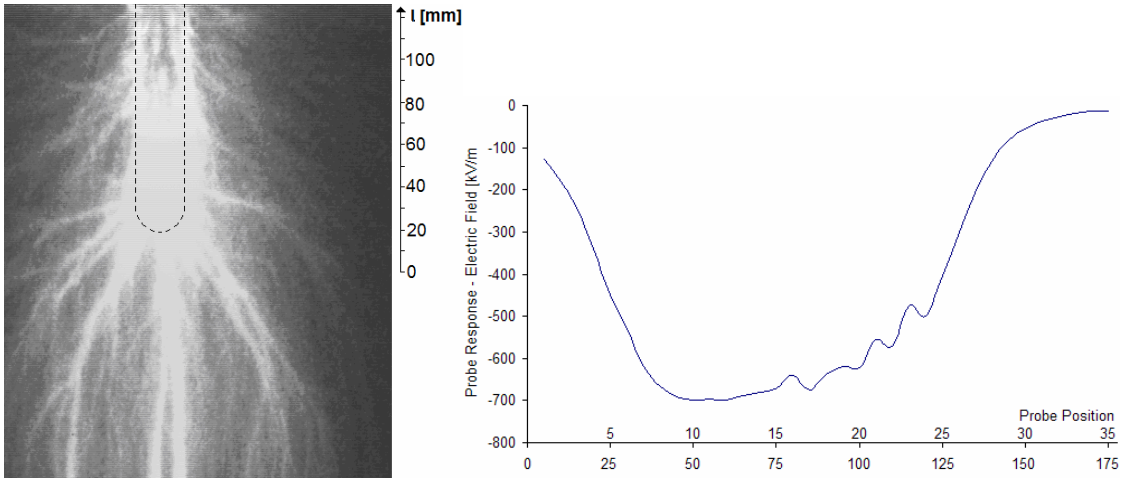

Fig. 5.29 – Case II: Left: Video image of discharges. Right: Corresponding probe response. Electrode distance 101 mm, applied voltage 126 kV (no electric breakdown)

Based on the probe response, the surface charge density using TSVD on the λ-method can be estimated:

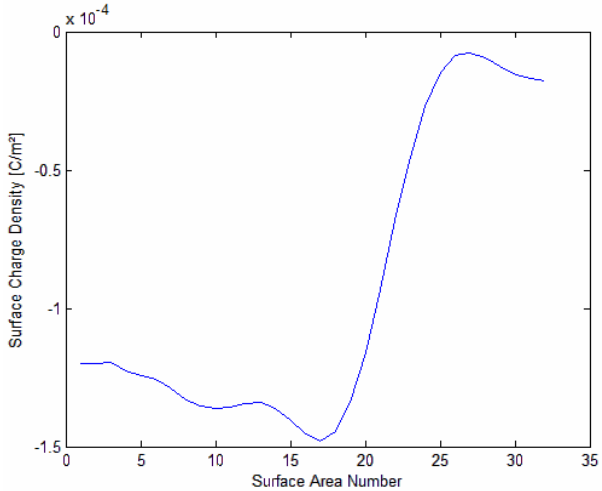

Fig. 5.30 – Estimated surface charge density for case II based on probe response in Fig. 5.29 using TSVD on the λ-method.

The correlation between the video image in Fig. 5.29 and estimated surface charge density is good. Compared to the estimated surface charge density for the first case, the charge density is 2 times higher and covers a greater part of the rod, in accordance with the recorded video images.

Cases III and IV: Negative impulses

Some typical images and corresponding probe measurements are shown in Fig. 5.31 and Fig. 5.33. As for positive impulses, both a small and large discharge is shown and the corresponding calculation of the resulting surface charge density is shown in Fig. 5.32 and Fig. 5.34 respectively.

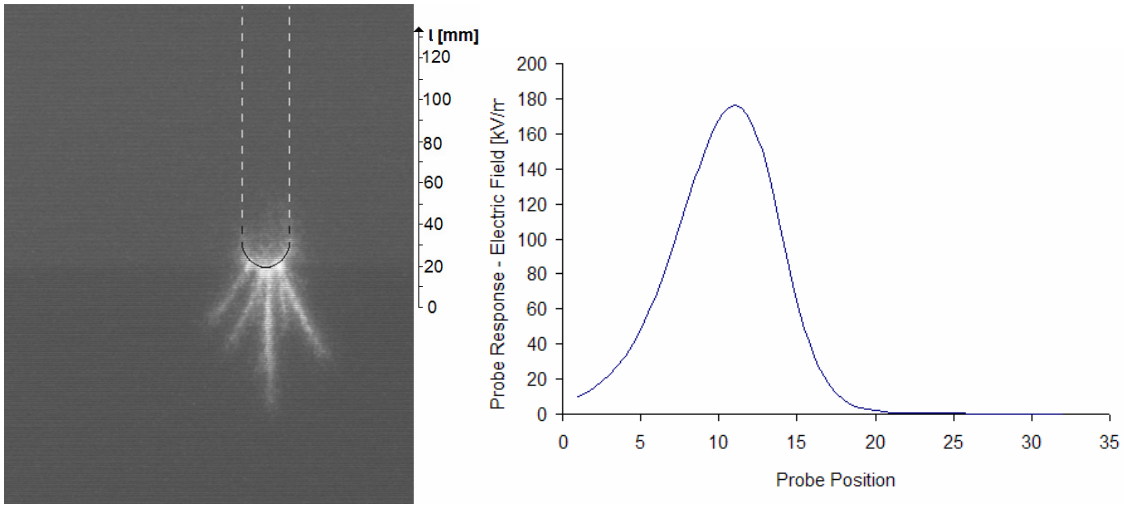

Fig. 5.31 – Case III: Left: Video image of discharges. Right: Corresponding probe response. Electrode distance 85 mm, applied voltage -104 kV (no electric breakdown)

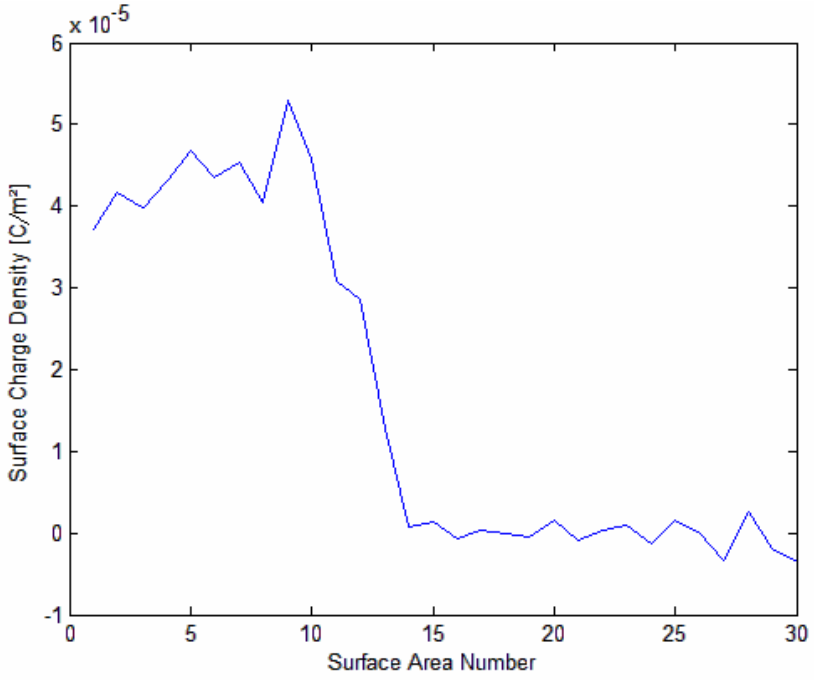

Fig. 5.32 - Estimated surface charge density based on probe response in Fig. 5.31 using TSVD on the λ-method.

The video image of accumulated discharge activities, probe response and calculated surface charge correlate well.

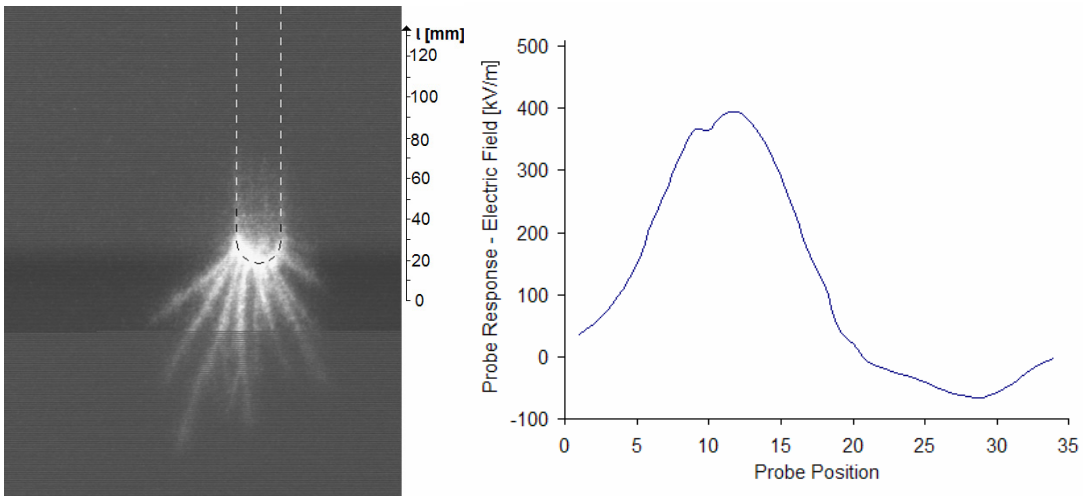

Fig. 5.33 – Case IV: Left: Video image of discharges. Right: Corresponding probe response. Electrode distance 85 mm, applied voltage -112 kV (no electric breakdown of the insulation system)

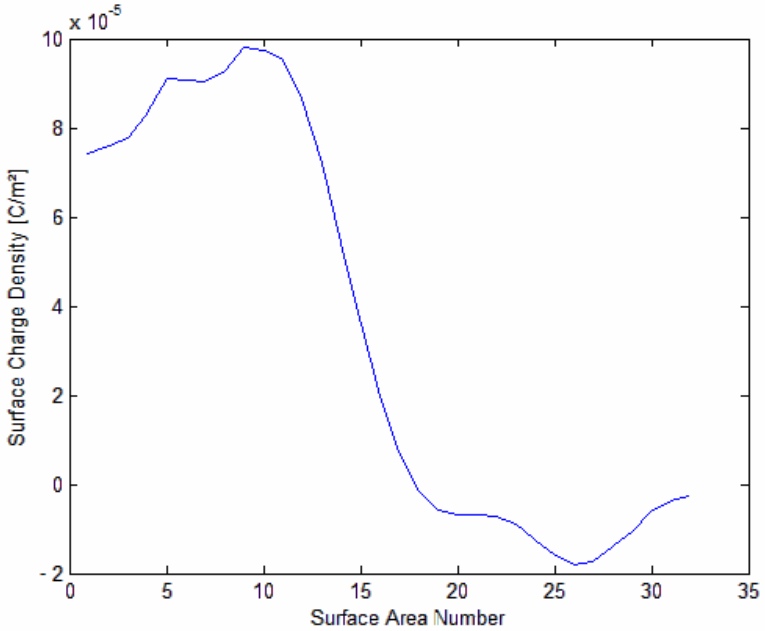

Fig. 5.34 - Estimated surface charge density based on probe response in Fig. 5.33 using TSVD on the λ-method.

As for the first case, there is a good correlation between the video image of the discharge activities, measured probe response and estimated surface charge density.

5.4 Surface charge evaluation using BEM

Evaluation of the probe response can also be done using BEM in combination with regularization. In this thesis the problem is solved using MATLAB® [50].
Discretization of the problem is shown in Fig. 5.35. For probe responses, the same responses are selected as used in Section 5.3. This is in order to facilitate a comparison between Pedersen's λ-method combined with regularization (TSVD) and BEM with regularization.

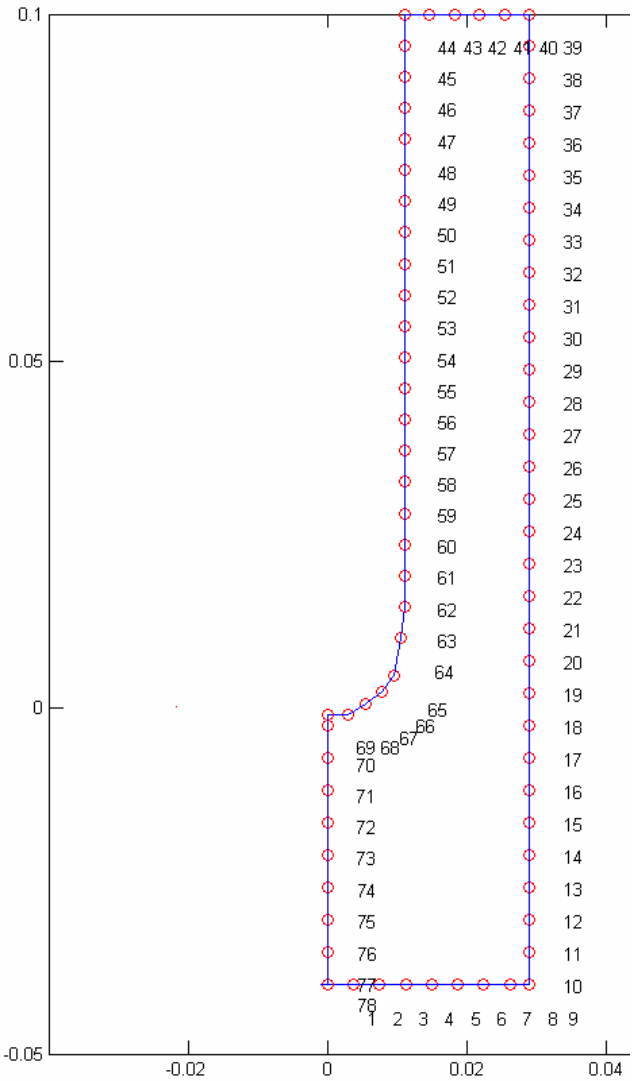

Fig. 5.35 – Division of the BEM problem into segments. Rotational symmetry around x=0.

In the BEM code, the user has to choose between TSVD and regularization by adding a regularization parameter α_{reg}. For TSVD, the program automatically chooses the best numerical rank, while for the second type of regularization a value for α_{reg} has to be chosen by the user. The value used for α_{reg} here is $1 \cdot 10^{-5}$, a value determined by trial and failing. The original BEM code was written by Dr Varslot, currently at Rensselaer Polytechnic Institute, USA, and has been modified for rotational symmetry for use here.

Here an ideal case without any noise added is considered. The probe response used is given in Fig. 5.36 while the applied surface charge density is given in Fig. 5.38.

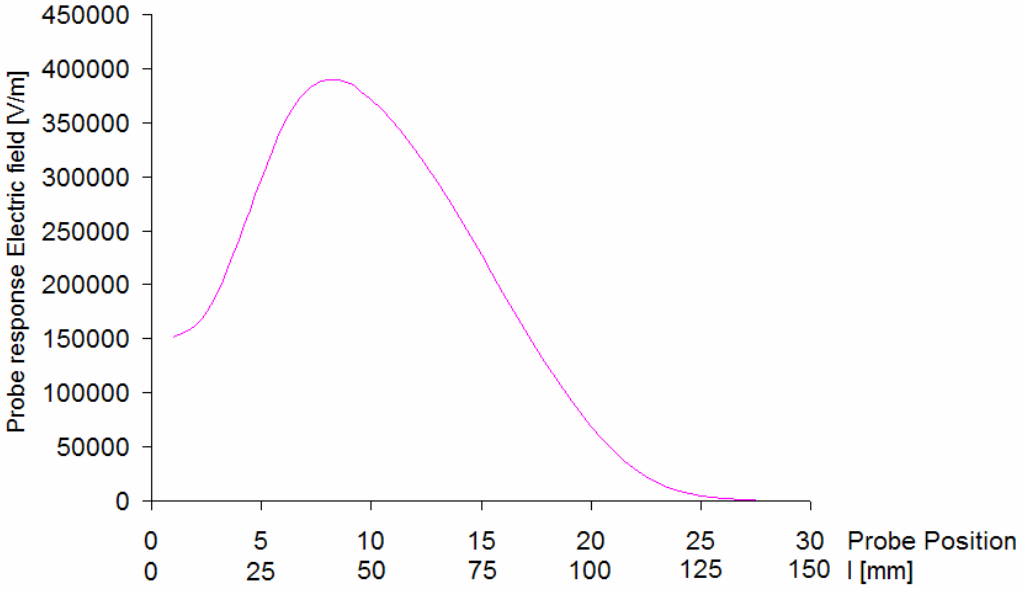

Fig. 5.36 – Probe response; calculated in Comsol and used as input in the BEM calculation.

The calculated electric field distribution is given in Fig. 5.37 and the surface charge distribution in Fig. 5.38.

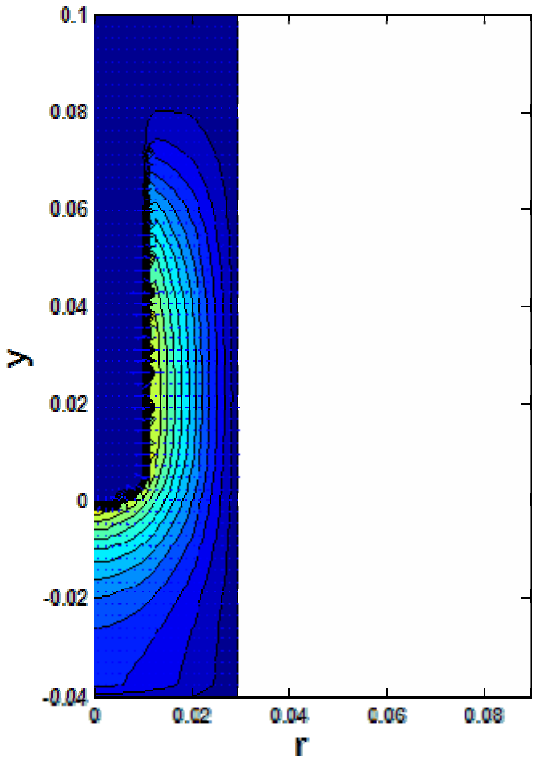

Fig. 5.37 – Equipotential plot using BEM with TSVD based on probe response in Fig. 5.36.

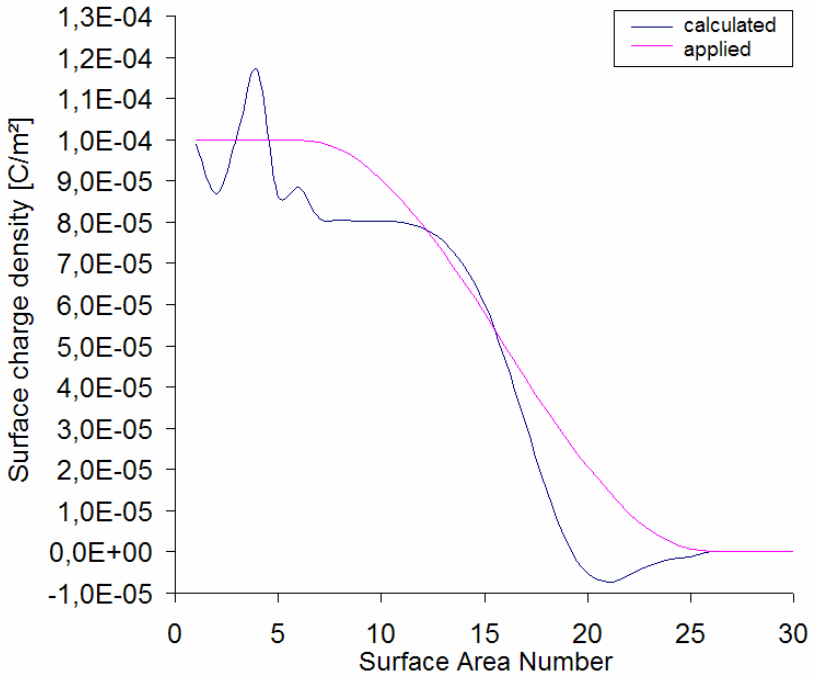

Fig. 5.38 – Surface charge density using BEM based on probe response in Fig. 5.36 compared to the applied surface charge. Regulation parameter $\alpha_{reg} = 1 \cdot 10^{-5}$(found by trial and error.)

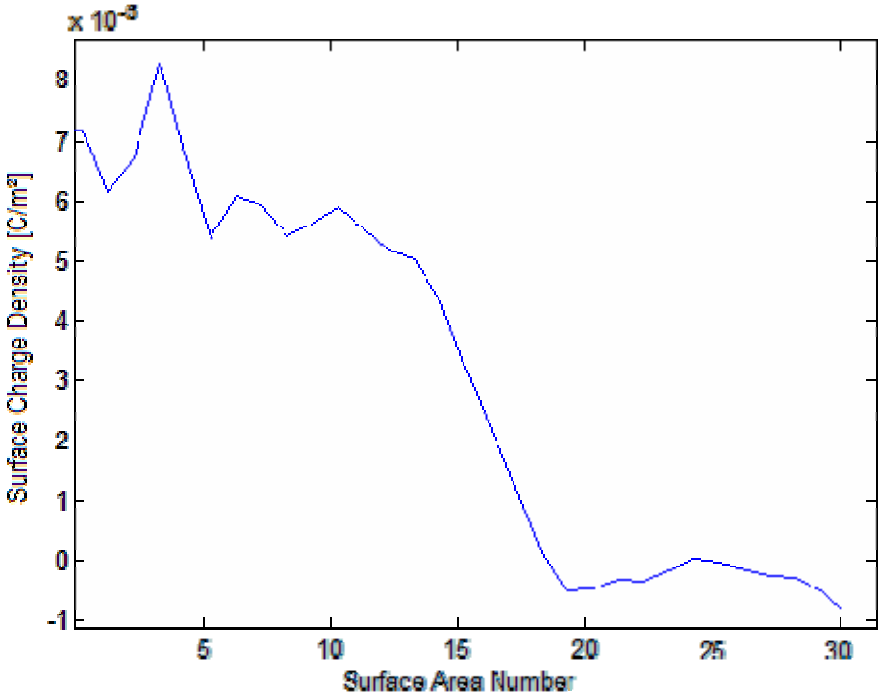

Fig. 5.39 – Surface charge density calculated by use of BEM in combination with TSVD as regularization.

As seen in Fig. 5.38 and Fig. 5.39 the calculated surface charge distributions follow the applied charge density, but the deviation is around 20-30% in both cases.

5.5 Surface charge evaluation using FEM

The third method tested for calculation of surface charges is the finite element method together with regularization according to Eq. **Error! Reference source not found.**. The regularization parameter α_{reg} is chosen to 0.1 by trial and error. Examples shown here are based on the same probe responses as for TSVD (Section 5.3) considering one positive and negative case (cases I and III respectively).

Case I – Positive impulse (Applied voltage 98.4 kV, electrode distance 90 mm)

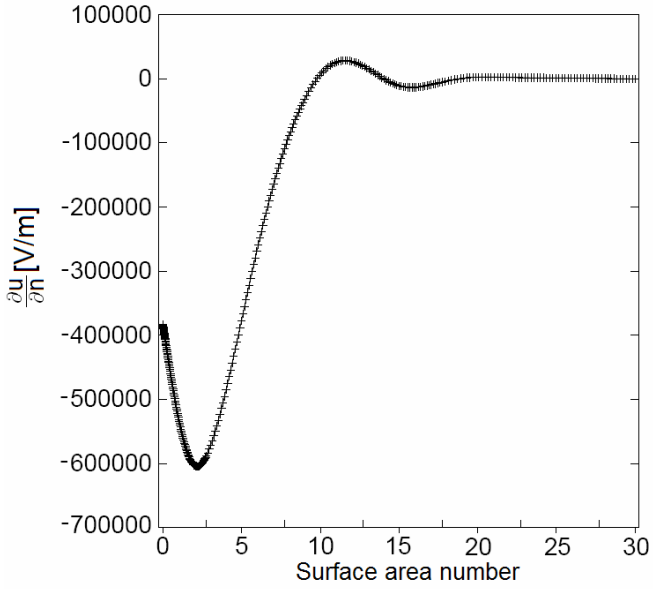

Fig. 5.40 –Calculated surface field strength of the air gap case I. Corresponding probe response and video image in Fig. 5.27.

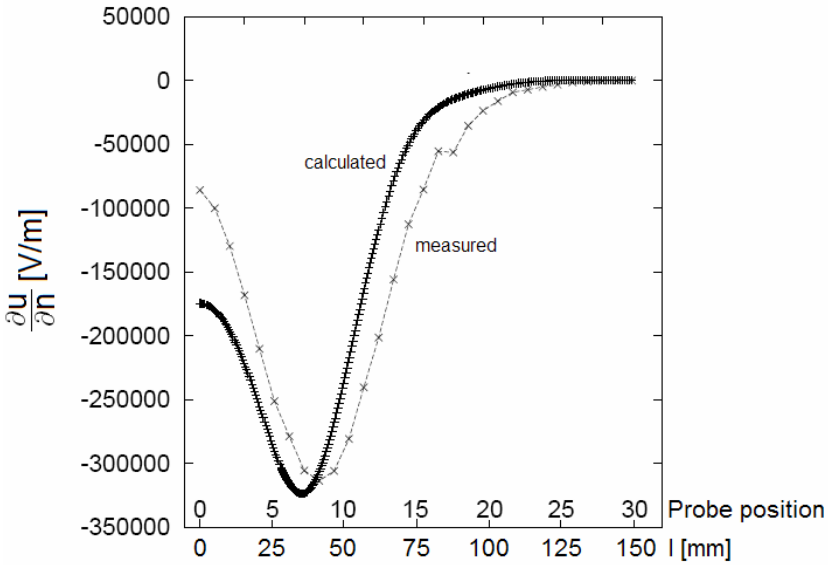

Fig. 5.41 – Calculated probe response (+) based on surface charge distribution in Fig. 5.40 using FEM and regularization vs. measured probe response (x).

Case III – Negative impulse (Applied voltage -104 kV, electrode distance 85 mm)

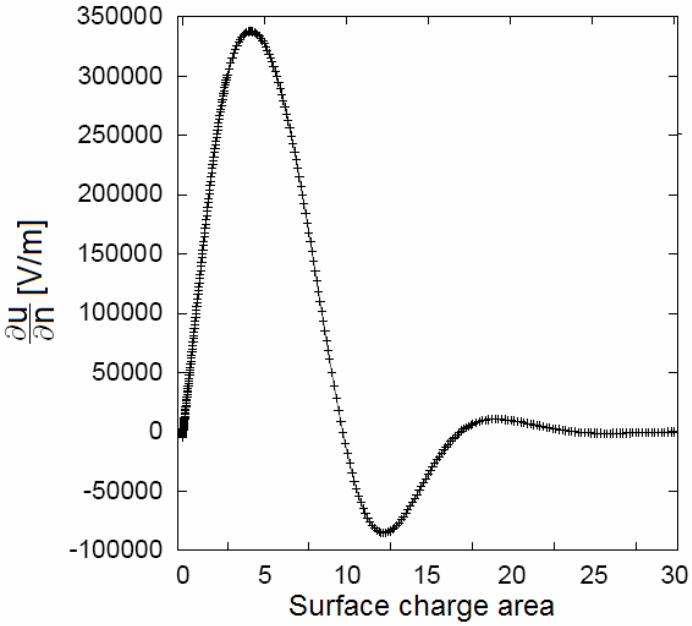

Fig. 5.42 – Calculated surface field strength of the air gap case III. Corresponding probe response and video image in Fig. 5.31.

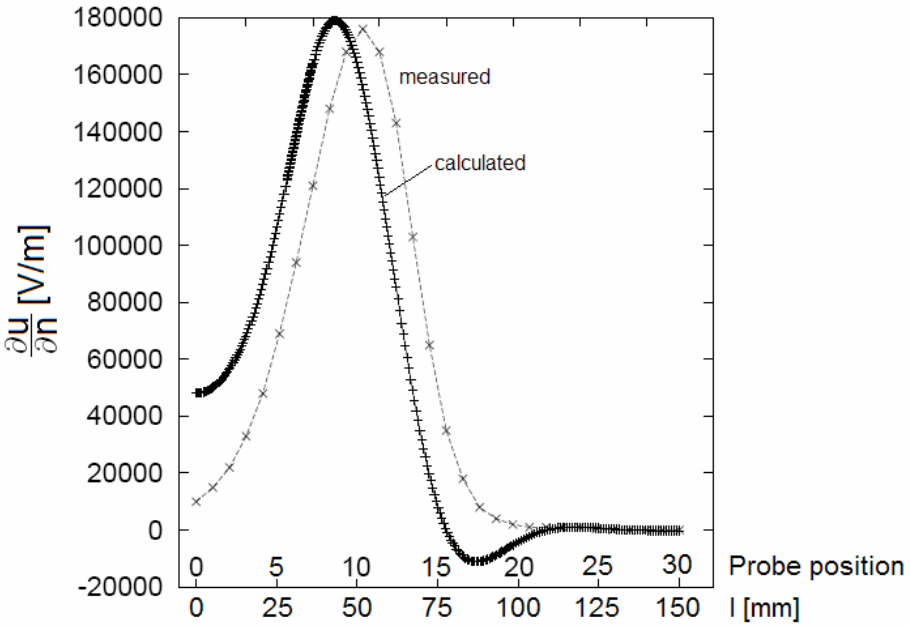

Fig. 5.43 - Calculated probe response (+) based on surface charge distribution in Fig. 5.42 calculated using FEM and regularization vs. measured probe response (x).

The regularization parameter α_{reg} is chosen minimizing the error between the measured and calculated probe response. As seen in Fig. 5.41 and Fig. 5.43 the deviation between measured and calculated probe response is relatively large mainly caused by a phase shift. The deviation can be explained to the poor coupling between the hemispheric part

of the rod and the measurement cylinder. Comparing the calculated surface charge density with the video images of Fig. 5.27 and Fig. 5.31, the correlation between the found densities and video image around the tip is low, while correlation further up the rod is good. This can be caused by the model geometry. The method using TSVD on the λ-method gives a better and more correct estimation of the surface charge density than both FEM and BEM with regularization.

5.6 Electric field distribution before and after discharges

Initially, before ignition of discharge activity, the field distribution of the insulation system is Laplacian. Under and after discharge activity, the field distribution is the sum of the Laplacian field distribution and the charge induced field according to Eq. (2.3).

The surface charge density distributions found by using the λ-method with TSVD on the measured probe responses are entered into a FEM model and the expected resulting electric field distribution is calculated for the impulse voltage with and without surface charges. For 2 positive and 2 negative lightning impulse voltages, examples with modest and stronger air gap discharge activity are reviewed. The surface charge distributions used here were calculated in Section 5.3.

Case I: Positive lightning impulse (98.4 kV)

In Fig. 5.44 a) the electric field distribution for case I is shown. Around the hemispheric part the field is initially high enough to initiate discharges, but as seen in Fig. 5.27 and discussed earlier, the discharges spread further upwards along the rod. In the end of this process, the electric field in the air is reduced and the solid insulation takes a greater part of the total electric stress.
Measurements of the surface charge distribution were done after the applied lightning impulse voltage has died out and the rod is earthed. The surface charge distribution for case I is given in Fig. 5.28, page 73.

Fig. 5.44 b) presents the total electric field with 98.4 kV applied and the surface charge distribution. Compared to the initial Laplacian distribution, it is seen that the stress within the solid insulation has increased due to the accumulated surface charges. It is expected that the highest electric field in the air gap should be about or lower than the discharge inception field. However, the electric field is higher than the discharge inception field. This can be the result of recombination after the applied voltage has been reduced to zero.

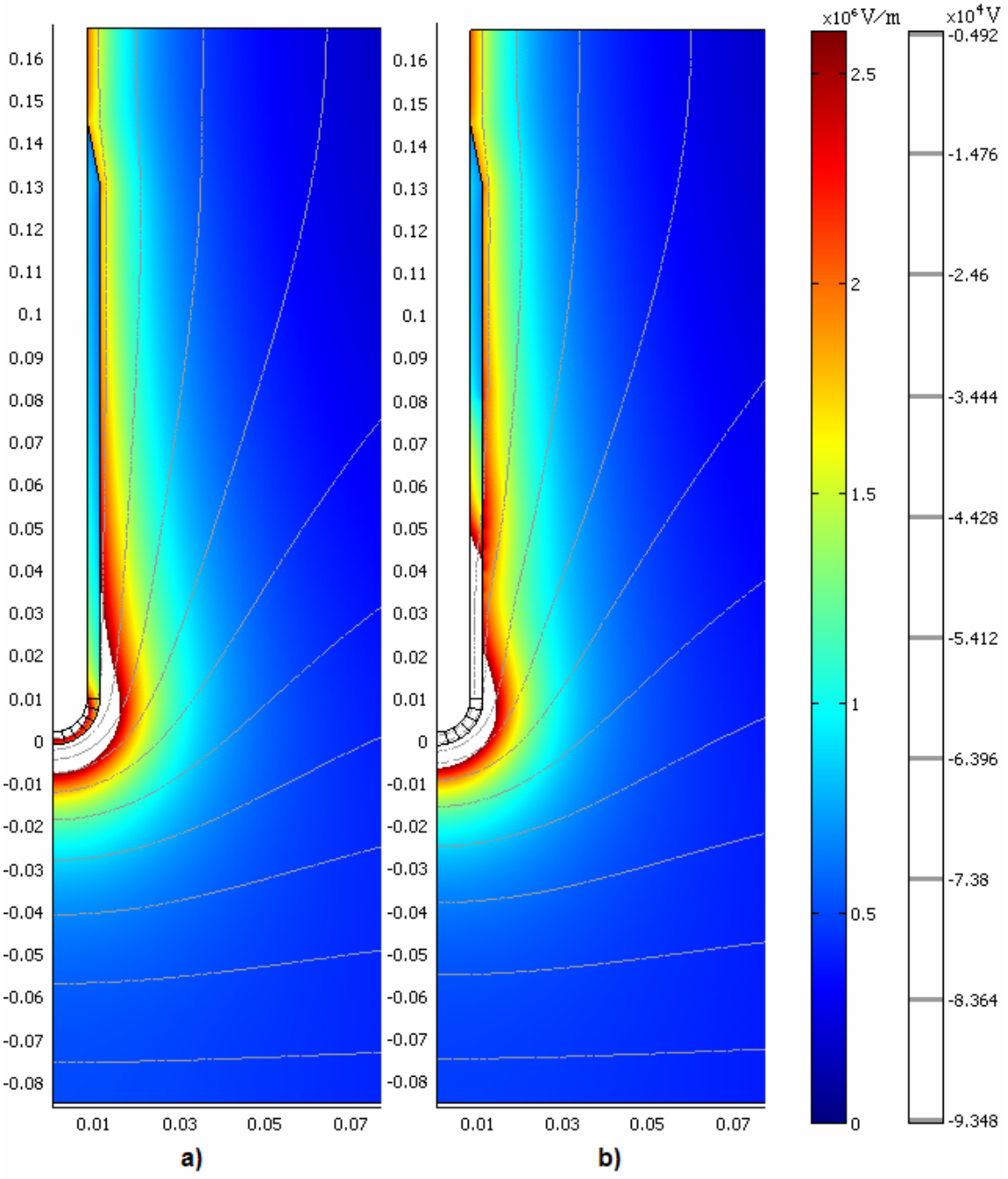

Fig. 5.44 – a) Electric field distribution case I. Rotational symmetry around x = 0. The white area around the hemispheric part of the rod indicates where the electric field is high enough to initiate discharge activity in atmospheric air. Corresponding discharge image in Fig. 5.27 (page 73). Applied voltage 98.4kV and electrode distance 90 mm.
b) Field distribution for case I with surface charge distribution found in SEction 5.3. Compared to a), a larger part of the stress is now over the solid insulation. However, the electric field is higher than the discharge inception field. This can be the result of recombination after the applied voltage has been reduced to zero.

Case II: positive lightning impulse (126 kV)

The Laplacian field distribution for case II (high discharge activity during lightning impulse) is shown in Fig. 5.45 a). As for case I, discharge activity is observed further upwards along the rod than expected based on electric field calculations and streamer criterion (see also Fig. 5.29). Adding the surface charge density found by TSVD by the λ-method (shown in Fig. 5.30) the electric field distribution becomes as shown in Fig. 5.45 b).

Comparing the field calculations with and without surface charges, it can be seen that the maximum stress of the air gap is reduced due to accumulation of surface charges. As in case I, the maximum electric field of the air gap with surface charges is higher than the initiation field strength, indicating that also in this case recombination of charges takes place until the applied voltage has been reduced to zero.

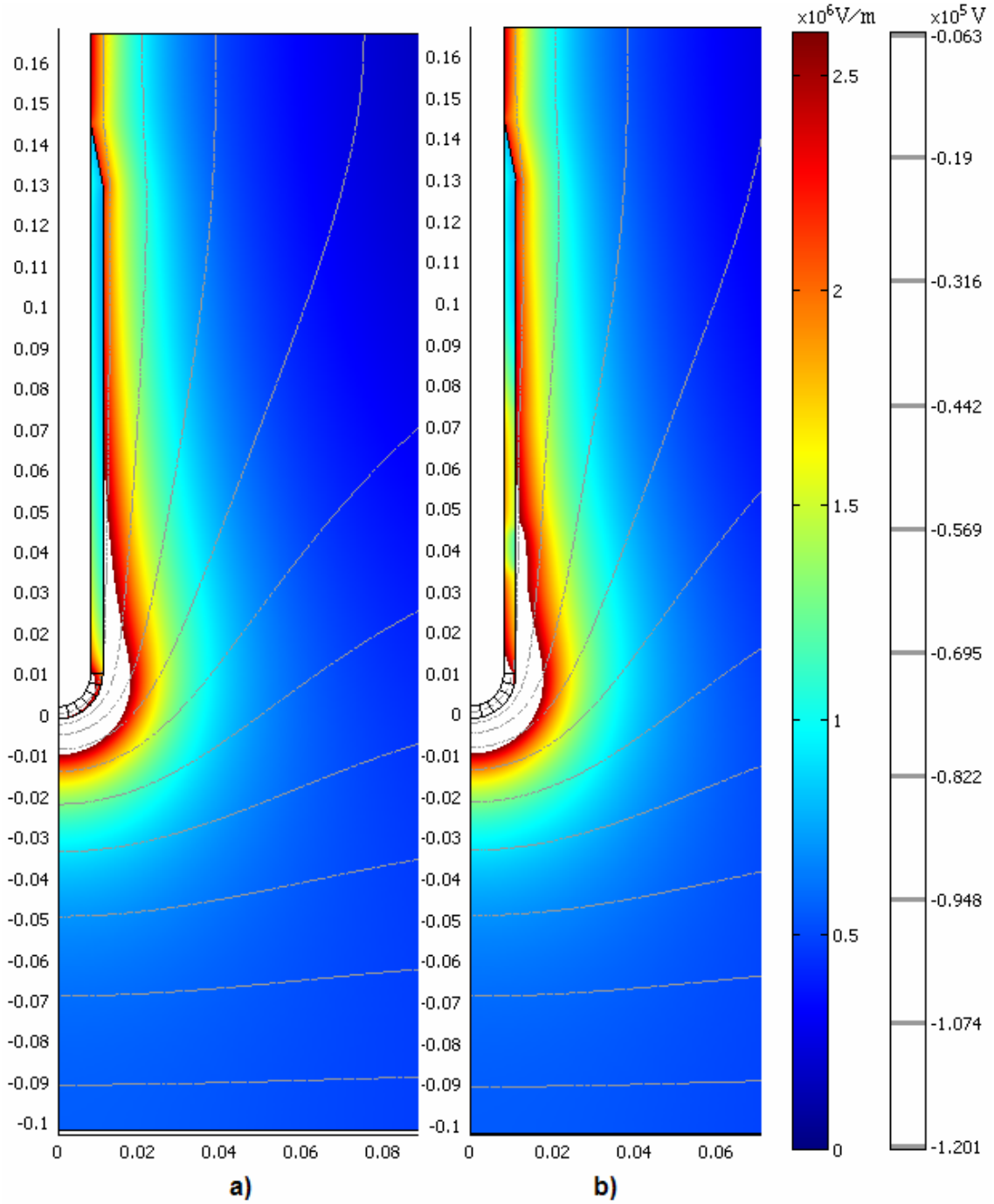

Fig. 5.45 – **a)** Laplacian field distribution for case II. Rotational symmetry around x = 0. The white area indicates where the electric field is high enough to initiate discharge activity in atmospheric air. Corresponding discharge image in Fig. 5.29 (page 74). Applied voltage 126 kV and electrode distance 101 mm.
b) Field distribution for case II with surface charge distribution found in Section 5.3. As expected, a larger part of the stress is now over the solid insulation. However, as for case I, the electric field is higher than the discharge inception field. This can be the result of recombination after the applied voltage has been reduced to zero.

The surface charge densities found in Section 5.3 are used to compare the electric field distribution for negative impulses with and without accumulated surface charges. Cases III and IV show a situation with modest and heavier air gap discharge activity respectively.

Case III: Negative lightning impulse (-104 kV)
In Fig. 5.46 a) it is easy to see that the electric field is high enough to cause discharges around the hemispheric part of the test object. Comparing the results of the electric field simulation with the video image of Fig. 5.31, the strongest discharges were found around the tip of the rod with more diffuse discharges further upwards along the surface.

Adding the calculated surface charge distribution shown in Fig. 5.32, the field distribution becomes as shown in Fig. 5.46 b).

When comparing the two electric field distributions with and without surface charges, the electric field distribution is altered and more of the stress is transferred into the solid insulation. The field in the air gap is still high enough to cause new discharges, but as for cases I and II, the maximum electric field of the air gap with surface charges is higher than initiation field strength, indicating that also for negative lightning impulses, recombination of charges takes place until the applied voltage has been reduced to zero.

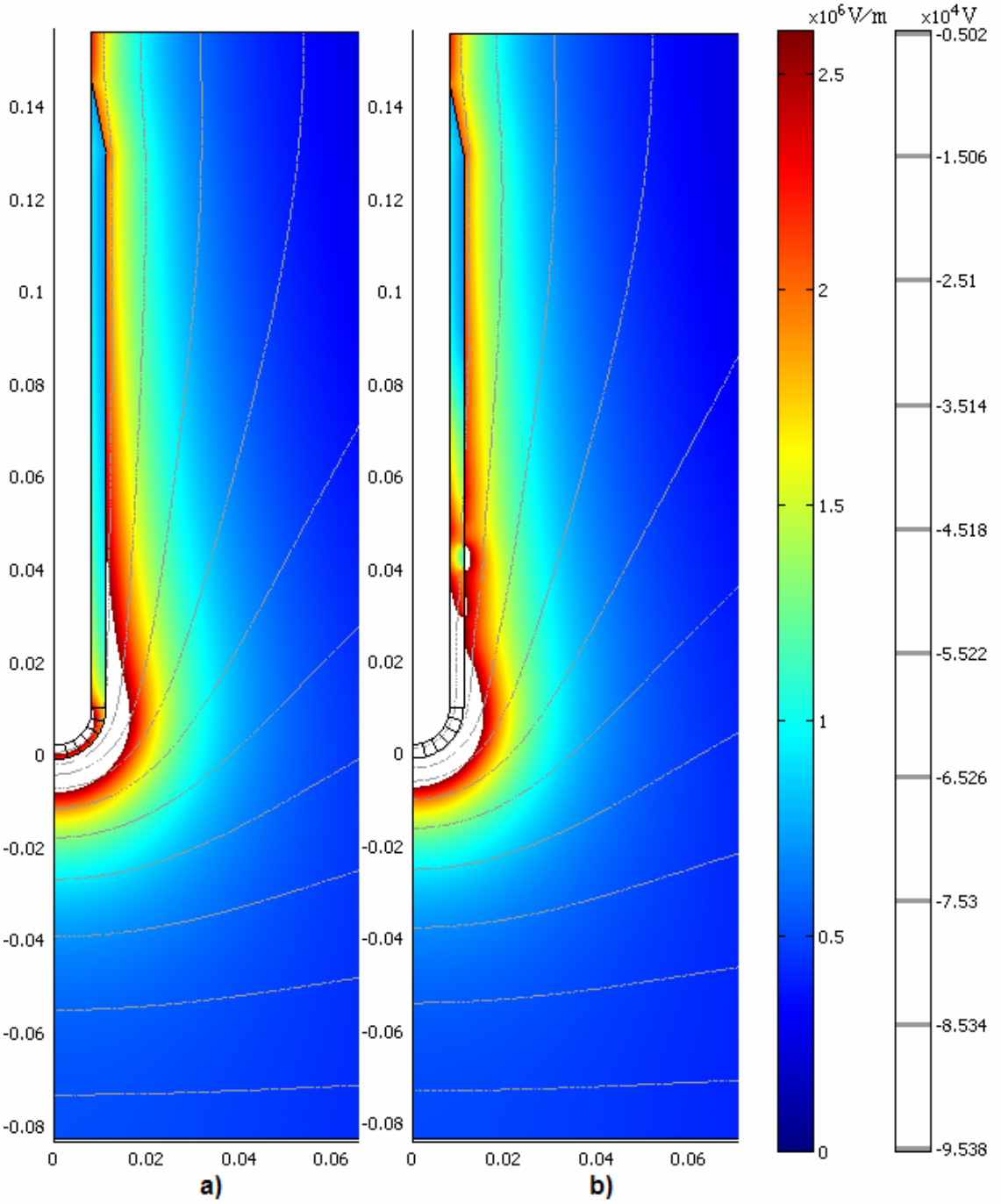

Fig. 5.46 – Capacitive field distribution for case III. Rotational symmetry around x=0. The white area indicates where the electric field is high enough to initiate discharge activity in atmospheric air. Corresponding discharge image in Fig. 5.31 (page 75).
b) Field distribution for case III with surface charge distribution found by TSVD. Due to the accumulated surface charges, the air gap stress is reduced. However, as in the two previous cases, the electric field in the air gap around the hemispheric part of the rod is high enough to cause new discharges. This can be the result of recombination after the applied voltage has been reduced to zero.

Case IV: Negative lightning impulse (-112 kV)
In Fig. 5.47 a) the Laplacian field distribution for case IV is simulated.
As for the previous cases, the field is initially high enough to cause discharge activity. Comparing the video image of Fig. 5.33 with the Laplacian field distribution, the discharge activities show a good correlation, but also here, the discharges spread further upwards along the rod than expected. If the discharge activity reaches the uncovered part of the rod, a breakdown of the insulation system occurs.

Adding the surface charges found previously with TSVD by the λ-method, the field distribution is altered as shown in Fig. 5.47 b). The surface charge distribution used is given in Fig. 5.34.

As in the previous cases, the surface charge density found after application of the lightning impulse voltage is not sufficient to prevent new discharge activity in the air gap. However, there are reasons to believe that the surface charge density is higher immediately after the discharging has taken place and that recombination directly after decreases the accumulated surface charges.

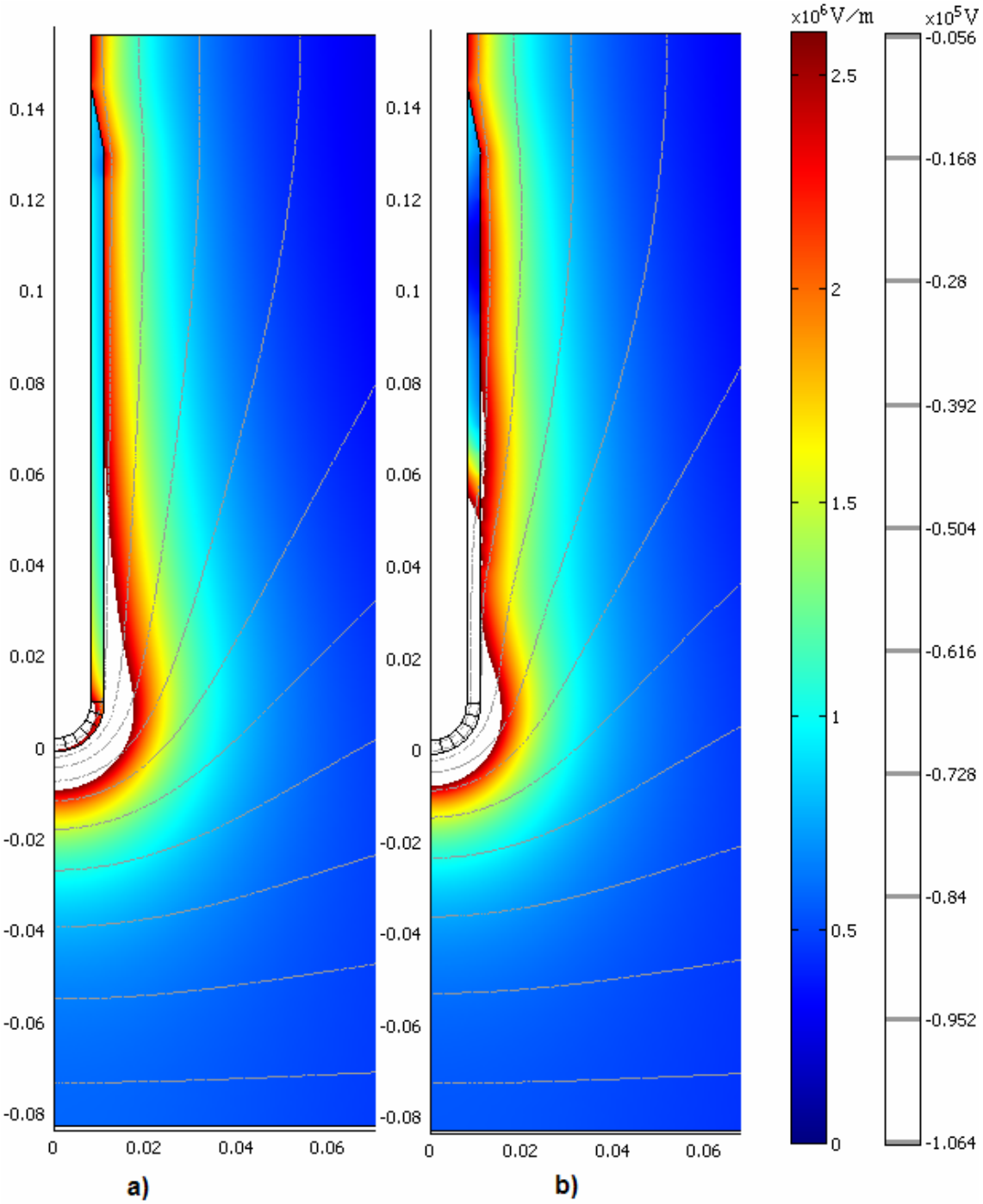

Fig. 5.47 – Capacitive field distribution for case IV without surface charges. Rotational symmetry around x=0. The white area indicates where the electric field is high enough to initiate discharge activity in atmospheric air. Corresponding discharge image in Fig. 5.33 (page 76). Electrode distance 85mm and applied voltage -112 kV.
b) Field distribution for case IV with surface charge distribution found by TSVD.

6 DISCUSSION

The main goal of this work has been to increase the knowledge of hybrid insulation in inhomogeneous electric fields studying discharge phenomena, surface charge distribution and the stress of the solid insulation. The concept of hybrid insulation has been tested by means of a hemispheric rod covered with a 3 mm layer solid insulation (RTV SIR). The influence of field inhomogeneity, surface charge accumulation and material properties of the solid insulation on the performance of the insulation system has been studied.

Surface charge measurement set-up
The measurements of the surface charge distribution should ideally be made as close as possible to the insulation surface. However, it is complicated to make a measurement set-up that traces the hemispheric part of the rod. As a compromise, a cylinder was used that was placed around the test object with the field mill placed in the cylinder wall. Hereby the sharp edges of the field mill are hidden preventing the field mill to cause discharges that can damage the field mill and measurements. In the late phase of this work, attempts were made to take additional measurements along a horizontal plate right under the hemispheric rod to get a better overview of the surface charge distribution on the hemispheric part of the rod. However, these measurements failed as the probe accidentally was damaged during the measurements.

Inception/breakdown voltage
Earlier presented results have shown that covering one of more electrodes in a gas gap can increase the breakdown voltage of the system significantly. The increase in breakdown strength is dependent on the electrode configuration and voltage shape.
To find the inception voltage, the standard up-and-down method (IEC 60060-1) has been used to find the correlation between electrode distance and discharge inception voltage.

A discharge directly leads to breakdown of the insulation system when a positive lightning impulse is applied to a rod plane gap with uncovered electrodes.

For covered electrodes, the discharge inception voltage is lower than the breakdown voltage and independent of how much of the rod that is covered with solid insulation.

As seen in Fig. 4.1, the inception/breakdown voltage for positive impulses improves as the electrode is covered with a layer of solid insulation. The rate of increase depends on the electrode distance and polarity. Negative discharges are observed at a lower voltage than positive ones at same electrode distance. However, the breakdown voltage for

covered electrodes is higher for negative impulses than for positive ones, also when the covered length is limited as used here (about 150 mm). Breakdown for both negative and positive discharges takes place along the surface of the solid insulation, leaving the solid insulation unharmed and retaining the insulating level it had before breakdown of the insulating system.

The increase in inception voltage for positive lightning impulses varied from 35% to around 100%. The increase in inception voltage was found to be dependent on electrode distance. The higher the inhomogeneity is, the smaller the increase in inception voltage.

Discharge pattern
The observed patterns for positive and negative air discharges are different. The behaviour is fairly similar to the discharge patterns observed in uncovered rod-plane gaps in air. For positive discharges, the streamers bridge the air gap and spread upwards along the rod. Negative discharges are more diffuse and forms streamers around the tip of the rod only. Further upwards along the rod the discharge activity is weak. Negative streamers are somewhat thicker and do not form branches like the positive streamers do. This may be explained by the electrons fanning out following the field lines and new avalanches cannot readily be formed preventing the discharge activity to grow further out in the air gap. However, around the tip, the electric field is sufficiently high to cause the streamers to grow further towards the plane. When the background field is sufficiently high, these streamers bridge the air gap. When initiated, positive streamers need a lower background field to grow compared to negative streamers. This can also explain the larger current measured for positive impulse voltage application at the plane compared to negative impulse voltage.

Accumulation of surface charges
During the lightning impulse application, discharge activity is most likely to start in the air gap around the tip where the electric field is highest and continue spreading upwards along the covered rod.

As expected, negative charges accumulate on the surface in the case of positive impulse voltage and vice versa. However, as seen in Fig. 4.25, after stronger discharges during negative impulse voltage application, surface charges of both polarities are observed and not only positive as would be expected.

A proposed mechanism for this is: that during the negative lightning impulse application, discharge activity is most likely to start in the air gap around the tip where the electric field is highest and spread upwards along the rod. Positive charges attract in the direction of the solid insulation surface while the negative charges follow the electric field lines towards the earthed plane. On the solid insulation surface, positive charges accumulate, creating a field component along the surface upwards. This, together with ionization due to photon emission from the discharges close by, helps to spread the discharge activity upwards along the rod. Between the tip of the rod and the plane, negative charges and electrons in the head of the avalanches reach the earthed plane. Electrons and negative ions created further up do not reach the plane before the applied impulse has died out and forms negative space charges. Positive surface charges

attract some of these and recombine. Due to drift and diffusion, negative charges accumulate on the surface, resulting in surface areas with negative surface charges. A similar process is also believed to take place during and after a positive discharge reducing the magnitude of the accumulated surface charge. This is also shown graphically in Fig. 6.1.

The same phenomenon is expected to take place after application of a positive lightning impulse although no change of polarity in the surface charge distribution has been observed. Positive discharges are associated with a higher discharge activity and surface charge density compared to negative discharges. In addition to the much lower mobility of positive ions compared to electrons, this can explain why only positive surface charges are observed.

Discharge propagation

Discharge activity is normally expected to take place where the electric field is above the critical field strength (for atmospheric air at 20ºC around 2.6 kV/mm). When applying an impulse voltage to a covered rod in a rod-plane gap, the discharge activity was also observed in unexpected areas. For negative discharges, visible discharge activity is observed upwards along the rod where the background field is around 2.5 kV/mm and higher. For positive discharges, visible discharge activity is observed along the insulating surface where the background field is around 2.3 kV/mm and higher. This is probably caused by the field enhancing effect of surface and space charges and ionization due to photo-emission from discharges close by enhancing the discharge activity spreading upwards along the rod. Also the duration of the applied impulse voltage affects how far the discharge activity will spread.

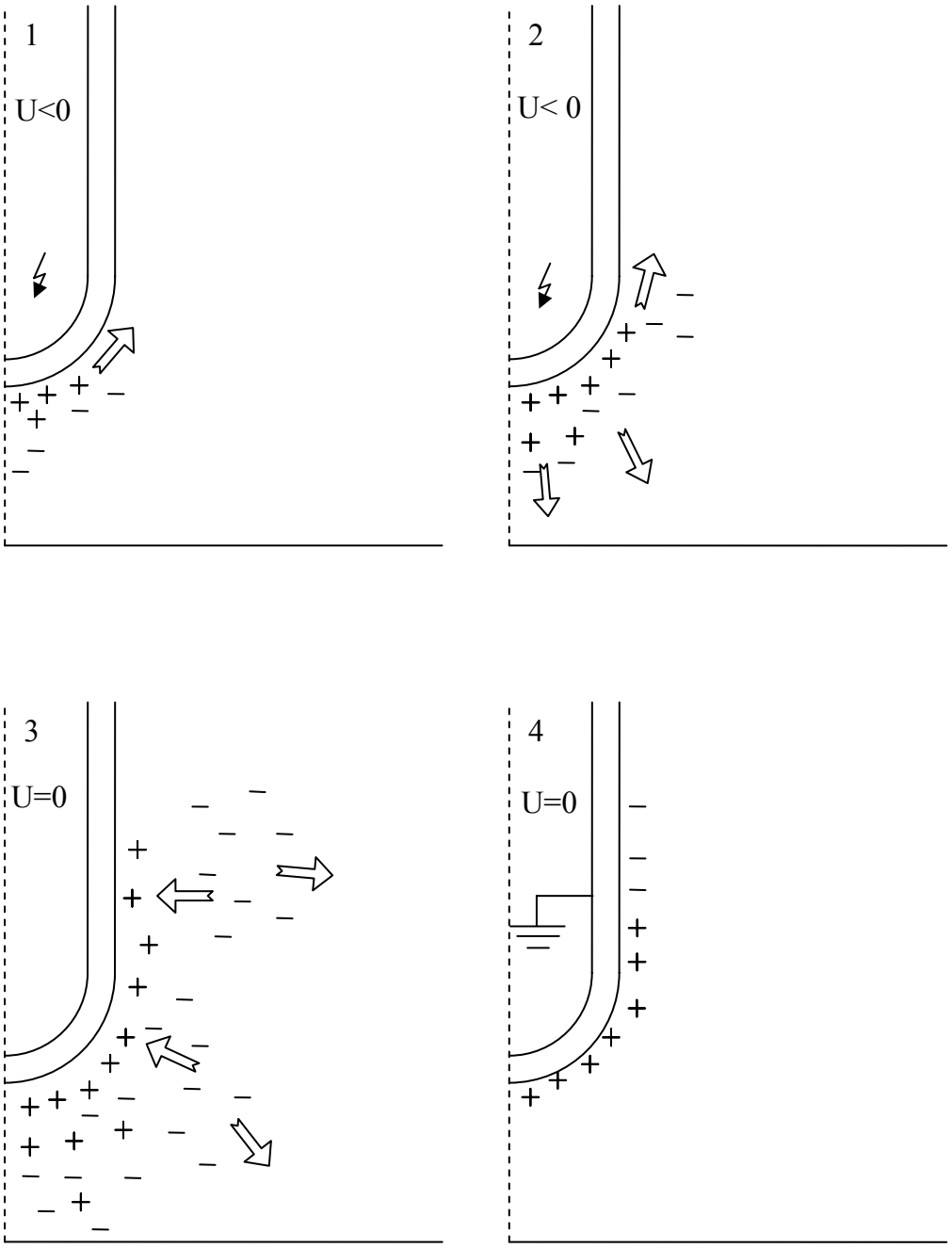

Fig. 6.1 – 1 and 2: Discharge activity starts in the air gap around the tip where the electric field is highest. Positive charges attracts in the direction of the solid insulations surface while the negative charges follow the electric field lines towards the earthed plane. The positive surface charges create a field component directed upwards parallel to the surface, driving the discharge activity upwards along the rod together with ionization due to photon emission from the discharges close by.
3 and 4: Right after the voltage impulse has died out, positive and negative ions and electrons are available in the air gap. The positive surface charge attracts some of these and recombines. Due to drift and diffusion, negative charges accumulate on the surface, resulting in surface areas with negative surface charges.

Charge Decay
The accumulated surface charges decay exponentially with a time constant τ that can vary from micro-seconds to hours. The most important relaxation mechanism is conduction through the solid insulation making the time constant mainly dependent on the permittivity ε and conductivity σ_a of the solid material.

The charge decay also depends on the charge density magnitude of the surrounding areas. Areas with a relatively high charge density compared to surrounding areas tend to smooth out after some time indicating a longitudinally current due to the local high electric field strength.

After voltage application, the remaining surface charges are generally unwanted, unless a surge impulse of the same polarity is expected. If surface charges still are present when a lightning impulse of opposite polarity follows, it might result in a breakdown of the insulation system as the electric field in the air gap is enhanced by the remaining surface charges.

When using covered electrodes in practical insulation systems, the remaining surface charges can represent a problem during type testing and routine testing (factory acceptance test) when changing polarity. The standard IEC 694 [51-53], §6.1.6, note 1 says "*Some insulating materials retain a charge after an impulse test and for these cases care should be taken when reversing the polarity. To allow the discharge of insulating materials, the use of appropriate methods, such as the application of impulses of the reverse polarity at lower voltages before the tests, is recommended*".
This eliminates the remaining surface charge problem after polarity reversal.

Remaining surface charges can also create a problem during repetitive testing with the same polarity as the breakdown voltage might become unrealistically high during impulse voltage testing. To ensure a more realistic test, surface charges should be removed between each impulse application where surface charges have been formed.

In practice, a 50 (or 60) Hz system voltage is also applied to the insulation system. This reduces the magnitude of the accumulated surface charges after a lightning impulse if the total electric field in the air gap is high enough to cause new discharges.

Material properties of the solid insulation
Through iodine doping the conductivity of the solid insulation was strongly increased. A very small time constant was achieved (42 ms) and experiments show little difference in discharge pattern. The main difference is the somewhat lower inception voltage compared to the undoped SIR, but still higher than for an uncovered electrode.

The experiments show that even with high conductivity, the principle of hybrid insulation works. High conductivity ensures the fast removal of the remaining surface charges and thus eliminating the problem with remaining surface charges after a lightning impulse. However, high conductivity can cause high resistive losses during ac voltage application that can cause damage to the solid insulation. The high temperature dependency of the conductivity of the solid insulation should also be taken into consideration.

Surface charge density estimation

The most common method to find the surface charge distribution for thin objects is direct measurement, while for thick objects and objects with a high surface charge density, measurements are made at a greater distance to avoid discharges or flashover to the measurement probe. This complicates the calculation of the surface charge density significantly since both the surrounding surface charges and the surface charges directly underneath the probe make a contribution to the probe response. The λ-method by A. Pedersen takes this into consideration [1]. The inverse problem that the calculation of the surface charge distribution represents is very sensitive to perturbations in the measurements, as the resulting matrix is singular. The λ-method has therefore previously not been applied to practical measurements.

This work has shown that by applying regularization to the problem, the influence of perturbations can be reduced significantly and a more stable solution can be found. In this thesis, three different methods with regularization have been applied to the problem:

- BEM with regularization
- FEM with regularization
- Pedersen's λ-method using TSVD as regularization.

By applying regularization to the problem, the influence of perturbations is reduced, but at the same time some information is lost. Results indicate that a stable solution of the problem is achieved giving a good estimation of the surface charge density.

The methods involving BEM and FEM seem promising, but when using the calculated surface charge to recalculate the probe response, large deviations between the calculated and measured was observed. The deviation of the surface charge density around the tip of the rod was also very high.

For the FEM method, the deviation was mainly caused by the poor coupling between the tip and measurement area. This has been confirmed by simulations using Comsol Multiphysics [40] where relatively large changes in the surface charge densities on the tip of the rod lead to a small change in the probe response. Ideally the measurement should take place as close to the surface charges as possible, but with the geometry used it was impossible to move the probe underneath the tip of the rod.

The method giving the best surface charge estimation tested here is the λ-method using TSVD as regularization and moving average. Simulations show that both with 1% and 10% white noise added to the probe response, the maximum deviation between calculated and applied surface charge is about 10%. When the surface charge density changes rapidly, the deviation is somewhat larger but still follows the applied surface charge distribution well.

For the electrode configurations used here the λ-method with TSVD has proven to be best suited.

Surface charge density – practical measurements

Video images and E-field probe measurements show a good correlation for both positive and negative voltage impulses. Discharges during positive voltage impulses emit more light than the negative and also cover a greater part of the air gap. For positive discharges the probe response is higher than for the negative voltage impulses. The surface charges accumulated have a maximum value around 0.6-1.5 μC/m² and 0.4-1 μC/m² after positive and negative impulses, respectively. Comparing the discharge images and the calculated surface charge density, it can also be seen that the surface charge density in the areas with highest discharge activity is relatively uniform. Further upwards along the rod, the charge density is reduced towards zero after a short length, and in some cases changes polarity before it is reduced towards zero again.

Using the calculated surface charges to calculate the field distribution before and after discharges shows that the electric field in the most cases is high enough to cause new discharges with the accumulated surface charges present. No discharge activity was detected after the discharge around the peak value of the lightning impulse voltage. This indicates that as soon as the discharge activity has died out, recombination takes place such that the magnitude of the accumulated surface charge is reduced.

7 CONCLUSIONS

This work has focused on hybrid insulation in case of inhomogeneous electric fields and lightning impulse voltages. The principal idea behind hybrid insulation is to transfer a significant part of the electric stress from the dielectrically weaker gas over to the dielectrically stronger solid insulation through surface charge accumulation. The increase in dielectric strength compared to uncovered rods, the distribution of discharge activity and accumulation of surface charge have been studied in this work.

New methods for measurement of surface charges have been developed and evaluated.

Experimentally the increase in positive inception voltage, compared to uncovered rods, is considerable. The increase varied from 35% up to 100% dependent on the electrode distance. The breakdown value is generally higher and dependent on how much of the rod that is covered.

During application of a lightning impulse, the discharge activity spreads upwards along the rod and out in the air gap. Video images taken during impulse voltage application show that positive discharges form numerous branches and, in most cases, bridge the air gap. Negative discharges are more diffuse, less light intensive and only form a few branches around the tip of the rod where the electric field is highest. For negative discharges the discharge inception voltage is lower than for the positive one, but as for uncovered electrodes in air, breakdown takes place at a higher voltage than for positive lightning impulse voltages.

For both polarities, discharge activity is observed where the field strength is lower than the critical electric field strength. Electric field simulations and video images of discharge activity show that the discharge activity spreads upwards along the rod providing the background field is higher than 2.3 kV/mm and 2.5 kV/mm for the positive and negative impulses respectively.

During application of lightning impulses, discharge activity starts in the air gap around the tip where the electric field is highest and spreads upwards along the rod. As expected, negative charges accumulate on the surface in case of positive impulse voltage and vice versa. However, after more powerful discharges during negative impulse voltage application, surface charges of both polarities are observed. This is due to positive surface charges attracting negative space charges and drift and diffusion.

Accumulated surface charges decay exponentially with a time constant τ varying from micro-seconds to hours depending on the material properties of the solid insulation. The

most important relaxation mechanism is found to be conduction through the solid insulation. The charge decay is also dependent on the charge density magnitude of the surrounding areas. Areas with a relatively high charge density compared to surrounding areas tend to smooth out after some time due to conduction.

Improved methods to calculate surface charges based on probe response for a 2D axial symmetric case have been developed and evaluated. The method best suited for this purpose is the λ-method with TSVD as regularization. Theoretical calculations shows that the deviation between applied and calculated surface charge is small based on a probe response with up to 10% white noise.

Comparison between video images, probe responses and calculated surface charge density shows a good correlation. Surface charge calculations show that the accumulated surface charges for the used configuration typically have a maximum value of 0.6 to 1.5 μC/m² and 0.4 to 1 μC/m² after the positive and negative impulses respectively. The surface charge density in the areas with the highest discharge activity is relatively uniform. Further upwards along the rod, charge density is reduced relatively fast towards zero, and in some cases as discussed, it changes polarity and is then reduced towards zero.

REFERENCES

1. Pedersen, A., G.C. Crichton, and I.W. McAllister, *The Functional Relation between Partial Discharges and Induced Charge.* IEEE Transactions on Dielectrics and Electrical Insulation, 1995.Vol. 2, issue 4.

2. Blennow, J., *Active High Voltage Insulation*. 2000, PhD Thesis, Chalmers University of Technology.

3. Sjöberg, M., *Charge Accumulation in Hybrid High-Voltage Insulation*. 2003, PhD Thesis, Chalmers University of Technology.

4. Falkenstein, Z. and J.J. Coogan, *Microdischarges Behavior in the Silent Discharge of Nitrogen-Oxygen and Water-Air Mixture.* J. Phys. D: Appl. Physics, 1997.Vol. 30, issue: 817-825.

5. Xu, X. and M.J. Kushner, *Multiple microdischarge dynamics in dielectric barrier discharges.* Journal of Applied Physics, 1998.Vol. 84, issue 8: 4153-4160.

6. Xu, X. and M.J. Kushner, *Ion composition of expanding microdischarges in dielectric barrier discharges.* Journal of Applied Physics, 1998.Vol. 84, issue 8: 7522-7532.

7. Raizer, Y.P., *Gas Discharge Physics*. 1997: Springer Verlag.

8. Allen, R.J. and K.H. Schoenback, *Improved electrical insulation of vacuum gaps utilizing SiO_x coatings.* 1997, issue.

9. Matsuo, T. and R.H. Hirotsu, *Coating effect on AC and impulse breakdown stress on SF_6,* in *Int. Symposium on Electrical Insulation Materials*. 1998.

10. Maus, H.A. and J.R. Melcher, *Electromagnetic Fields and Energy* 1989: Prentice-Hall inc.

11. Pedersen, A., *On the Electrical Breakdown of Gaseous Dielectrics.* IEEE Transactions on Electrical Insulation, 1989.Vol. 24, issue 5.

12. Kreuger, F.H., *Industrial High Voltage - part 1, 2 and 3*. 1991: Delft University Press.

13. Llewellyn-Jones, F., *Ionization and Breakdown in Gases*. 1957: Methuen & Co Ltd.

14. Donohoe, J.P., *A comparison of air breakdown criteria for slightly divergent fields*, in *Southeastcon '97*. 1997, IEEE.

15. Meeks, J.M. and J.D. Craggs, *Electrical Breakdown of Gases*. 1978: John Wiley & Sons.

16. Francis, G., *Ionization Phenomena in Gases*. 1960: Butherfords Scientific Publications.

17. Grossmann, K., *Untersuchungen über der Durchschlag in Luft und Flüssigkeiten bei Wechselspannung stark verschiedener Frequenz*. 1931, Braunschweig T.H.: PhDThesis.

18. Bruyn, P.A. and R.G. van Heeswijk. *Influence of a dielectric barrier on the dc and ac breakdown strength of a point-to-point gap in air*.Int. Symp. Electrical Insulation. 1984. Montreal, Canada: IEEE.

19. Ming, L. and M. Leijon. *Factors influencing barrier effects in air-gaps*.Int. Symp. High Voltage Eng. 1995. Graz, Austria.

20. Sjöberg, M., Y.V. Serdyuk, S.M. Gubanski, and M.Å.S. Leijon, *Experimental study and numerical modelling of a dielectric barrier discharge in hybrid air-dielectric insulation.* Journal of Electrostatics, 2003.Vol. 59, issue: 87-113.

21. Serdyuk, Y.V., S.M. Gubanski, J. Blennow, and M. Sjöberg. *Electrical Discharges in an Air-Gap with Dielectric-Covered Electrodes*. CEIDP 2000.

22. Masaki, N., I. Oshima, T. Yoshida, and K. Matsuzawa. *72 kV C-GIS composite insulation in SF_6 gas*.Third International Conference on Future Trends in Distribution Switchgear. 1990.

23. Yoshida, T., et al., *Increase of Breakdown Voltage Due to Composite Insulation in SF_6 Gas.* Electric Engineering in Japan, 1991.Vol. 111, issue 6: 36-45.

24. Baldo, G. and G. Pesavento. *Impulse breakdown of air gaps in series with thick electrode insulation layers*.International Symposium on High Voltage Engineering. 1987.

25. Mizuno, T., et al. *Electrical Insulation Performance in Air gap with Covered Electrodes*.7th International Conference on Properties and Applications of Dielectric Materials. June 2003.

26. Mizuno, T., K. Morita, K. Kurata, and M. Miyagawa. *The Electrical Performance of Air or Nitrogen Gas with Solid Insulation and the Application for Switchgears*. 2002.

27. Darvenzia, M., *Electrical Breakdown of Air between Insulated Conductors*, in *6th Int. Conference on Properties and Applications on Dielectric Materials*. June 2000: Xi'an, China.

28. Walfridsson, L., et al. *Solid Insulating Covering of Conductors Improves Air Insulation Systems*. Int. Conference on Conduction and Breakdown in Solid Dielectrics. June 1998. Västerås, Sweden.

29. Walfridsson, L., et al. *Termination of Creeping Discharges on a Covered Conductor*.8th Int. Symposium on Gaseous Dielectrics. 1998. Virginia, USA.

30. Sudarshan, T.S. and R.A. Dougal, *Mechanisms of Surface Flashover along Solid Dielectrics in Compresses Gases: A Review.* IEEE Transactions on Electrical Insulation, October 1986.Vol. 21, issue 5.

31. Akyuz, M., *Positive Streamer discharges in air and along insulator surfaces: experiment and simulation*. 2002, University of Uppsala.

32. Akyuz, M., A. Larsson, V. Cooray, and G. Sandberg, *3D simulations of streamer branching in air.* Journal of Electrostatics, 2003, issue 59: 115-141.

33. Faircloth, D.C. and N.L. Allen, *High Resolution Measurement of Surface Charge Densities on Insulator Surfaces.* IEEE Transactions on Dielectrics and Electrical Insulation, 2003.Vol. 10, issue 2.

34. McAllister, I.W., *Electric Fields and Electric Insulation.* IEEE Transactions on Dielectrics and Electrical Insulation, October 2002.Vol. 9, issue 5.

35. Tatematsu, A., S. Hamada, and T. Takuma, *A Study of the Accuracy of Surface Charge Measurements.* IEEE Transactions on Dielectrics and Electrical Insulation, June 2002.Vol. 9, issue 3.

36. Takuma, T., M. Yashima, and T. Kawamoto, *Principle of Surface Charging Measurements for Thick Insulating Specimens.* IEEE Transactions on Dielectrics and Electrical Insulation, August 1998.Vol. 5, issue 4.

37. Kumada, A., S. Okabe, and K. Hidaka, *Resolution and Signal Processing Technique of Surface Charge Density Measurement with Electrostatic Probe.* IEEE Transactions on Dielectrics and Electrical Insulation, Feb. 2004.Vol. 11, issue 1: 122-129.

38. Kumada, A., Y. Shimizu, M. Chiba, and K. Hidaka, *Pockels surface potential probe and surface charge measurement.* Journal of Electrostatics, 2003.Vol. 58, issue: 45-58.

39. Kumada, A., R. Yoshida, and K. Hidaka. *Charge Accumulation on a Truncated Cone Spacer under DC Electric Field*.ISH 2005. Beijing, China.

40. Comsol, *Comsol Multiphysics 3.2 - User's guide*. 2006.

41. Hansen, P.C., *The Truncated SVD as a Method for Regularization*, in *BIT 27*. 1987. p. 534-553.

42. Hansen, P.C., *Rank-Deficient and Discreet Ill-Posed Problems*. 1996, Technical University of Denmark: PhD Thesis.

43. Engl, H.W., M. Hanke, and A. Neubauer, *Regularization of Inverse Problems*. 1996: Kluwer Academic Publishers.

44. Brebbia, C.A., *Topics in Boundary Element Research*. 1984: Springer-Verlag.

45. Vasconcelos, J.A., L. Krähenbühl, L. Nicolas, and A. Nicolas, *Design Optimization in Electrostatic Field Analysis Using the BEM and the Augmented Lagrangian Method.* IEEE Transactions on Magnetics, 1994.Vol. 30, issue 5.

46. Dijkstra, W. and R.M.M. Mattheij, *The condition number of the BEM-matrix arising from Laplace's equeation.* Electric Journal of Boundary Elements, 2006.Vol. 4, issue 2: 67-81.

47. Zhong, W.-X., *Engineering Electromagnetism: Functional Methods*. 1991: Ellis Horwood.

48. Suttmeier, F.T., *work note - FEM simulations*. February 2006.

49. Suttmeier, F.T. and T.K. Varslot, *FE-approximations of problems with Cauchy-type boundary data*. October 2005.

50. Matlab. *http://www.mathworks.com/*.

51. *IEC 649, Common clauses for high-voltage switchgear and controlgear standards*. 1980.

52. *IEC 649, Amandent 1 - Common clauses for high-voltage switchgear and controlgear standards*. 1985.

53. *IEC 649, Amandent 2 - Common clauses for high-voltage switchgear and controlgear standards*. 1993.

APPENDIX A - Singular Value Decomposition

Let $A \in \mathbb{R}^{m \times n}$ be a rectangular or square matrix with m ≥ n. The singular value decomposition (SVD) of the matrix A is then a decomposition of the form[1]:

$$A \equiv U \Sigma V^T = \sum_{i=1}^{n} u_i \sigma_i v_i^T \tag{5.24}$$

where U = ($\mathbf{u}_1$, $\mathbf{u}_2$, … , $\mathbf{u}_n$) and V = ($\mathbf{v}_1$, $\mathbf{v}_2$, … , $\mathbf{v}_n$) are orthogonal matrices and $U^TU = V^TV = I_n$. The diagonal elements of the matrix Σ = diag(σ_1, σ_2, … , σ_n) are positive where $\sigma_1 \geq \sigma_2 \geq \ldots \geq \sigma_n \geq 0$. The numbers σ_n are called the singular values of A. The first n columns of U are called the right singular vectors and the first m rows of V left singular vectors for the corresponding singular values.

From the relations

$$A^TA = V\Sigma^2V^T \tag{5.25}$$

and

$$AA^T = U\Sigma^2U^T \tag{5.26}$$

it can be showed that the SVD of A is strongly linked to the eigenvalue decompositions of symmetric matrices A^TA and AA^T. This shows that the SVD of a given matrix A is unique, up-to a sign change in the pair ($\mathbf{u}_i$, $\mathbf{v}_i$) [42]. For ill-posed problems, the following two characteristic features for the SVD are typical:

- The decay of the singular values σ_i gradually goes towards zero with no particular gap in the spectrum. An increase in the dimensions of A increases the number of small singular values.
- The left and right singular vectors tend to have more sign changes as the number of singular values increases.

For more detailed theory on SVD, refer to [41-43].

[1] If m < n, A is replaced by A^T, U and V interchanged

NTNU
Norwegian University of Science and Technology

PhD Thesis

Faculty of Information Technology, Mathematics and Electrical Engineering
Department of Electric Power Engineering

ISBN 82-471-8261-0 (printed version)
ISBN 82-471-8260-2 (electronic version)
ISSN 1503-8181

Doctoral theses at NTNU, 2006:239

Printed by NTNU-trykk